ISBN 978-82-326-3246-6 (printed version)
ISBN 978-82-326-3247-3 (electronic version)
ISSN 1503-8181

Doctoral theses at NTNU, 2018:228

Karlis Rieksts

Heat Transfer Characteristics of Crushed Rock and Lightweight Aggregate Materials

Doctoral Thesis

Karlis Rieksts

NTNU
Norwegian University of
Science and Technology

Doctoral theses at NTNU, 2018:228

NTNU
Norwegian University of
Science and Technology
Faculty of Engineering
Department of Civil and Environmental Engineering

NTNU
Norwegian University of
Science and Technology

NTNU

Karlis Rieksts

Heat Transfer Characteristics of Crushed Rock and Lightweight Aggregate Materials

Thesis for the degree of Philosophiae Doctor

Trondheim, October 2018

Norwegian University of Science and Technology
Faculty of Engineering
Department of Civil and Environmental Engineering

NTNU
Norwegian University of
Science and Technology

NTNU
Norwegian University of Science and Technology

Thesis for the degree of Philosophiae Doctor

Faculty of Engineering
Department of Civil and Environmental Engineering

ISBN 978-82-326-3246-6 (printed version)
ISBN 978-82-326-3247-3 (electronic version)
ISSN 1503-8181

Doctoral theses at NTNU, 2018:228

Printed by Skipnes Kommunikasjon as

Preface

This doctoral study has been submitted to the Norwegian University of Science and Technology (NTNU) in August, 2018 as partial fulfillment of the requirements for the degree of Doctor of Philosophy. The work has been mostly carried out at NTNU at the Department of Civil and Environmental Engineering. Part of the time developing the numerical models was spent at Laval University in Canada.

The doctoral study was started in 2015 and is a part of a larger research project called "Frost Protection of Roads and Railways" (2015–2019) which is supported by the Research Council of Norway under research grant 246826/O70. However, the project has also involved a wide collaboration with academic, public and private institutions: Laval University, the Norwegian Public Roads Administration (Statens vegvesen), the Norwegian National Rail Administration (Bane NOR), and SINTEF Byggforsk, Glasopor and Leca. The project has two main research areas: heat transfer mechanisms in granular materials, and frost susceptibility for pavement materials. The former is the field of study for the current doctoral thesis and associated papers.

The main supervisor for this work was Professor Inge Hoff of the Department of Civil and Environmental Engineering at Norwegian University of Science and Technology. The work was co-supervised by PhD Elena Scibilia, of the same department, and Professor Jean Côté from the Department of Civil and Water Engineering at Laval University, Canada.

During the course of this study, seven research papers have been produced. One paper was submitted and presented at a conference, while the other six have been submitted to different scientific journals. These seven papers together present a detailed piece of research based on laboratory experiments, numerical modeling and field observations. Of the seven, two are dedicated to thermal conductivity in crushed rock materials; four papers cover research on air convection in coarse granular materials (crushed rock and insulation materials), and one presents a field study and the development of the numerical model to further analyze the thermal response of construction materials.

The committee for the appraisal of this thesis comprises the following members:

Professor Pauli Kolisoja (first opponent),
Tampere University of Technology, Finland

Chief Engineer Geir Berntsen (second opponent),
Norwegian Public Roads Administration, Norway

Associate Professor Helge Mork (administrator),
Norwegian University of Science and Technology, Norway

The supervisors of this study were:

Professor Inge Hoff, main supervisor
Norwegian University of Science and Technology, Norway

Researcher PhD Elena Scibilia
Norwegian University of Science and Technology, Norway

Professor Jean Côté
Laval University, Canada

Acknowledgements

I would first like to thank my supervisor, Professor Inge Hoff, for giving me the opportunity to join the project and to work and live in Norway. I thank him for all the freedom and independence that he has allowed me, and will always remember his words at our first meeting: “Consider us as advisors, not supervisors.” I would also like to thank my co-supervisor Elena Scibilia. She has done truly amazing work managing the project, involving new people and coming up with great ideas. Most of all I thank her for her support, enthusiasm and positivity, and for cheering me up when it was most needed. And finally I would like to thank my co-supervisor Jean Côté for his support and knowledge throughout the study. From a scientific perspective, I have to give him the most credit for his preceding work on this field, which has largely served as the basis of my project. I thank him for all his ideas and comments, and for his thorough review of the drafts which brought them from good to better.

Next I would like to extend my thanks to all the partners involved in our project for sharing their knowledge and experience and giving positive feedback on the progress of the study. These thanks go particularly to Jostein Aksnes and Kjell Arne Skoglund (Norwegian Public Roads Administration, Statens vegvesen); Juan Barrera (Norwegian National Rail Administration, Bane NOR); Rune Skarstad, Thomas Bjørhusdal and Tore Bye (Glasopor); Oddvar Hyrve and Jon Hauge (Leca); and Yared Bekele (SINTEF). All of these people also took part in the advisory board meetings and engaged in discussions on project progress. I would also like to thank other individuals contribution to the advisory board: Arnstein Watn, Svein Willy Danielsen and Ole Arild Haugum.

Special thanks to Bent Levrik and Jan Erik Molde for all their assistance with the experimental setups in the laboratory and during the construction of the field test site in Røros. I would also like to thank other people for their assistance and help in experimental procedures and field work: Zahra Rahimi, Lisbeth Johansen, Olivier Sylvester, and Andrea Balestri. And thanks to Espen Eberg and Hans Helmer Sæternes from SINTEF Energy for lending their needle probe and engaging in discussion on the thermal conductivity of soils. I thank Mohammad Rahimi for all his help with developing the numerical models; Roar Nålsund for his knowledge about and advice on designing railway sections at our test site; Eyolf Erichsen for sharing his knowledge of the thermal conductivity of rocks and their mineralogical composition; and Øistein Johansen for his work on the field of thermal conductivity of soils and large-scale experiments on natural air convection. It was a great pleasure to meet him, and his contribution to this field of science is so big that I cite his doctoral thesis in every single paper.

It has been a great work environment during these last three years, and that is only because of my wonderful colleagues and the excellent administration team who has always taken care of us and created social activities so that we feel more like a family than just colleagues. Of my colleagues I would specially like to thank my fellow PhD candidate Benoit Loranger for the conversations and discussion we have had to progress our project. Best wishes to him in finalizing his work and bringing the whole project to a major

conclusion. And special thanks also to my dear colleague Albert Lau for taking care of my cat when conferences called.

Deep gratitude goes to my loving parents back home for all their support throughout these years of education and work. I thank them so much for understanding my decision to expand my horizons and study abroad.

And finally, my deepest gratitude goes to my beloved wife and much more than that, Jolanta, for all her support and encouragement throughout these years. I thank her for all those countless discussion on how biology is different from engineering, and why statistics are not crucial as long as your models are physically based. I thank her for cheering me up when I was feeling down and overwhelmed by all the work. I thank her for knowing my work probably better than anyone else. Only she knows all the behind-the-scenes struggles I went through to finally come up with this written version of my work. Most of all I thank her for being in my life, as I would probably not have started this three-year journey without her in the first place.

Abstract

Over the last decades there has been a major transition to using crushed rock materials for road and railway construction instead of natural materials such as sand or gravel. In addition, it is common practice to use very coarse and sometimes open graded materials for structural layers. For instance, a typical material for a subbase layer is 20/120 mm crushed rock, while even coarser materials of up to 500 mm can be used for the frost protection layer. Knowledge of the thermal properties of construction materials is crucial for proper thermal design for road and railway structures. Thermal conductivity is the governing heat transfer mechanism in most such materials. However, with coarse open graded materials, natural air convection can make a significant contribution to the overall heat transfer. This can result in unanticipated frost penetration depth and differential heaving, due to the effect of natural convection.

This study investigates the heat-transfer characteristics of granular materials with a focus on natural air convection. It consists of three parts: i) small-scale experiments on particle thermal conductivity and crushed rock thermal conductivity, and the validation and adaptation of an existing thermal conductivity model; ii) large-scale experiments on natural convection and the establishment of intrinsic permeability; iii) investigations of possible air convection under field conditions in a full-scale road structure.

The thermal conductivity of rock material (k_s) is a crucial input parameter for the estimation of the thermal conductivity of crushed rock materials. Hence a minor number of the small-scale experiments were dedicated to the investigation of different methods for measuring or approximating k_s. The study showed that measurements of the thermal conductivity of rock core samples can be underestimated, most likely due to contact resistance. The geometrical mean method, based on the percentage and thermal conductivity of each rock-forming mineral, gives fairly good results. However, the method relies on precise measurement of mineralogical composition. In this study, the most successful method for estimating k_s was assumed to be from measurements of saturated samples and subsequent back-calculation of k_s values. These values were then used as input parameters for the thermal conductivity model.

For the validation and adaptation of the thermal conductivity model, 42 samples were prepared and 328 tests conducted in unfrozen and frozen states with different degrees of moisture content. An existing thermal conductivity model was used and the model's prediction was compared to the experimental values. The results showed that the model slightly overestimates thermal conductivity values, especially at the low end of the range of moisture levels. Given that the model was developed based on a particular set of data, using it for different materials requires model calibration. The thermal conductivity model incorporates two parameter accounting for structure effects. The calibrated model showed increased prediction accuracy compared to the experimental results.

A large-scale heat transfer cell with an inner volume of 1 m^3 was used to measure the increase in heat transfer due to natural air convection. A method based on the analytical Nusselt (Nu)-Rayleigh (Ra) number relationship was used to establish the intrinsic permeability (K) of different construction materials. These included three crushed rock

materials (20/120, 40/120 and 20/250 mm) and two lightweight aggregates: expanded clay and foam glass. The experimental results showed that natural air convection could be initiated in all three crushed rock materials at a fairly low temperature gradient (∇T) of 4.5 to 6.5° C/m. The established K for crushed rock materials ranged from 1.1 to $2.2x10^{-6}$ m^2. Air convection for foam glass and expanded clay (10/20 mm) material was initiated at critical ∇T of 11.0 and 22.5°C/m respectively. The corresponding K values based on the experimental measurements were 0.86 and $0.17x10^{-6}$ m^2. The overall results show that air convection can be induced at a relatively low ∇T.

The method for establishing intrinsic permeability is based on an idealized case with adiabatic conditions when uniform temperature conditions are applied to the sample. The laboratory experiments, however, deviated in several ways from the idealized case: the side insulation was not perfect, and the interface sand layers added at the top and the bottom of the sample would affect the resulting Nu-Ra relationship. To account for this and to get a test-setup-specific Nu-Ra relationship, a numerical model was developed. The model results show that the added sand layers had the largest impact on the resulting Nu-Ra relationship. However, it was also found that the Nu-Ra relationship was dependent on the effective thermal conductivity (k_e) of the test sample. Finally, the Nu-Ra relationship was expressed as a function of k_e. With the adjusted Nu-Ra relationship, the K values were re-established and were found to be 8–26% lower than those established using the analytical Nu-Ra relationship.

To observe material characteristics under field conditions, a full scale test site was constructed incorporating ten different sections. This study, however, focuses on only two sections, which had layers of open graded materials. Observations of the temperature profiles during the cooling period found that ∇T exceeded the critical value in all open graded layers. However, given that the air convection also depends on layer thickness, apparent Rayleigh number (Ra*) was calculated. The results show that Ra* exceeded the critical value only in a 1.0 m thick frost protection layer (40/120 mm crushed rock) and a 0.6 m thick foam glass layer (10/60 mm). To further investigate possible air convection under field conditions, a numerical model was developed. The results from the model clearly show the presence and effect of air convection. However, it could be that the effect of convection was overestimated, given that the K values were established under laboratory conditions with materials with no compaction.

To sum up, this study has shown that a simple thermal conductivity model could be adapted, with slight calibration, for the estimation of thermal conductivity in crushed rock materials. The study has also shown that natural air convection could easily be initiated in coarse materials used in road construction under relatively low temperature gradients. The study at the field test site found that layers with coarse, open graded materials are exposed to very high temperature gradients. The field observations and analysis together with the numerical model showed the possible presence of natural air convection. Air convection can have an adverse effect on seasonal freezing environments by increasing the depth of frost penetration, resulting in possible differential heaving.

List of publications

Publications included in the thesis:

This thesis consists of an overview of the publications referred to in the text by their Roman numbers:

I Rieksts, K., Hoff, I., Scibilia, E. and Côté, J., 2018. Establishment of intrinsic permeability of coarse open graded materials – a review and analysis of existing data from natural air convection tests. Submitted to *Cold Regions Science and Technology*.

II Rieksts, K., Hoff, I., Kuznetsova, E. and Côté, J., 2017. Laboratory investigations on heat transfer of coarse crushed rock materials. *GeoOttawa 2017, the 70th Canadian Geotechnical Conference and the 12th Joint CGS/IAH-CNC Groundwater Conference in Ottawa, Canada (October 1-4, 2017)*.

III Rieksts, K., Hoff, I., Scibilia, E. and Côté, J., 2018. Laboratory investigations on convective heat transfer for road construction materials. Submitted to *Canadian Geotechnical Journal*.

IV Rieksts, K., Hoff, I., Scibilia, E. and Côté, J., 2018.Modelling the Nu-Ra relationship to establish the intrinsic permeability of coarse open graded materials from natural air convection tests in $1m^3$ cell. Submitted to *International Journal of Heat and Mass Transfer*.

V Rieksts, K., Hoff, I., Scibilia, E. and Côté, J., 2018. Comparison of different methods to assess the thermal conductivity of crushed rock solid particles used for road and railway construction. Submitted to *International Communications in Heat and Mass Transfer*.

VI Rieksts, K., Hoff, I., Scibilia, E. and Côté, J., 2018. Thermal conductivity of crushed rock material over a wide range of mineralogy and degree of saturation. To be submitted to *Cold Regions Science and Technology.*

VII Rieksts, K., Hoff, I., Scibilia, E. and Côté, J., 2018. The effect of natural convection on frost penetration: comparison between field observation and numerical model. Submitted to *Cold Regions Science and Technology.*

Declaration of authorship

Publication I

K. Rieksts wrote the article and conducted the analysis. I. Hoff, E. Scibilia and J. Côté contributed to the paper by editing the manuscript, engaging in productive discussions and giving valuable feedback, comments and suggestions.

Publication II
K. Rieksts performed the laboratory measurements, wrote the article and conducted the analysis. I. Hoff, E. Scibilia and J. Côté contributed to the paper by editing the manuscript, engaging in productive discussions and giving valuable feedback, comments and suggestions.

Publication III
K. Rieksts performed the laboratory experiments, analyzed the data and wrote the article. I. Hoff, E. Scibilia and J. Côté contributed to the paper by editing the manuscript, engaging in productive discussions and giving valuable feedback, comments and suggestions.

Publication IV
K. Rieksts developed the numerical model, performed simulations, analyzed the data and wrote the article. I. Hoff, E. Scibilia and J. Côté contributed to the paper by editing the manuscript, engaging in productive discussions and giving valuable comments and suggestions.

Publication IV
K. Rieksts conducted the laboratory experiments, analyzed the data and wrote the article. I. Hoff, E. Scibilia and J. Côté contributed to the paper by editing the manuscript, engaging in productive discussions and giving valuable feedback, comments and suggestions.

Publication VI
K. Rieksts conducted the laboratory experiments, performed data analysis and wrote the article. I. Hoff, E. Scibilia and J. Côté contributed to the paper by editing the manuscript, engaging in productive discussions and giving valuable feedback, comments and suggestions.

Publication VII
K. Rieksts took part in the construction of the field test site, developed the numerical model, performed the data analysis and wrote the paper. I. Hoff, E. Scibilia and J. Côté contributed to the paper by editing the manuscript, engaging in productive discussions and giving valuable feedback, comments and suggestions. In addition, I. Hoff and E. Scibilia took part in the construction process of the field test site.

Contents

1 Introduction

This introductory chapter briefly describes the study of the heat transfer characteristics of crushed rock and lightweight aggregate materials. The chapter is split into four sections describing the background to the study (section 1.1), the research objectives and scope (1.2), the research approach (1.3) and the structure of the thesis (1.4).

1.1 Background

The winters of 2009/2010 and 2010/2011 in south-eastern part of Norway were excessively cold, resulting in frost-related damage to even newly-built roads and railways (Seehusen, 2011; Tunmo, 2010). The damage caused to road and railway structures was mostly related to frost heave problems originating from excessive and unanticipated frost penetration depth. This attracted public attention, with some articles in newspapers creating negative publicity for the national road and railway authorities. The Norwegian Public Road Administration therefore established an expert group to find the causes of excessive frost heave and propose changes to the existing regulations. Since then, Handbook N200 (2014) has been revised twice, in 2014 and a new version to be released in 2018.

Handbook N200 (2014) introduced new requirements for materials used in frost protection layer (FPL) for road structures. First, the use of untreated blasted material originating from tunnel construction was prohibited. The main reason for this is the high inhomogeneity of this material and insufficient quality control. Second, the new regulations declare that only crushed rock should be used for FPL. However, they set only a few requirements for material particle gradation: i) the maximum particle size is limited to 500 m, or half of the layer thickness; ii) at least 30% of the material must be below 90 mm; and iii) the fraction of fines (<0.063 μm) should be 2–15% of material below 22.4 mm. With these three limiting factors, the new regulations allow for rather large interpretation of particle gradation. Given the requirements, one could use an open graded material with a minimal amount of fines, or use a fine material (only below 22.4 mm) with the maximum allowed fines content. Either case would most likely have an adverse effect on frost protection performance.

Over the last decades there has been a major transition from using natural mineral materials to using crushed rock materials in road and railway construction. The main reason for this is the depletion and unavailability of natural resources such as sand and gravel. In addition, crushed rock materials offer better performance in terms of mechanical properties. Natural mineral resources, unlike crushed material, are available only in the size found in nature. Typically, gravel is found with a particle size of 6–20 mm, and coarse gravel can have a particle distribution of 20–60 mm (Johansen et al., 1976). The gradation and particle size of crushed material can be largely controlled by blasting, multistage crushing and screening processes (Rothery & Mellor, 2006). Coarse materials are typically used for unbound layers in road and railway structures (Fladvad et al., 2017). While many of the current road construction regulations are based on the properties of natural soils, gravel and

crushed rock are significantly different, and previous knowledge of natural materials cannot be directly applied to crushed rock materials (Côté & Konrad, 2009).

Seeing that current regulations should be based on more experimentally-backed validation of the materials currently used in road and railway construction, a project called Frost Protection of Roads and Railways (the Frost Project) was initiated at Norwegian University of Science and Technology (NTNU). The Frost Project investigates frost heave issues and the thermal properties of road and railway construction materials. The latter is covered in this thesis and is the topic of associated papers. Particular attention has been paid to the use of coarse materials that could result in unanticipated natural air convection, which would ultimately reduce the effectiveness of frost protection. Natural air convection has been the subject of research in various branches of engineering over recent decades (Côté et al., 2011). The current study employs the best knowledge acquired so far in this particular field of heat transfer in coarse granular materials. The next paragraphs summarizes some of the studies that the current research project is influenced by.

A comprehensive study of the action of frost on the ground was conducted in 1970–76 as a project called *Frost I Jord* (Frost in Soils). The results relating to frost heave problems and the thermal properties of granular materials are reported in Heiersted (1976). In particular, the chapter on thermal properties is mostly based on a doctoral thesis by Johansen (1975), who conducted a broad study of the thermal conductivities of soils. A minor part of his research was dedicated to natural air convection in coarse open graded materials. Johansen (1975) proposed a normalized thermal conductivity model that has been used as a basis for other models (Balland & Arp, 2005; Côté & Konrad, 2005b; Lu et al., 2007). Furthermore he proposed the limits of different heat transfer mechanisms as a function of degree of saturation (S_r) and effective particle diameter (d_{10}). His research outcomes serve as a basis for more recent studies on thermal conductivity and the natural convection of unbounded materials.

The next comprehensive study was conducted after the cold winters of 1995/1996 and 1996/1997, which caused excessive frost damage to railway lines, and focused on crushed rock materials. Subsequently the Norwegian Railway administration formed a research group and assigned the Norwegian Geotechnical Institute (NGI) to conduct research on the thermal properties of materials used in railway construction. The initial research results regarding thermal conductivity are reported in NGI (1996a), NGI (1996b) and NGI (1996c). The research found that frost damage on railway lines does not originate from high thermal conductivity alone: the excessive depth of the frost penetration was also a consequence of the natural air convection occurring in coarse materials. This study was continued, and results regarding natural air convection were reported in NGI (1999).

Later, Côté et al. (2011) conducted a study of air convection using natural cobbles as their test material. They successfully managed to use the experience of preceding studies running large-scale experimental tests (Johansen, 1975; NGI, 1999) to develop a new, optimized heat transfer cell. They also employed an analytical Nusselt (Nu)–Rayleigh (Ra) number relationship proposed by Schubert and Straus (1979) to develop a method for the establishment of intrinsic permeability (K). Intrinsic permeability largely defines the extent of natural air convection under certain environmental conditions.

To summarize, the transition from the use of gravel material to crushed rock material has not been backed with a sufficient amount of experiment-based knowledge. Although the current regulations are a good advancement, they can still be interpreted in such a way as to allow the use of materials that have a negative effect on frost protection. The studies by Johansen (1975), NGI (1999), Côté et al. (2011) and Côté and Konrad (2005b) are the cornerstones of this doctoral thesis and all of the associated papers. Their work has been used to investigate the thermal properties and limits of natural air convection.

1.2 Research scope and objectives

The primary scope of this research is the investigation of the heat transfer characteristics of unbound materials in road and railway structures. These materials include crushed rock and lightweight aggregates. The research includes several directions of scientific investigation.

A part of the study focuses on thermal conductivity experiments on unfrozen and frozen moist crushed rock materials and solid rock particles. A major part of the study is dedicated to investigating convective heat transfer and the establishment of intrinsic permeability. This part investigates not only crushed rock materials but also lightweight aggregates (expanded clay and foam glass material). Part of the research also focuses on the investigation of material performance under field environmental conditions. Finally, the research includes numerical modelling to validate the laboratory experiments and field observations.

The main objective of this research project is to investigate the heat transfer characteristics of unbound materials used in road and railway structures, with a focus on natural air convection.

The secondary objectives are:

i) development of general knowledge about crushed rock materials used for road and railway construction in terms of their heat transfer characteristics (conduction, radiation and convection);

ii) investigation of the thermal conductivity of solid particles (k_s) and methods of effectively estimating this;

iii) adoption of an existing thermal conductivity model and validation of laboratory measurements;

iv) investigation and establishment of the intrinsic permeability of various road construction materials (crushed rock and lightweight aggregates) based on large-scale laboratory experiments;

v) development of a numerical model for large-scale experiments to account for imperfections under laboratory conditions and to re-establish permeability;

vi) construction of a full-scale field test site to assess material performance and possible natural air convection under field conditions;

vii) development of a numerical model representing the field test site, using input parameters based on laboratory experiments.

1.3 Research approach

This study employed a multi-stage research approach that allowed the set of objectives to be tackled one at a time. This included conducting a literature review on the subject of heat and mass transfer, followed by small-scale (conduction) and large-scale (conduction, radiation and convection) laboratory experiments, and then by numerical modelling of large-scale experiments to account for imperfections under laboratory conditions. A field test site was constructed incorporating full-scale road and railway sections to observe material performance under field conditions. Finally, numerical modelling was carried out for the field test site with a focus on natural air convection. This last step involved using input parameters from preceding small- and large-scale laboratory-based studies and numerical modelling of large-scale experiments.

Figure 1 shows the interconnection between the different papers that make up this doctoral thesis. The study can be broken down into three parts: small-scale experiments (Papers V and VI), large-scale experiments including numerical modeling (Papers I, II, III and IV), and field observations and numerical modeling of two road sections (Paper VII). Paper VII employs the research outcomes from the two first parts.

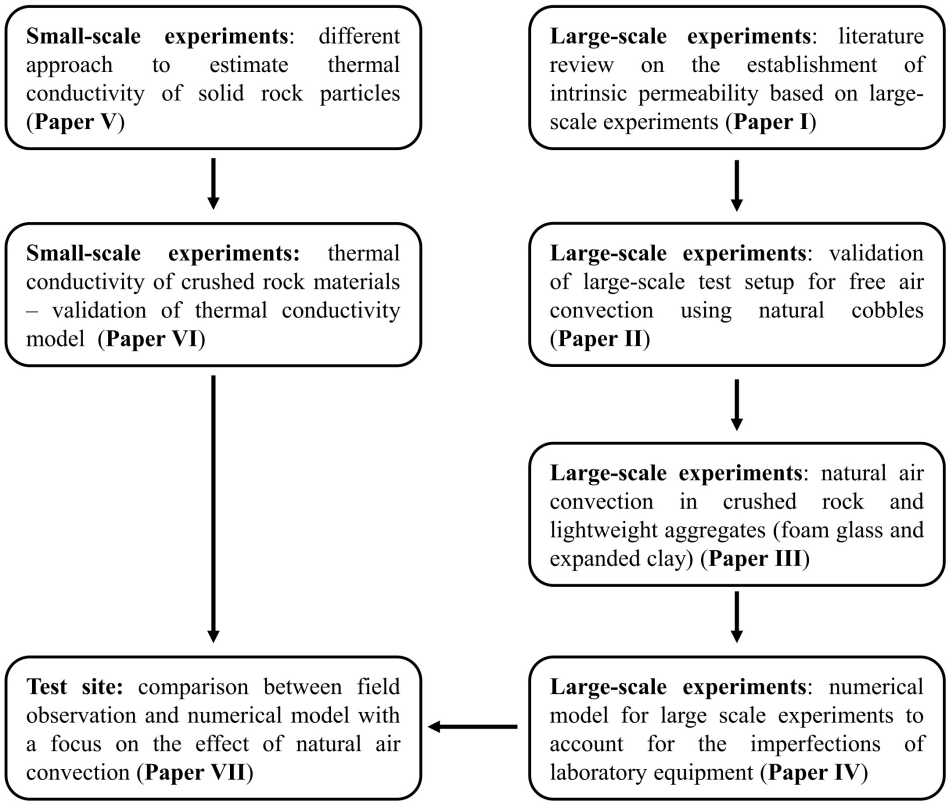

Figure 1. Flow chart of interrelation between different research scopes within this study

The results of the small-scale experiments are reported in two journal publications (Papers V and VI). Their primary objective was to validate and adapt an existing model for the estimation of the thermal conductivity of partly saturated crushed rock materials. Paper V is dedicated to the investigation of the thermal conductivity of solid particles (k_s). This is a crucial input parameter for the thermal conductivity model to ensure a reasonable estimation. Paper VI deals with the adaption and validation of an existing thermal conductivity model. In total more than 300 tests were carried out with unfrozen and frozen samples. These allowed the verification of a thermal conductivity model to use for further analysis on the field test site.

The part of the research associated with large-scale experiments was initiated by conducting a review of the literature on natural air convection tests and the establishment of intrinsic permeability based on experimental data (Paper I). After that the experimental setup used in this study was first validated for conduction, using a sand sample, and for convection, using a cobble sample (Paper II). Next, five different road construction materials were tested for natural air convection. The results are reported in Paper III. To account for imperfections in the laboratory experiments, a numerical model for a large-scale experimental setup was developed which allowed adjustment of the calculated intrinsic permeability values (Paper IV).

Paper VII discusses the potential for natural air convection in two road sections, one using open graded crushed rock material and the other with a foam glass layer. The paper gives a simple analysis based on the temperature gradient for convection-susceptible layers in combination with the experimentally determined intrinsic permeability values, and provides a numerical model that incorporates thermal properties based on models validated via small- and large-scale experimental setups.

An explanation of the interrelationship between the different parts of the collection of papers that make up this doctoral study is given in this section. The introduction (Chapter 1) gives an overview of the background to the study, the research scope, the main objectives and the research approach employed. This is followed by a brief theory of heat transfer in granular materials in Chapter 2, which presents the basic knowledge and theoretical models used to approximate different heat transfer mechanisms (conduction, radiation and convection), as well a method for establishing intrinsic permeability based on laboratory experiments. Chapter 3 provides information on the research methodology, with a detailed explanation of the small- and large-scale laboratory experiments, the field test site and the numerical models developed. The results and discussion, based on the research papers, are presented in Chapter 4. Conclusions and recommendations and future work are summarized in Chapter 5. The full-length papers are provided in Appendices A–F.

2 Theory of heat transfer in granular materials

This chapter provides the basis of the heat transfer theory and the models used in this study in relation to construction materials. Different heat transfer mechanisms occurring in soils and construction materials are introduced in section 2.1. The heat transfer mechanisms relevant to this study are discussed in the next three sections as follows: conduction (2.1), radiation (2.2), and convection (2.3). The last section (2.4) is dedicated to a method for establishing intrinsic permeability based on natural air convection tests. The different heat transfer mechanisms and the models for approximation and establishing permeability are used throughout the papers to analyze heat transfer in construction materials.

2.1 Different heat transfer mechanisms

Granular material has a complex structure consisting of randomly arranged solid particles of different shapes and sizes, with pore spaces between them. The pore can contain air, and water in its various forms: liquid, vapor or solid (Farouki, 1981). The type of heat transfer mechanism depends on the skeleton structure of the porous medium (solid particles) and the proportion and amount of air/water/ice in the pore space. Johansen (1975) conducted an extensive study of heat transfer in soils and defined the domains of different heat transfer mechanisms as a function of the degree of saturation (S_r) and effective particle size (d_{10}). Figure 2 shows these mechanisms as follows: 1) conduction; 2) temperature-driven vapor diffusion; 3) moisture-driven vapor diffusion; 4) natural water convection; 5) natural air convection; 6) radiation. As Figure 2 shows, in the majority of mineral materials heat is transferred by conduction. However, in coarse materials, radiation and convection can make a considerable contribution to the overall heat transfer rate. Hence all three heat transfer mechanisms (conduction, radiation and convection) must be addressed in the thermal design of road and railway structures. The thermal conductivity of crushed rock materials is discussed in Papers V, VI and VII, while heat transfer by convection, and to a lesser extent radiation, are discussed in Papers I, II, III, IV and VII.

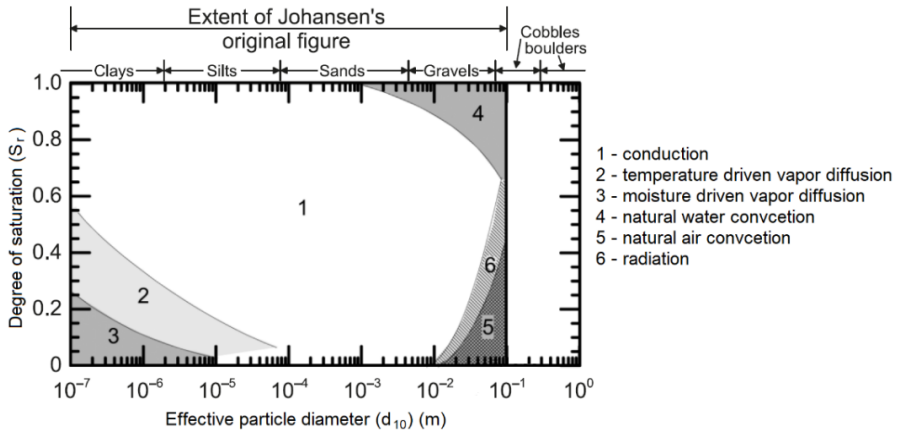

Figure 2. Heat transfer modes in soils (redrawn and adapted from Johansen (1975) by Côté et al. (2011))

The energy conservation equation defining the complex heat transfer in coarse granular materials can be expressed as follows (Howell et al., 2010):

$$[1] \qquad \nabla \cdot (k_c \nabla T) + \nabla q_r = C_s \frac{\partial T}{\partial t} + C_a q_a \cdot \nabla T$$

where k_c is thermal conductivity (W/m°C), ∇T is temperature gradient (°C/m), q_r is the radiative heat flux vector, C is the volumetric heat capacity (J/m^3·°C), with the subscripts "s" and "a" referring to solid and air phases respectively, T is the absolute temperature (K), t is time and q_a is the volumetric flux vector of air.

2.2 Heat transfer by conduction

Thermal conductivity is the governing heat transfer mode in the majority of unbound granular materials (Farouki, 1981; Johansen, 1975). Over the last decades, numerous theoretical (De Vries, 1963; Mickley, 1951; Smith, 1942) and empirical (Côté & Konrad, 2005b; Johansen, 1975; Kersten, 1949) models have been developed for dry, moist and saturated soils. Farouki (1981) reviews several of the thermal conductivity models available at that time and comes to the general conclusion that Johansen (1975) model gives the best estimates for the widest range of soils.

Johansen (1975) developed his model based on data gathered by Kersten (1949) on medium and fine sands and fine-grade soils. He proposes the approach of normalized thermal conductivity as follows:

$$[2] \qquad k_n = \frac{(k - k_{dry})}{(k_{sat} - k_{dry})}$$

where k_n is normalized thermal conductivity (W·m^{-1}·°C^{-1}), k is measured thermal conductivity (W·m^{-1}·°C^{-1}), k_{dry} is thermal conductivity in a dry state and k_{sat} is the thermal conductivity in a saturated state. Johansen (1975) then relates normalized thermal conductivity to the degree of saturation and proposes soil-type-dependent relationships. The normalized thermal conductivity model sets the upper and lower limits as follows:

$$[3] \qquad \begin{cases} S_r = 0 : & k = k_{dry} & \Rightarrow & k_r = 0 \\ S_r = 1 : & k = k_{sat} & \Rightarrow & k_r = 1 \end{cases}$$

Given its fairly good performance, as stated by Farouki (1981), Côté and Konrad (2005b) extended the model to make it applicable to other soil types to propose a generalized k_r-S_r relationship:

$$[4] \qquad k_n = \frac{\kappa S_r}{1 + (1 - \kappa) S_r}$$

where κ is an empirical parameter (no units) to account for different soil types as well as for unfrozen or frozen conditions, and S_r is the degree of saturation. For crushed rock materials the value of κ is set to 4.7 for unfrozen conditions and 1.8 for frozen conditions (Côté & Konrad, 2005b). However, for a given set of data the κ parameter may have to be adjusted, as in Paper VI as part of a thermal conductivity model calibration.

Dry thermal conductivity

Normalized thermal conductivity expresses the thermal conductivity of a given material in its dry and saturated states. Together with the generalized thermal conductivity model, Côté and Konrad (2005b) propose an equation for calculating k_{dry} as follows:

[5] $$k_{dry} = \chi \times 10^{-\eta n}$$

where χ ($W \cdot m^{-1} \cdot °C^{-1}$) and η (no units) are material parameters accounting for soil type and n is porosity. For crushed rock materials the values of χ and η are 1.7 W/m°C and 1.8 respectively. Eq.[5] presents k_{dry} as a function of porosity and soil type, but does not take thermal conductivity in the solid phase (k_s) into consideration. Later, Côté and Konrad (2009) proposed another equation for two-phase material to account for the variation of k_s:

[6] $$k_{dry} = \frac{(\kappa_{2p} k_s - k_f)(1-n) + k_f}{1 + (k_{2p} - 1)(1-n)}$$

where k_s and k_f are the thermal conductivity ($W \cdot m^{-1} \cdot °C^{-1}$) of the solid and fluid (air) phases respectively, and κ_{2p} is a structure parameter (no units) defined as:

[7] $$\kappa_{2p} = 0.29 \left(15 \frac{k_f}{k_s}\right)^{\beta}$$

where β is an empirical parameter accounting for structure. When the k_f/k_s ratio is lower than 1/15, the empirical value of β for crushed rock material is 0.54.

The two equations for estimating k_{dry} were applied to test the effect on the model's performance (discussed in more details in Paper VI).

Saturated thermal conductivity

Although with no physical basis, the geometric mean method results gives reasonable estimates of saturated thermal conductivity (Johansen, 1975; Sass et al., 1971). The saturated thermal conductivity of unfrozen and frozen materials can be calculated as follows:

[8] $$k_{sat(u)} = k_s^{1-n} \times k_w^n \qquad \text{(unfrozen)}$$

[9] $$k_{sat(f)} = k_s^{1-n} \times k_i^n \qquad \text{(frozen)}$$

where k_w is the thermal conductivity of water (W/m°C) and k_i is the thermal conductivity of ice (W/m°C).

Thermal conductivity of solid particles

The equation for calculating k_{dry} (Eq.6) and k_{sat} (Eqs.8 and) require k_s as an input parameter. Where the composition and proportion of each mineral are known, a generalized geometric mean method can be used to estimate k_s as follows:

[10] $$k_s = \prod_{j=1}^{z} k_{mj}^{x_j} \quad \text{with} \quad \sum_{j=1}^{z} x_j = 1$$

where $\prod$ is the product of the thermal conductivity of each mineral km raised to the power of its volumetric proportion x in the rock. This method is used successfully in several studies (Côté & Konrad, 2005b; Sass et al., 1971; Woodside & Messmer, 1961). However, it

requires precise knowledge of the rock-forming minerals present. Paper V discusses and compares the different ways of measuring or estimating k_s.

Calculation of thermal conductivity

The thermal conductivity of unfrozen (k_u) and frozen states (k_f) can then be calculated by rearranging Eq.2 as follows:

[11] $$k_u = (k_{sat(u)} - k_{dry})k_{nu} + k_{dry}$$

[12] $$k_f = (k_{sat(f)} - k_{dry})k_{nf} + k_{dry}$$

where k_{nu} and k_{nf} correspond to the normalized thermal conductivity of unfrozen and frozen conditions, and subscripts "u" and "f" correspond to unfrozen or frozen conditions.

The thermal conductivity model introduced in this chapter was adapted and validated with extensive laboratory measurements of moist and saturated samples. Paper V presents a discussion of the thermal conductivity of k_s. This is subsequently used as an input parameter for the model adoption presented in Paper IV. The adaption of the model was mostly related to bets-fitting the parameters accounting for soil type.

2.3 Heat transfer by radiation

Solving radiation heat transfer equations in complex geometries such as porous media can be difficult. However, in granular materials the particles are opaque and are therefore only affected by their neighbors, hence radiation in such conditions can be expressed as a diffusion process (Xue et al., 2007). Because radiation flows in the same direction as thermal conduction it can be assessed in the form of Fourier's law through diffusion approximation (Howell et al., 2010). As a result, the effective thermal conductivity (k_e) can be expressed as the sum of the contribution of pure conductivity (k_c) and equivalent radiant conductivity (k_r) as follows:

[13] $$k_e = k_c + k_r$$

where k_e is effective thermal conductivity ($W \cdot m^{-1} \cdot °C^{-1}$) and k_r is the equivalent radiant conductivity ($W \cdot m^{-1} \cdot °C^{-1}$).

Radiation can make a considerable contribution to the overall heat transfer rate only when pore size is large enough to induce a significant temperature difference in the interparticle space. This is clearly demonstrated in Fillion et al. (2011) study, which compares effective thermal conductivity when material size is increased from sand to cobbles. The effect of radiation is also shown in Figure 2 in this study, where Johansen (1975) defines the limit of d_{10} of 10 mm, above which radiation can make a considerable contribution. Equivalent radiant conductivity can be calculated with Eq.14, as stated by Tien (1988):

[14] $$k_r = 4Ed_{10}\sigma T^3$$

where E is the exchange factor (no units), σ is the Stephan-Boltzmann constant equal to 5.67×10^{-8} $Wm^{-3}K^{-4}$ and T is the mean porous medium temperature (K). The literature provides numerous equations for approximation of the exchange factor. Fillion et al. (2011) in a study of radiation in coarse materials uses seven different equations to determine the one

that fits the model best. They found that the equation proposed by Argo and Smith (1953) gave the most satisfying results with the materials tested:

$$[15] \qquad E = \frac{\varepsilon}{(2-\varepsilon)}$$

where ε is surface emissivity (no units).

Substituting k_c with Eq.6 and k_r with Eq.14 in Eq.13 yields:

$$[16] \qquad k_e = \frac{(\kappa_{2p}k_s - k_f)(1-n)+k_f}{1+(k_{2p}-1)(1-n)} + 4Ed_{10}\sigma T^3$$

Eq.16 is a model for effective thermal conductivity in a two-phase material, accounting for the contribution for pure conduction and radiation heat transfer. Papers I and III discuss the model together with experimental data on coarse materials.

In a similar manner, in Eq.1 the k_c term accounting for conduction in coarse materials can be substituted by k_e. Hence Eq.1 can be rewritten as (Kaviany, 1999):

$$[17] \qquad \nabla \cdot (k_e \nabla T) = C_s \frac{\partial T}{\partial t} + C_a q_a \cdot \nabla T$$

2.4 Heat transfer by convection

Natural air convection can be induced in coarse materials under upward heat-flow conditions. Under these conditions, the density variations of fluid (air) along the temperature gradient can become unstable. As a result, warmer air starts rising while colder (denser) air flows downwards (Côté et al., 2011; Goering et al., 2000). In such conditions, natural air convection is promoted when Rayleigh number (Ra) exceeds the critical value of $4\pi^2$ (critical Ra_c~40). As Nield and Bejan (2013) state, Ra can be calculated as follows:

$$[18] \qquad Ra = \frac{g\beta C K H^2 \nabla T}{\nu k_e}$$

where g is gravitational acceleration ($m \cdot s^{-2}$), and β, C and ν are thermal expansion (K^{-1}), heat capacity ($J \cdot m^{-3} \cdot K^{-1}$) and the kinematic viscosity ($m^2 \cdot s^{-1}$) of the fluid (air) respectively, K is intrinsic permeability, H is the sample (layer) height (m), and ∇T is the temperature gradient ($°C \cdot m^{-1}$) over the sample (layer).

In configurations where the temperature gradient is applied vertically, the downward heat flow is characterized by effective thermal conductivity. Natural air convection can increase the heat flow in upward heat-flow conditions if the temperature gradient exceeds the critical value. The ratio between the downward and the upward heat flux values is expressed as a Nusselt number that is widely used as another means of characterizing natural air convection:

$$[19] \qquad Nu = \frac{q\uparrow}{q\downarrow}$$

where $q \downarrow$ is the measured downward heat flux ($W \cdot m^{-2}$) (conduction and radiation) and $q \uparrow$ is the upward heat flux ($W \cdot m^{-2}$) (convection). Ra and Nu are related to one another with a specific relationship for the given geometry and boundary conditions. The relationship can be used to establish the intrinsic permeability of coarse materials based on large-scale experiments.

2.5 Intrinsic permeability

Intrinsic permeability is a crucial parameter controlling air and heat flow in coarse materials (Goering & Kumar, 1999). Côté et al. (2011) clearly demonstrate increasing permeability with increasing d_{10}. This in turn leads to lower critical gradients required to initiate air convection. However, measuring the permeability of coarse materials can be difficult. Conventional methods of measuring hydraulic conductivity may be hard to apply due difficult control over excessively large water flows. In addition, turbulent flows may form at relatively low hydraulic gradients (Dudgeon, 1966).

Côté et al. (2011) demonstrate how large-scale air convection tests can be used as an alternative method for establishing the intrinsic permeability of coarse materials. The method is based on the Nu-Ra relationship given by Schubert and Straus (1979). They offer an analytical solution to a Nu-Ra relationship for a square enclosure heated from below, from which Côté et al. (2011) derive best-fit equation:

[20] $$\mathrm{Nu} = 1.735 \ln(\mathrm{Ra}) - 5.38$$

By substituting the Nu with Eq.19 and the Ra with Eq.18 in Eq.20 they obtain:

[21] $$\frac{q\uparrow}{q\downarrow} = 1.735 \ln\left(\frac{g\beta C K H^2 \nabla T}{\nu k_e}\right) - 5.38$$

Eq.21 can then be used in combination with experimental results, using K as a best-fit parameter allowing establishment of the K values. This method was very valuable in this study for determining the intrinsic permeability of road and railway construction materials for the analysis of natural air convection under field conditions.

Many studies investigating natural air convection have relied on empirical or semi-empirical models for their estimation of K values. In this study the established K values are compared to two semi-empirical models derived from hydraulic radius theory (Poiseuille, 1844) by Kozeny (1927) (Eq.22) and Chapuis (2004) (Eq.23) as follows:

[22] $$K = \frac{C}{f^2} d_{10}^2 \frac{n^3}{(1-n)^2}$$

where the C/f^2 accounts for tortuosity as well as pore and particle shape (no units), and

[23] $$K = 0.000125\alpha^{0.7825}$$

where α is $d_{10}^2 \cdot n^3/(1-n)^2$

The method for establishing intrinsic permeability based on the Nu-Ra relationship is a cornerstone of this study's analysis of air convection in road and railway materials. The method and theoretical equations (Eqs.22 and 23), validated with K values derived using this method, are used throughout most of the papers associated with this study. The method is first put into perspective by analyzing preceding large-scale experiments on natural air convection, as presented in Paper I. Afterwards, the method is used in validation studies of large-scale experiments and the results compared with those of other studies using similar materials (Paper II). The method is further used to establish the intrinsic permeability of different road construction materials (Paper III). Paper IV presents a numerical model adjusting the Nu-Ra relationship and subsequently re-establishing K values. Finally, Paper VII**,** dealing with the field test results and modeling, uses intrinsic permeability values

derived from laboratory tests to analyze the extent of natural air convection under different environmental conditions.

3 Research methodology

This chapter explains the research methodology used in this study. The chapter is subdivided into three sections as follows: section 3.1 presents the laboratory measurements, with descriptions of small-scale and large-scale experiments, 3.2 presents the field-test site measurements, and 3.3 describes the modelling, including the models for large-scale experiments and field test site.

3.1 Laboratory measurements

3.1.1 Small-scale laboratory experiments

Small-scale laboratory experiments were used primarily for determination of the thermal conductivity of various crushed rock materials and to adopt and validate a thermal conductivity model (Eq.11 and 12) (Paper VI). As part of the study, a comparison of different methods of approximation for the thermal conductivity of solid particles was carried out (Paper V).

Figure 3 shows the cross section of a small-scale experiment setup. Two different test setups were used, with a variation in the heat flux sensors. For the test setup depicted in Figure 3, borosilicate glass discs (see Figure 4a) were used as heat flux sensors. The other test setup was equipped with heat flux meters (see Figure 4b). The test setup was built following that used by Côté and Konrad (2005a) and comprises a test sample with a height and diameter of 75 and 100 mm respectively. The sample is compacted in a PVC mold with an outer diameter of 110 mm and a height equal to that of a sample. The sample is placed between two heat flux sensors. The borosilicate glass discs have thermocouples embedded in their flat surfaces. Borosilicate glass is a material with known thermal conductivity which varies fairly minimal in temperature range used in these experiments. At a temperature of -7°C its thermal conductivity is 1.03 W/m°C, while at 7°C it is 1.05 W/m°C. The heat flux plates have a series of thermocouples which generate a voltage that is sensitive to heat flux, and five independent thermocouples providing temperature readings. The heat flux sensors make it possible to measure heat flux and temperature gradient imposed on the sample.

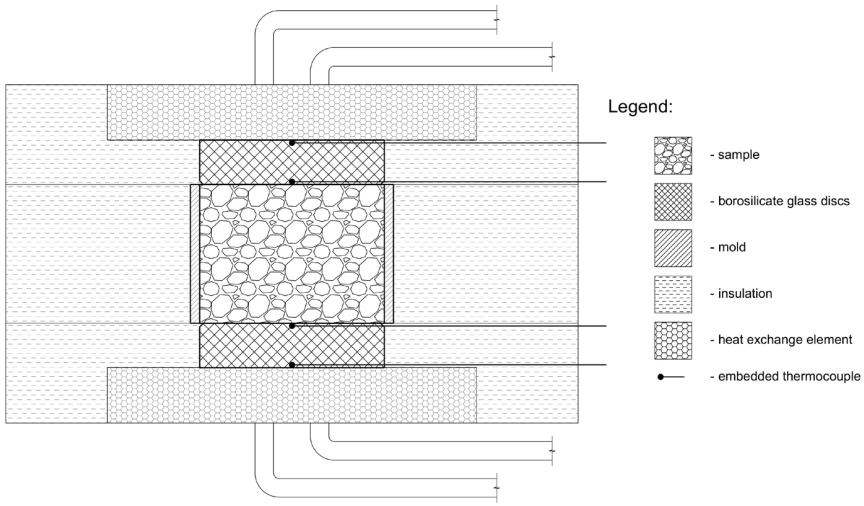

Figure 3. Cross section of small-scale experimental setup (with borosilicate glass discs)

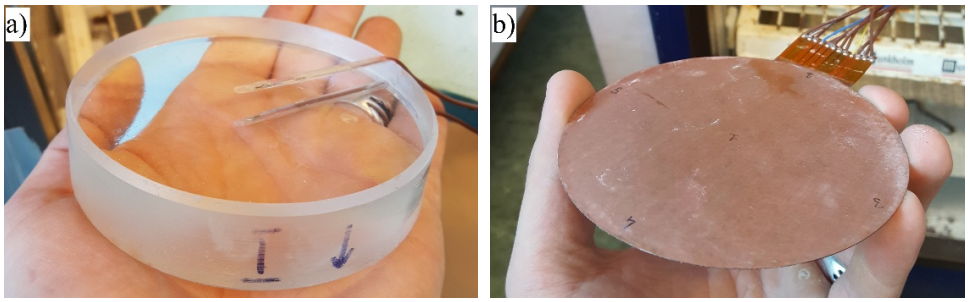

Figure 4. Heat flux sensors: a) borosilicate glass disc; b) heat flux plate

The three-layer system (heat flux sensor – sample – heat flux sensor) was placed between two independent heat exchange plates. The samples were tested in unfrozen and frozen conditions. For the unfrozen tests the temperatures at the top and bottom were set to approximately 7° and 3°C respectively. For the frozen tests, the temperatures were set to -3° and -7°C.

Small-scale experiments use steady-state conditions to determine the thermal conductivity of the test material. For steady-state conditions Fourier's law can be applied, and in the case of this experimental setup, the expression for calculating thermal conductivity is as follows:

[24] $$k = \frac{q_{uf}+q_{lf}}{2} \cdot \frac{h_s}{(T_T - T_B)}$$

where k is the thermal conductivity of the test material ($W \cdot m^{-1} \cdot °C^{-1}$), q_{uf} and q_{lf} are the heat flux values from the upper and lower heat flux sensors ($W \cdot m^{-2}$), h_s is the sample thickness (m) and T_T and T_B are the temperatures at the top and bottom of the sample (°C).

Materials

Paper V presents the study using the small-scale experimental setup to determine thermal conductivity of solid particles (k_s). The results of Paper V are used as input parameters for

the preceding study (Paper VI) of the adoption and calibration of the thermal conductivity model (Eqs.11 and 12) for crushed rock materials.

The test materials were samples, all with different mineralogical compositions, from nine quarries in Norway: Legruvbakken, Hellvik, Hello, Vassfjell, Hadeland, Meraftåsen, Rombak, Aplitt and Hanestad (see Table 1, below). The values of two different samples were used to determine k_s. First, direct measurements of thermal conductivity (k_s) were conducted on the rock core samples (Figure 5a). Second, saturated samples with a particle size of 1/2 mm were used (see Figure 5b). These tests yielded measurements of thermal conductivity in the saturated state. Subsequently, Eq.8 can be used to back-calculate the thermal conductivity of the solid phase. Table 1 also gives the thermal conductivity values for each mineral. These values were used together with Eq.10 as an alternative way to define k_s. Tests using partly saturated samples (Paper VI) were carried out on crushed rock material with a particle size of 0/16 mm (see Figure 5c). Figure 6 shows the grain size distribution in the test material. The gradation curve is based on Fuller's curve, setting the fines content at 7%, corresponding to an intermediate value that is allowed for materials used for frost protection layers.

Table 1. Mineralogical composition of test materials

Mineral (%)	Legruvbakken	Hellvik	Hello	Vassfjell	Hadeland	Meraftåsen	Rombak	Aplitt	Hanestad	Thermal conductivity,* W/mK
Quartz	36	-	8	<1	7	5	46	29	81	7.69
Plagioclase	33	78	20	21	54	33	28	37	4	1.96
Pyroxene	-	2	1	1	4	2	2	-	-	4.93
Amphibole	4	-	49	35	2	10	-	<1	-	2.81
Epidote	6	-	16	-	-	18	-	-	-	2.83
Chlorite	13	2	6	10	-	19	3	2	<1	5.15
K-feldspar	4	4	-	2	32	3	-	13	13	2.49
Clinozoisite	-	6	-	30	-	-	-	6	-	2.40
Calcite	<1	-	-	<1	<1	6	2	-	-	3.59
Sphalerite	-	-	-	<1	-	<1	-	-	-	12.73
Biotite	5	-	-	-	<1	-	12	-	-	2.02
Muscovite	-	6	-	-	-	3	7	2	3	3.48
Rhodochrosite	-	-	-	-	-	<1	-	-	-	3.00
Magnesite	<1	-	-	-	-	-	-	-	-	5.10
Chalcopyrite	-	<1	-	-	-	-	-	-	-	8.20
Pyrite	-	-	-	-	<1	-	<1	-	-	19.21
Dolomite	-	-	-	-	-	-	<1	-	-	5.51
Garnet	-	-	-	-	-	-	<1	-	-	3.4
Prehnite	-	-	-	-	-	-	-	10	-	3.57

**Thermal conductivity from Horai (1971) and converted to SI units in Côté and Konrad (2005b)*

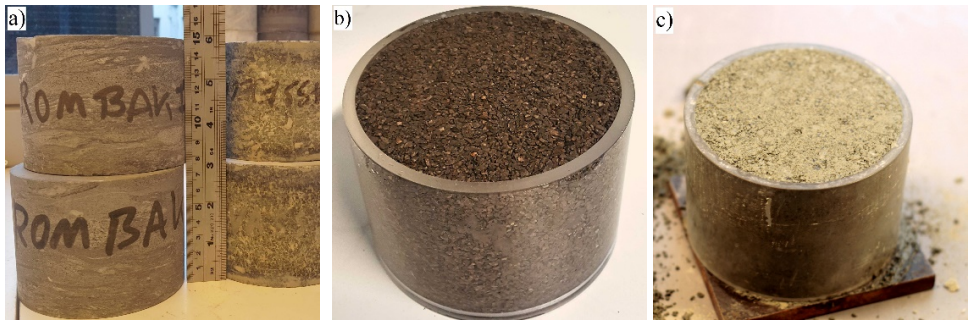

Figure 5. Materials used for small-scale experiments: a) rock core samples; b) saturated sample of crushed rock material with particle size of 1/2 mm; c) moist samples of crushed rock material with particle size of 0/16 mm

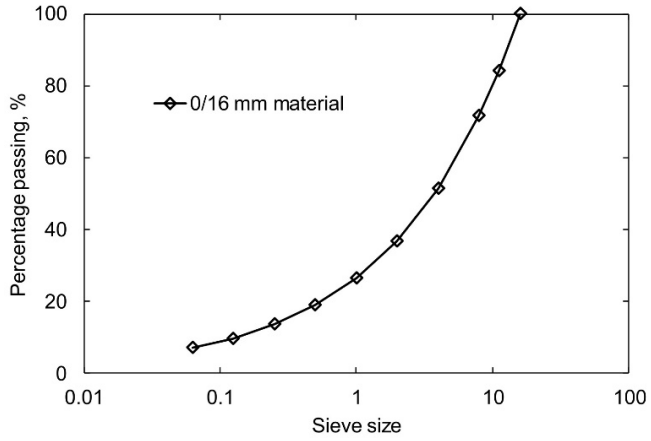

Figure 6. Grain size distribution for 0/16 mm material samples

3.1.2 Large-scale laboratory experiments

The setup for the large-scale test (heat transfer cell) was used primarily to measure natural air convection and establish intrinsic permeability (K) based on the experimental results. This test setup also made it possible to measure effective thermal conductivity and compare it with the theoretical contribution of pure conduction and radiation. The test setup was inspired by and based on the study by Côté et al. (2011), with a few modifications to improve the characterization of natural air convection, as presented in the next paragraphs.

Figure 7 shows a cross section of the experimental setup comprising an insulated box with an inner volume of about $1m^3$. The outer shell of the box is made of polyisocyanurate foam boards with a thickness of 100 mm. An extra layer of insulation is attached to the inner walls in the form of XPS boards with a thickness of 115 mm. There is a 2 cm and a 5 cm sand layer placed beneath and on top of the sample respectively. The top sand layer was separated from the sample with a layer of geotextile. This prevented the sand from percolating into the sample. The sand layers were included primarily to ensure good heat transfer between the sample and the heat exchange plates. The sample height for all of the tests was set to 0.98 m. We made the minor improvement of a more cube-shaped sample than

that used by. However, as shown in the numerical model presented in Paper IV, this had a rather insignificant influence on the resulting Nu-Ra relationship.

The temperature was controlled during the tests by two independent heat exchange plates, one placed at the top and one at the bottom of the sample, imposing a vertical temperature gradient alternating between upward and downward heat flow conditions. The heat exchange plates were made of a double copper tube circuit placed between two aluminum sheets. The voids between the copper tubes were filled with quartz sand to ensure uniform temperature and thermal stability. The heat exchange plates were powered by two independent cryostat units capable of maintaining the desired temperature range for the tests (5–40°C).

During the tests, the heat flux was measured by nine independent heat flux meters (Captec Entreprise) with a size of 0.3x0.3 m (see Figure 8a). The heat flux plates were placed between two 5 mm thick Plexiglass sheets over the top sand layer. The nine heat flux sensors covered 81% of the sample's top surface area. This is a considerable improvement compared the test setup used by Côté et al. (2011), where only four heat flux sensors were used, accounting for 64% of the sample's top surface area. In addition, having nine heat flux plates allowed more precise characterization of the air convection cells.

The temperature profile was measured by 45 thermocouples. The temperature sensors where placed at several levels 16-17 cm apart. The approximate positions are shown in Figure 7. In each layer, one thermocouple was placed at the center of the sample and the other four were placed about 16 cm from each of the side walls. The thermocouples allowed visualization of the convective heat transfer, and more importantly, calculation of the average temperature gradient imposed on the sample.

To be able to analyze the natural air convection and establish the intrinsic permeability (K), the tests were performed under downward and upward heat transfer conditions. The downward heat transfer corresponds to conditions where convection is not initiated. In this case the warmer (less dense) air is at the top of the sample, resulting in a stable density gradient. The heat for downward heat flow conditions in coarse materials is transferred by a combination of conduction and radiation. The downward heat flow test makes it possible to calculate the effective thermal conductivity. This can be done by measuring the average heat flux and temperature gradient over the sample and using the following equation:

$$[25] \qquad k_e = \frac{q\downarrow}{\nabla T}$$

The upward heat flow conditions correspond to a coupled heat transfer by conduction, radiation and convection. To initiate convection in a two-dimensional pattern (face to face), a line heat source was placed at one of the bottom edges of the heat transfer cell. The line heat source consisted of a metal pipe with circulating fluid maintained at 80°C, powered by an independent cryostat unit. After initiating the air convection the line heat source was turned off. The upward heat flow tests made it possible to measure the increase in heat transfer due to convection (expressed as a Nu number in Eq.19). In addition, intrinsic permeability could be established based on Eq.21 using input parameters from tests and calculating the value of k_e from the downward heat flow tests.

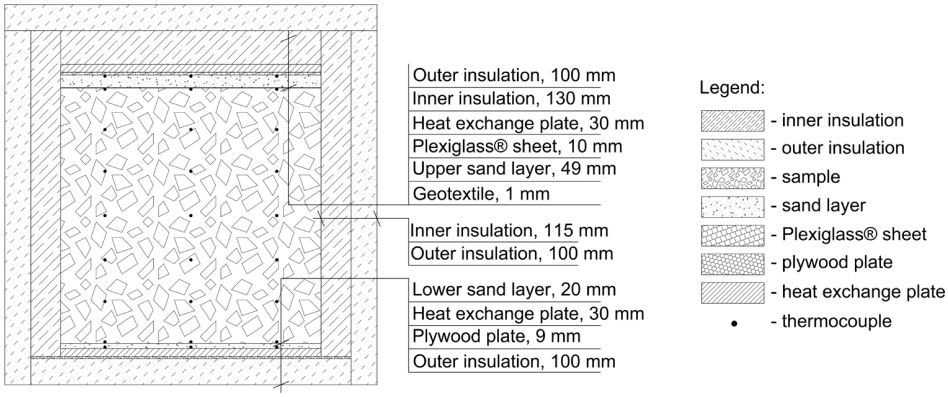

Figure 7. Cross-section of experimental test setup

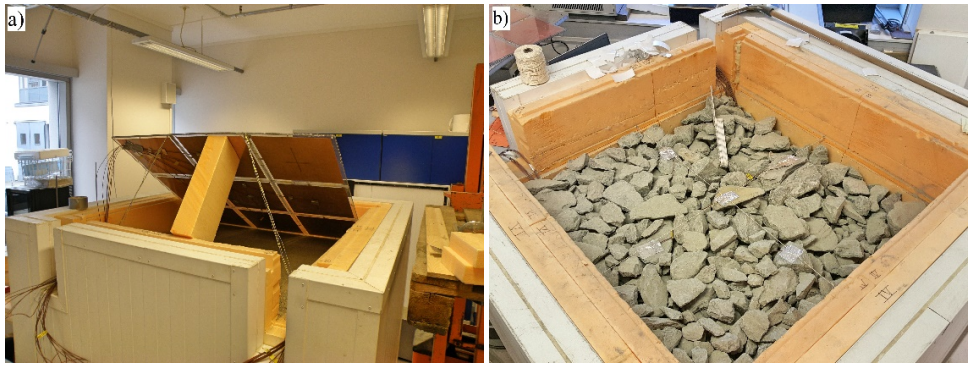

Figure 8. Large-scale experiments: a) heat flux plates; b) crushed rock material sample

Materials

The tests using the heat transfer cell were conducted in three stages. The first stage was the setup validation using sand. This stage validated the test setup for conduction heat transfer. The second stage was the validation of the convective heat transfer, using natural cobbles with a particle size of 0.09–0.21 m. This material was very similar to that used by Côté et al. (2011), hence the test results could be comparable to validate the convective heat transfer. The results of the first two validation stages are presented and discussed in Paper II. The third stage involved tests using road construction materials as follows a) three crushed rock materials with particle sizes of 20/120, 40/120 and 20/250 mm (an example of 20/120 mm material is given in Figure 8b); b) two expanded clay materials with particle gradation of 10/20 mm and 0/32 mm; c) foam glass material with particle gradation of 10/60 mm (see Figure 9 for grain size distribution). The test results for the third stage are presented in Paper III**,** except for the results of the tests with 10/20 mm expanded clay material. These tests were carried out later and are included in the results section of this study.

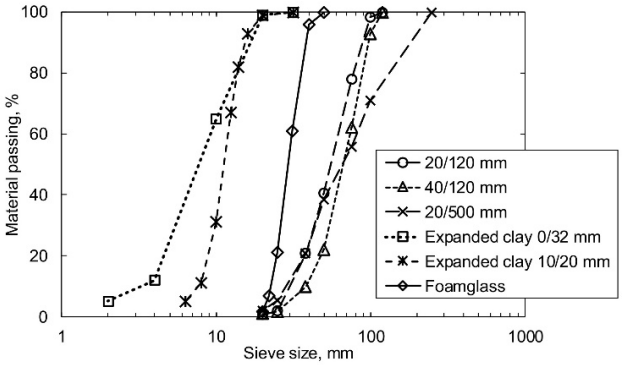

Figure 9. Material grain size distribution

3.2 Field test site

The laboratory experiments can give good information about materials' thermal properties. However, the physical and thermal boundary test conditions may not represent reality. To see the materials' response under real environmental conditions, a field test site was constructed. The test site incorporated a 48 m stretch of road with 6 different sections and a 32 m stretch of railway with 4 different sections. Each stretch was 6 m wide. A full description of the materials and instrumentation used for each section is given in the next subchapters. Figure 10 shows the completed road and railway stretch (no rails or sleepers were constructed). The primary objective of the field test site was to test different road and railway materials for their thermal response and performance.

The test site provided a vast amount of data over a period of two winters (2016/2017 and 2017/2018). The current research focused more on field observations of convective heat transfer. The results from field observations of two road sections (Ro1 and Ro6, see Figure 11) possibly allowing for natural air convection during the winter season, are given in Paper VII, which also includes numerical modelling of the two sections. For this purpose, the input parameters from preceding laboratory studies (small- and large-scale tests) were used.

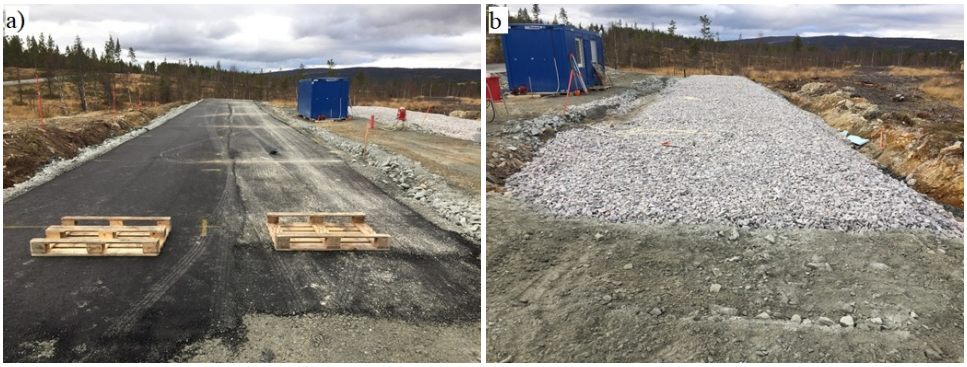

Figure 10. Completed field test site: a) road stretch; b) railway stretch

3.2.1 Location of the field test site

The field test site is situated in the Trøndelag region of Norway, a few kilometers outside Røros. The construction of the test site took place during the fall of 2016 and was finished shortly before the freezing season. Several test site locations (existing roads and off-road areas) were considered during the design phase. The final decision was based on the severe winter conditions in this region: the mean annual temperature in the region is only 0.4°C and the FI_{10} and FI_{100} freezing indexes are 38019 and 59719°C·h respectively.

The test site was constructed on an off-road area that is not subjected to traffic loading. However, proper winter maintenance (snow plowing) was carried out on both stretches, allowing a buildup of only a shallow snow/ice layer.

3.2.2 Cross section and instrumentation of road sections

Figure 11 shows cross sections of all six road sections (longitudinal view). The sections can be divided into two groups based on their structural layers (crushed rock material and lightweight aggregates). The first three road sections (Ro1–Ro3) focus on the effect of different gradations of the frost protection layer. The other three sections (Ro4–Ro6) were built to investigate the effects of different lightweight aggregates: expanded clay and foam glass.

The first three road sections were constructed with a 0.05 m thick asphalt layer, a 0.2 m thick base layer (0/32 mm crushed rock), a 0.8 m thick subbase layer (20/120 mm crushed rock), and a 1.0 m thick frost protection layer (FPL). The variation among these three sections is in the material grain size distribution used for the FPL. A detailed grain size distribution of all the materials is given in section 3.2.4. The total thickness of the superstructure for the first three road sections was 2.05 m. These sections were not designed in accordance with Handbook N200 (2014). The primary design intention was to create a road structure that would freeze through into the silt layer under relatively mild winter conditions.

The other three road sections were constructed with the same thickness of asphalt and base layer, a 0.2 m thick subbase layer (20/120 mm crushed rock), a 0.6 m thick lightweight aggregate layer, and a 0.7 m thick lower frost protection layer (LFPL) (0/120 mm crushed rock). The variation among road sections Ro4–Ro6 is in the type of lightweight aggregate used. Material gradations are given in section 3.2.5. Road sections Ro4–Ro6 were designed according to Handbook N200 (2014) for this area with FI_{10} as the frost index. The frost front should not penetrate the underlying subsoils in a winter with a FI_{10} freezing index.

All sections have an artificial layer of silt material beneath them. A 0.5 m thick layer was constructed below road sections Ro1–Ro3 and a 0.8 m layer was placed below road sections Ro4–Ro6. The silt layer was placed primarily in order to observe a possible frost heave if the frost front penetrates the superstructure. The natural subsoil below the silt layer is clay.

All six road sections are equipped with thermocouples for measuring temperature distribution through the layers. The thermocouples are placed on the interface between the different layers and in the middle part of most of the layers (approximate locations are shown in Figure 11). Most of the upper thermocouples in each section are embedded in the asphalt layer at a depth of about 1 cm. The measurements from these thermocouples were used to set

the boundary conditions in the numerical modeling of road sections Ro1 and Ro6. ThetaProbe ML3 moisture sensors were placed at different locations throughout the road sections, as shown in Figure 11. Two heat flux meters were embedded in the asphalt layer. LVDT-based frost heave sensors were placed in the silt layer in each section. In addition, there is a sensor in the frost protection layer in road section Ro2. Paper VII, investigating field measurements, employs only the data from the thermocouples and part of the data from the moisture sensors.

3.2.3 Cross section and instrumentation of railway sections

Figure 12 shows the cross section and instrumentation of the railway sections. All four railway sections have the same structural layers. The variation in these sections is in the mineralogy and particle gradation of the sub-ballast layer. The railway sections were constructed with a 0.5 m thick ballast layer (32/63 mm crushed rock), a 0.7 m thick sub-ballast layer (crushed rock), and a 0.8 m thick FPL (0/120 mm crushed rock). All sections have an artificial 0.5 m layer of silt beneath them. The natural subsoil below the silt layer is clay. The material gradation for each layer is given in section 3.2.6.

All of the railway sections are equipped with thermocouples located in the approximate positions, as shown in Figure 12. LVDT based frost heave sensors were placed in the silt layer in sections Rw1–Rw3, and a moisture sensor were placed in the silt layer in each of sections Rw1 and Rw4.

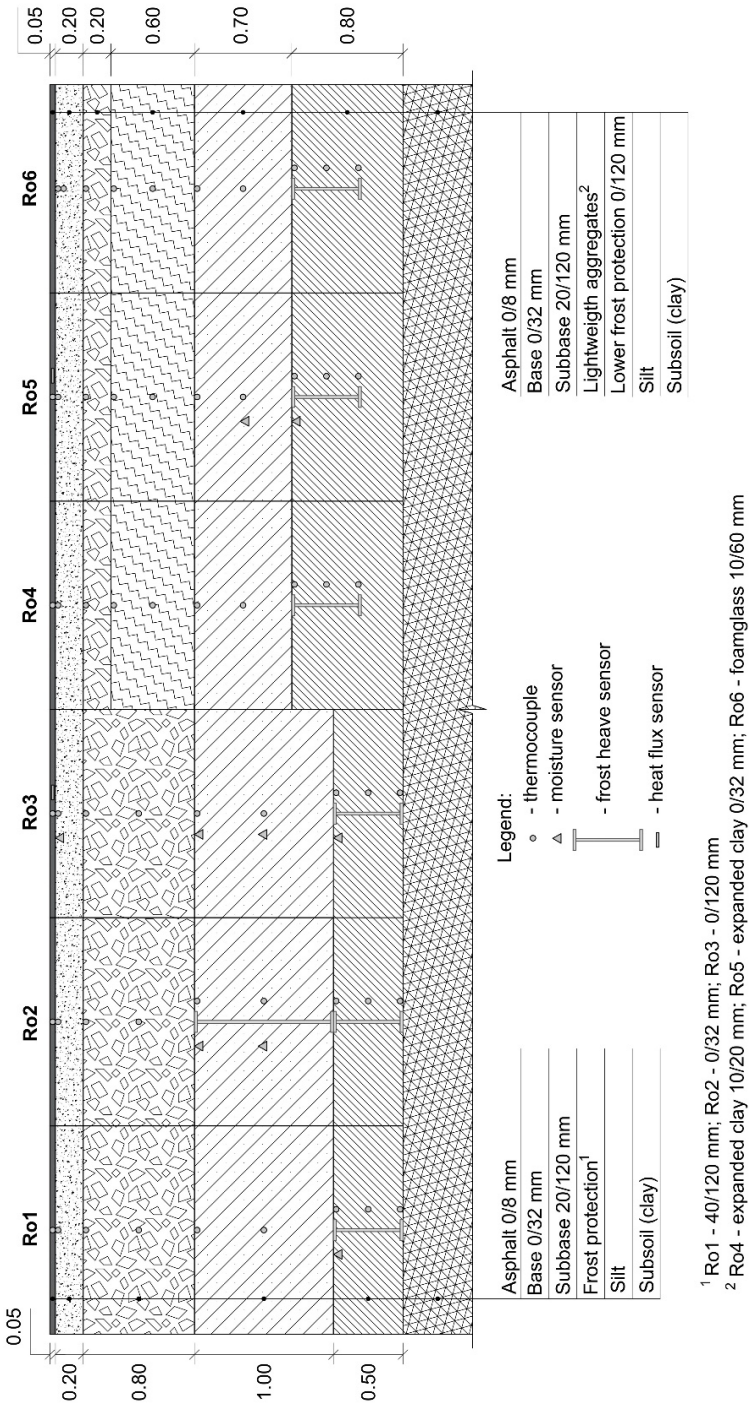

[1] Ro1 - 40/120 mm; Ro2 - 0/32 mm; Ro3 - 0/120 mm
[2] Ro4 - expanded clay 10/20 mm; Ro5 - expanded clay 0/32 mm; Ro6 - foamglass 10/60 mm

Figure 11. Cross section of road sections

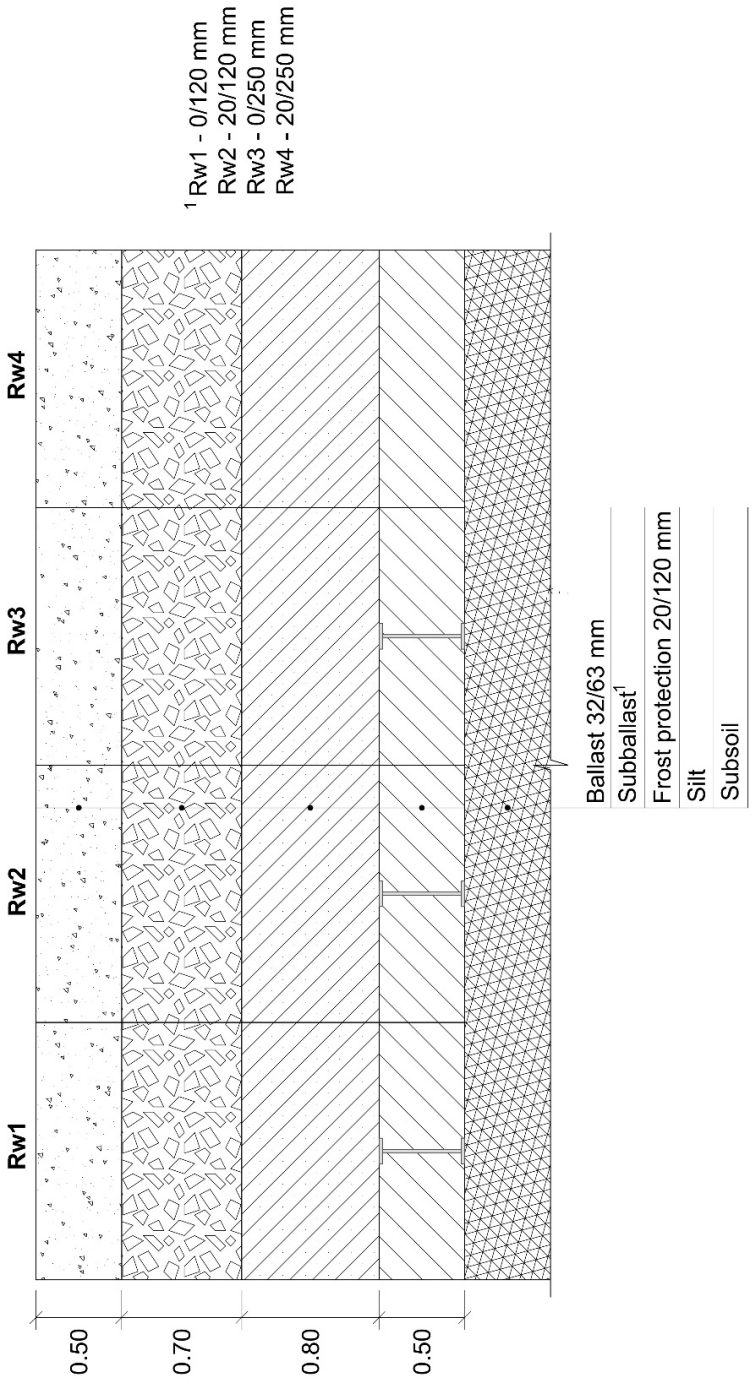

Figure 12. Cross section of railway sections

3.2.4 Materials used for road sections Ro1–Ro3

Figure 13 shows all of the crushed rock materials used in the first three road sections: a) three frost protection materials with different particle gradations, and b) the base and subbase layer materials. The grain size distribution of all the crushed rock materials are given in Figure 14. The base (0/32mm) and subbase (0/120 mm) layers have the particle gradation typically used for these layers. The subbase material has an open graded grain size distribution and is hence prone to natural air convection due to the relatively large pores. Because of this, the material was tested using the large-scale experimental setup (Paper III) to determine its permeability and define the critical temperature gradient that initiated air convection.

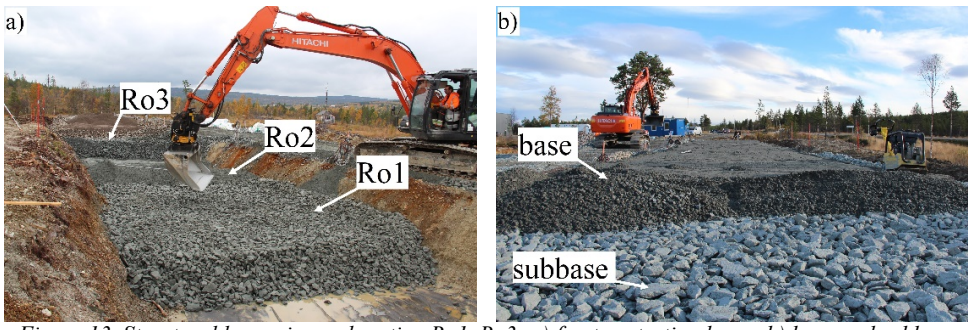

Figure 13. Structural layers in road section Ro1–Ro3: a) frost protection layer; b) base and subbase layer

The frost protection layers in the first three road sections were constructed of materials with different grain size distributions. All three materials were designed in accordance with Handbook N200 (2014). However, each material represent a significantly different case for gradation that the regulations allows to use. The crushed rock materials in all six road sections had the same mineralogical composition (see Legruvbakken material in Table 1).

The FPL for Ro1 was constructed using an open graded material. While this material was defined as 40/120 mm to distinguish it from other materials, it contained a small fraction below the lower limit of 40 mm to fit the requirements set by Handbook N200 (2014). This material is referred to here as *open graded FPL*. It is characterized by a large pore structure and represents a theoretical upper limit for the materials that can be used for the frost protection layer. This material was expected to be prone to natural air convection, which would compromise its insulating properties and its sole purpose, frost protection. A thorough discussion regarding the potential of air convection is presented in section 4.2 together with the large-scale experimental results.

Ro2 was constructed using a 0/32 mm dense graded crushed rock material. This material is characterized by large portion of fines (<63 μm) and represents the theoretical lower limit set by the regulations for material used in the frost protection layer, and is referred to here as *fine graded FPL*. The fines content for this material was 12%, and it was expected to be frost susceptible. However, the large fines content would retain more water than the two other frost protection layers. This would in turn increase the amount of latent heat and provide a better thermal barrier. The investigation of this material is being carried out in associated study under the Frost Project.

Ro3 was constructed using a coarse yet well graded crushed rock material with a particle size of 0/120mm, but it had not been sieved below 5 mm (see Figure 14). However, extending the gradation curve to the fine part would most likely give a fines content that is not frost susceptible. This material was designed as a reference and is referred to here as *typical FPL*. It was assumed that based on the requirements for a frost protection layer, a material like this would be close to the optimal choice with no risk of air convection (compared to *open grade FPL*) or frost susceptibility (compared to *fine graded FPL*). In addition, the coarse material does not require extensive crushing.

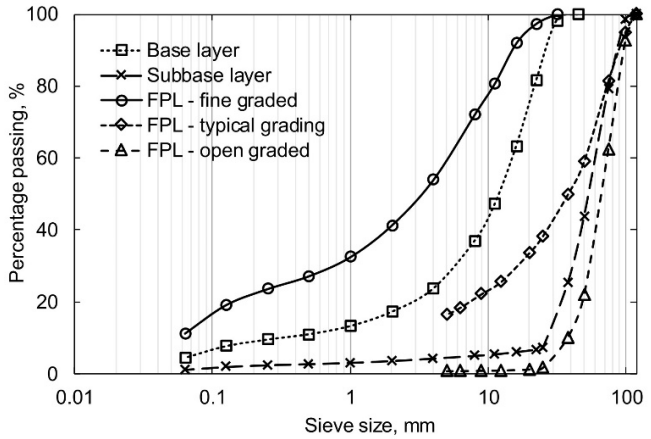

Figure 14. Material grain size distribution for road sections Ro1–Ro3

3.2.5 Materials used for road sections Ro4-Ro6

In Ro4– Ro6 the same materials were used for both the base and the subbase layers. The material used for the LFPL was the same *typical FPL* material used in Ro3. The variation in Ro4–R6 was in the material used for the lightweight aggregate layer. Two different gradations of expanded clay (Leca) and one foam glass material (Glasopor) were used for these sections. Figure 15a and 15b show the construction of the lightweight aggregate layers and the sizes of the expanded clay and foam glass particles. Figure 16 gives the grain size distribution for all three lightweight materials. Expanded clay is produced by heating clay up to around 1200°C in a rotary kiln, while foam glass material is produced by sintering crushed glass powder.

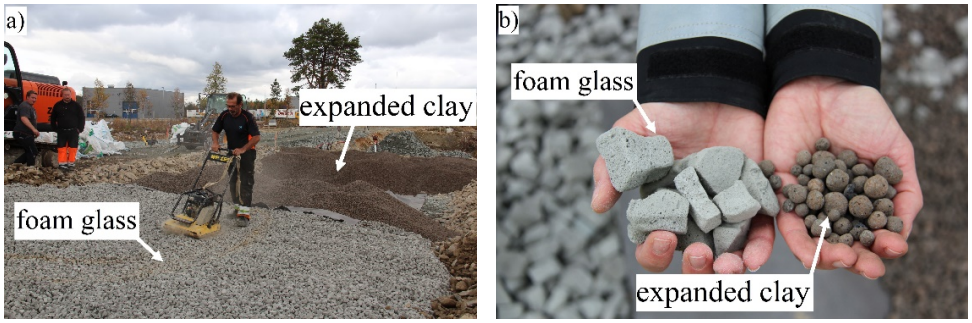

Figure 15. Lightweight aggregates: a) during construction process; b) particle comparison

An expanded clay with a particle gradation of 10/20 mm was used for Ro4. This material had a modified particle distribution compared to material directly from the production line. Road section Ro5 was constructed using expanded clay with a particle size of 0/32 mm. This material is the primary product of expanded clay. It was assumed that the performance of these two gradations of expanded clay would ultimately give very similar results. However, the 10/20 mm material had a higher d_{10} value, which theoretically means that air convection would be initiated at a lower temperature gradient due to its greater permeability.

Ro6 was constructed using a layer of foam glass material. The particle size as declared by the producer was 10/60 mm. However, the material contained negligible fractions of material below 20 mm and above 50 mm. Foam glass material is of particular interest in natural air convection due to its high d_{10} value compared to expanded clay. The d_{10} value for foam glass is fairly close to that of crushed rock. In addition, the material has a substantially low thermal conductivity. The combination of these factors could promote natural air convection at fairly low temperature gradients. This would have a negative effect on frost insulating performance.

For a better insight into the performance of these three lightweight materials, they were all tested using the large-scale test setup. The results from the 0/32 mm expanded clay and foam glass materials are included in Paper III, and those from the 10/20 mm expanded clay are presented here in the results section.

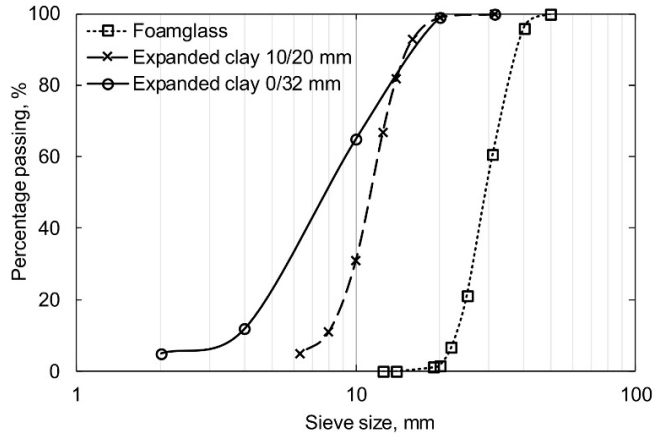

Figure 16. Grain size distribution of lightweight aggregates used in road sections Ro4–Ro6

3.2.6 Materials used for railway sections Rw1–Rw4

The primary objective with the railway sections was to use two different material gradations and two different mineralogies in the subballast layer, adding up to four different variations of subballast material. This makes it possible to separate the evaluations of the effects of the gradation and of the mineralogy. However, the actual material gradations were not consistent with the designed ones and the final structure had four different material gradations, making evaluation of the effects more complex. The quartzite material (see Hanestad mineralogy in Table 1) had a particle size of 0/120 (Rw1) and 20/120 (Rw2). The gabbro material (see Vassfjell mineralogy in Table 1) had a material gradation of 0/250 mm (Rw3) and 20/250 mm (Rw4).

All of the railway sections were built using *typical FPL* material for the frost protection layer. The ballast layer was constructed using a typical ballast material with a gradation of 32/63 mm. The variation in Rw1–Rw4 was in the gradation and the mineralogical composition of the material. Figure 17 shows the different materials used for the railway sections: a) a common frost protection layer for all sections with 0/120 mm subballast material; b) a comparison of the two mineralogical compositions of the subballast materials used. The grain size distribution of all the crushed rock materials (except FPL) is given in Figure 18.

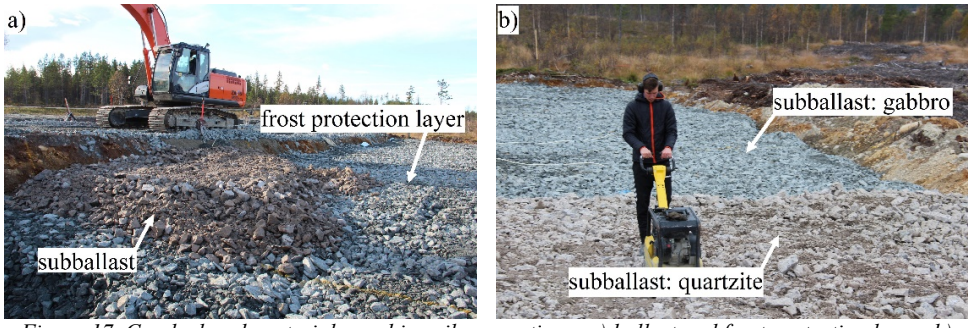

Figure 17. Crushed rock materials used in railway sections: a) ballast and frost protection layer; b) comparison between gabbro and quartzite material used for subballast layer

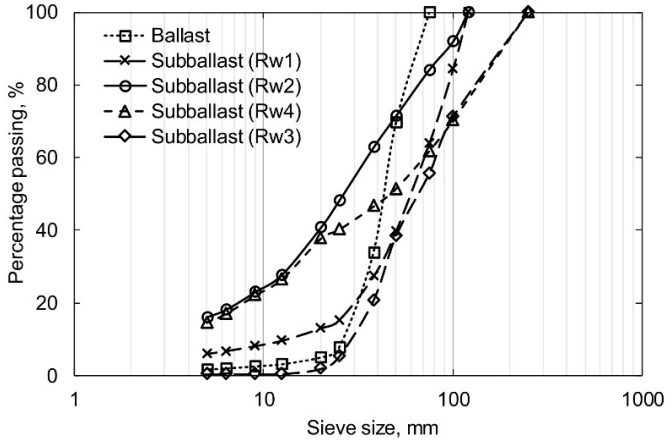

Figure 18. Material grain size distribution in railway sections Rw1–Rw4

3.2.7 Summary of field test site

The description of field test site in section 3.2 shows the extent of the Frost Project's research objectives. The test site provided potential for numerous investigations of material performance in terms of thermal properties.

In the first three road sections (Ro1–Ro3) the grain size distribution of the materials used for the frost protection layer (*open graded*, *fine graded* and *typical gradation*) varies. Each of the materials represents a different case based on the regulations on material size in the frost protection layer. The *open graded* material is at the upper limit and is potentially susceptible to natural air convection at small temperature gradients. The *fine graded* material is at the

lower limit, being potentially frost susceptible due to its high fines content. The *typical grading* serves as a reference section with material of potentially optimal particle size distribution in terms of its thermal properties. Ro4–Ro6 allow the investigation of the thermal performance of lightweight aggregates (expanded clay and foam glass). Railway sections were built using different subballast materials. The individual sections made it possible to observe the effects of different material gradations and mineralogical (gabbro and quartzite) composition.

The field test site has provided a vast amount of data. However, only Paper VII is dedicated to the investigation and modelling of the site. In particular, it discusses only road sections Ro1 and Ro6. However, this allows greater focus on the subject of possible natural air convection in road construction materials and a more thorough discussion of three particular materials: subbase (Ro1 and Ro6), *open graded FPL* (Ro1) and foam glass material (Ro6). These three materials were also tested under laboratory conditions. The combination of laboratory, field and numerical investigations provides a good insight into their performance and thermal properties.

3.3 Modelling

This section describes the numerical models developed and the simulations carried out in this study. Two numerical models were developed. The first describes the large-scale heat transfer cell (section 3.3.1) and is discussed in Paper IV. Its primary purpose was to develop a test-setup-specific Nu-Ra relationship that would account for any deviations from the perfectly square enclosure on which Schubert and Straus (1979) analytical Nu-Ra relationship is based. Having a test-setup-specific Nu-Ra relationship made it possible to re-establish the intrinsic permeability values with higher precision. The second model represents the field test site (section 3.3.2, and discussed in more detail in Paper VII). Only two sections were modelled at this stage, namely Ro1 and Ro6. The primary focus here was on sections with open graded crushed rock and foam glass materials. The model allowed comparison with the field observations regarding the occurrence of natural air convection during the winter.

3.3.1 Modelling of heat transfer cell

The numerical model of the large-scale test setup was developed using Comsol Multiphysics finite element software. The model incorporates coupled heat and mass transfer mechanisms in steady state conditions. Both a two-dimensional (2D) and a three-dimensional (3D) model were developed to evaluate any corner effects.

The numerical problem solved in this model is the porous medium analog of the Rayleigh-Bérnard problem in fluids (Nield & Bejan, 2013). This was first studied by Horton and Rogers (1945) and later, independently, by Lapwood (1948), and hence the problem is defined as the Horton-Rogers-Lapwood problem dealing with an infinite horizontal porous layer heated from below. The numerical problem can be also applied to a finite sized porous medium heated from below. The conservation equations for mass, momentum and energy for a steady state thermal energy transfer and fluid flow consisting of a porous matrix saturated with a single mobile fluid (air) are as follows (Nield & Bejan, 2013):

mass:

[26] $\nabla \cdot u = 0$

momentum:

[27] $u = -\frac{K}{\mu}(\nabla P - \rho_f g)$

energy:

[28] $(\rho c_p) u \cdot \nabla T = k_m \nabla^2 T$

where ∇ is the differential operator, u is the pore air velocity ($m \cdot s^{-1}$), K is intrinsic permeability (m^2), μ is the dynamic viscosity of the pore air (Pa·s), P is pressure (Pa), ρ_f is air density ($kg \cdot m^{-3}$), g is gravitational acceleration ($m \cdot s^{-2}$), ρ, cp and ke are the density ($kg \cdot m^{-3}$), specific heat capacity ($J \cdot kg^{-1} \cdot K^{-1}$) and effective thermal conductivity ($W \cdot m^{-1} \cdot K^{-1}$) of the porous medium respectively, and T is the temperature (K).

Numerous simplifications and assumptions were made for the model that may deviate to some extent from an actual laboratory experiment or material response under environmental conditions. First, it is assumed that the porous medium is homogenous and isotropic, that Darcy's law is valid (only linear fluid flow) and that the Oberbeck-Boussinesq approximation is applicable. Second, it is assumed that the fluid (air) is incompressible and that the variations in density are merely due to temperature variation. With these assumptions, the Oberbeck-Boussinesq approximation is used as follows:

[29] $\rho_f = \rho_0[1 - \beta(T - T_0)]$

where ρ_0 is a reference density ($kg \cdot m^{-3}$), T_0 is a reference temperature (K) and β is thermal expansion (K^{-1}). In essence Eq.29 introduces the density variation along the temperature gradient. This will in turn create fluid flow if conditions allow.

Boundary conditions

Two independent boundary conditions are used for the model. First, an inner boundary condition is directly applied to the sample representing the top and bottom heat exchange plates used in laboratory conditions. The inner boundary conditions are temperature controlled and are set accordingly above and below the reference temperature to impose a downward or upward heat flow:

[30] $T_{bottom} = T_{ref} \pm \Delta T/2$

[31] $T_{top} = T_{ref} \pm \Delta T/2$

where T_{bottom} is the temperature set at the bottom of the sample, T_{top} is the temperature at the top of the sample, Tref is the reference temperature and ΔT is the difference between the top and the bottom temperatures. The reference temperature is set equal to 22.5°C, the average room temperature during the laboratory tests.

The second boundary condition is a temperature controlled boundary imposed on the outer walls of the heat transfer cell. The temperature is set equal to T_{ref} representing the

laboratory conditions. In this way the average sample temperature is close to T_{ref} minimizing any heat loss or input through the side wall.

Air convection initiation

Under laboratory conditions the direction of the air convection was initiated with a line heat source. A similar approach was taken in the numerical model to ensure a unicellular convection cell. However a different approach was used for the 2D and 3D models. In the 2D model, to initiate convection in a certain direction a temperature gradient was applied over the bottom inner boundary. After this the temperature was returned to a uniform temperature setting in a few steps. This method was not successful for the 3D model, with any change in bottom boundary conditions resulting in convergence problems. As an alternative method of imposing air convection the gravitation angle was tilted by 30°. This is equal to tilting the whole domain and keeping the gravitational vector vertical. In this way air convection is initiated in a certain direction. Afterwards the gravitational angle was returned to vertical, maintaining the air flow in the initial direction.

3.3.2 Modelling the field test site

The domain for the test site model is that of road sections Ro1 and Ro6, as shown in Figure 11, and it was built using the same conservation equations (Eqs.26, 27 and 28) and employing the Oberbeck-Boussinesq approximation (Eq.29). However, the model was extended to include transient conditions and incorporate a phase change.

Boundary conditions

The upper boundary conditions are set equal to the field temperature measurements from the moist upper thermocouples embedded in the asphalt layer. The modelling period was set to represent the ground cooling period from October 1, 2017 to May 1, 2018.

The bottom boundary conditions were set to temperature-controlled. The depth and temperature for the bottom boundary conditions were set in an iterative process by comparing numerical results with temperature change measurements from the thermocouple located in the silt layer.

The side boundary conditions were set to zero flux. This could have a considerable effect on temperature distribution near the side boundaries. However, it was considered the best approach due to lack of knowledge about material properties and temperature distribution outside the road boundaries.

Phase change

The phase change is incorporated using an apparent heat capacity method. The apparent heat capacity (C_p) is as follows:

[32] $$c_p = \frac{\theta\rho_{ph1}c_{p,ph1}+(1-\theta)\rho_{ph2}c_{p,ph2}}{\theta\rho_{ph1}+(1-\theta)\rho_{ph2}} + L\frac{\partial\alpha_m}{\partial T}$$

where θ is the fraction of frozen or unfrozen water (no units), $c_{p,ph1}$ and $c_{p,ph2}$ are specific heat ($J\cdot kg^{-1}\cdot K^{-1}$) in phases 1 and 2 (frozen and unfrozen) respectively, ρ_{ph1} and ρ_{ph2} are density

($kg \cdot m^{-3}$) in phases 1 and 2 respectively, L is the latent heat in transitions between the two phases ($J \cdot kg^{-1}$), T is temperature (K) and α_m is calculated as follows:

[33] $$\alpha_m = \frac{(1-\theta)\rho_{ph2} - \theta\rho_{ph1}}{2(\theta\rho_{ph1} + (1-\theta)\rho_{ph2})}$$

Thermal conductivity for the phase change interval is expressed as:

[34] $$k = \theta k_{ph1} + (1-\theta)k_{ph2}$$

where k_{ph1} and k_{ph2} are the thermal conductivity ($W \cdot m^{-1} \cdot K^{-1}$) of the material in phases 1 and 2 respectively.

The θ changes from 0 to 1 and is incorporated with a smooth transition function over the phase transition period of ΔT. The phase transition for the road structural layers occurs within a very narrow temperature range and hence the transition period was set to the low value of 0.1 K. The silt layer below the structural layers will also have a proportion of unfrozen water in subzero temperatures. However, the unfrozen water content in the silt layer was not determined and hence the actual freezing curve was not available. Consequently it was decided to set the transition period also to 0.1 K. This could result in increased depth of frost penetration due an overestimation of thermal conductivity at a given temperature. However, given that the focus is on the structural layers above, this inaccuracy was considered insignificant.

4 Results and discussion

This chapter presents the main results of and discussions on the laboratory experiments, numerical modelling and field test site analysis. Section 4.1 first gives the results of the study of the thermal conductivity of solid particles (Paper V). Next the chapter presents the experimental results together with model predictions on the thermal conductivity of crushed rock materials (Paper VI). Section 4.2 provides the results of and discussion on natural air convection in the large-scale experiments. This section is split into four subsections. The first briefly introduces earlier experimental test setups on which the current study relies (Paper I). The second subsection explains the validation process of the experimental setup for conduction and convection conditions (Paper II). The third subsection provides the experimental results and establishes the intrinsic permeability of coarse construction materials (Paper III). The fourth subsection presents the numerical model of the experimental test setup to re-establish intrinsic permeability, with test-setup-specific Nu-Ra relationship (Paper IV). Finally, section 4.3 presents the field analysis of temperature distribution in road structures and further analysis of possible natural air convection based on numeric modelling (Paper VII).

4.1 Small-scale experiments

4.1.1 Thermal conductivity of solid particles

A minor part of the small-scale experiments was dedicated to different methods of measuring or estimating the thermal conductivity of solid particles (k_s). Four methods were investigated, including direct and indirect measurements of k_s and estimating it based on mineralogical composition. The main objective of this investigation was to compare the different methods and to get input parameters for the thermal conductivity model validation described in Paper VI.

The final results on k_s measurements and estimation are given in Figure 19. The next paragraphs briefly introduce each of the methods and the main observations about and obstacles affecting the accuracy of each one.

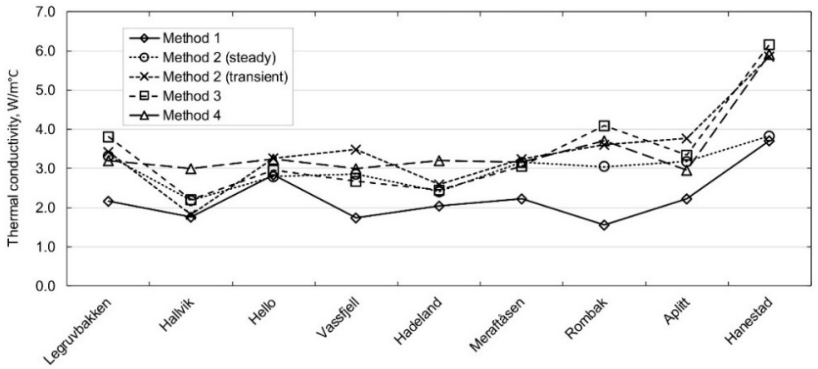

Figure 19. Comparison of different methods for measuring or estimating thermal conductivity for solid particles (k_s)

Method 1

Method 1 was the only method used for the direct measurement of k_s values and was carried out on rock core samples (see Figure 5b) obtained from the same quarries as the corresponding crushed rock materials. Measurement of the samples was carried out via a small-scale experimental setup using both heat flux sensors. The measurements given in Figure 19 are the average of the two small-scale experimental setups.

The measurements of the rock core samples systematically provided the lowest values of k_s. Given that the other methods yielded higher results, it was assumed that the measurements of the rock core samples might have been underestimated. Although this is a direct measurement of k_s, a few difficulties were encountered using this method. First, there was thermal resistance at the interface between the rock core sample and the heat flux sensor. This was minimized using thermal paste; however, it still probably had a certain effect on the accuracy of the measurements. Second, the temperature sensors were embedded in the heat flux sensors and so the temperature gradient measurements were not taken directly from within the sample. This issue could be solved by drilling and embedding the sensors directly in the sample. Third, the rock core samples may have had minor fractions; in fact in some the fractions were clearly visible. These would essentially result in lower measurements.

Method 2 (steady state)

Method 2 was carried out by measuring saturated samples with a particle size of 1–2 mm and using Eq.8 to back-calculate the k_s value. The measurements were made using only borosilicate glass discs, as the heat flux plates might have been compromised if immersed in water.

Although all of the methods arrived at quite different results, it was believed that this method is the most accurate in this study. Comparing the conditions of this experiment to those using the core samples eliminates two issues: first, as the heat flux sensor was in direct contact with the water, no contact resistance was expected to influence the results. However, the bottom part of the sample was sealed with a thin aluminum plate. Thermal paste was used at the bottom between the sample and the heat flux sensor, and hence there may have been some remaining thermal resistance issues in the bottom part. Second, as the tested material was rather fine there were no issues with fractions, as there were with the core samples.

Method 2 (transient state)

Method 2 was also carried out performing transient state measurements using a TP08 needle probe from Hekseflux. The measurements were carried out in the same 1-2 mm fraction material with saturated samples, using Eq.8 to back-calculate the k_s values.

This method provided very fast k_s measurement and generally agreed with those obtained using the steady-state method. The main challenge with this method is determination of the time period over which to derive thermal conductivity measurements. As the method is transient, small changes in the time period led to large variations in the final result. Hence the method can give good results, but can be sensitive due to the interpretation of the results.

Method 3

Method 3 was based on the geometric mean method given by Eq.10. While the method has no physical basis it has been proven to give good estimates of k_s by numerous studies (Birch & Clark, 1940; Horai, 1971; Woodside & Messmer, 1961).

The results, presented in Figure 19, show that the method generally agrees well with the results from method 2 (steady state), with a few exceptions for materials with a higher quartz content. The fact that methods 2 and 3 lead to rather similar values is another argument that the measurements of the core samples were underestimated. Method 3, however, relies on precise measurement of mineralogical composition, which can be difficult with some classes of minerals.

Method 4

Method 4 is a simplified version of the geometric mean proposed by Johansen (1975). It is based on the quartz content and assumes a constant thermal conductivity for other minerals. If the quartz content is equal to or below 20%, the thermal conductivity of the rest of the minerals is assumed to be 3 W/m°C. If the quartz content is higher than 20% the thermal conductivity of the rest of the minerals is assumed to be only 2 W/m°C.

Figure 19 shows that method 4 provides much less k_s variation than the other methods, tending to give k_s values of around 3 W/m°C for most of the materials tested. This method may only work precisely with materials with a very high quartz content in which k_s is governed by the quartz content rather than other minerals. Method 4 is particularly inaccurate for quartz content around 20% given that the transition in this range is not smooth.

Based on the different methods covered in this study, measurements from method 2 (steady state) were selected as input parameters for the thermal conductivity model discussed in the next section. Alternatively, if no measurements (direct or indirect) are available, method 3 can be used to estimate k_s values.

4.1.2 Thermal conductivity of crushed rock materials

This part of the research was carried out primarily to validate and adapt an existing thermal conductivity model to use as a tool to determine the thermal conductivity of crushed rock materials in field conditions. For this, a large number of laboratory experiments were carried out.

Nine materials from different quarries across Norway, each with different mineralogical composition, were selected (see Table 1). In total, 42 samples were prepared and tested under 3 to 5 different moisture content conditions. This accounted for 164 tests in the unfrozen state and the same number in the frozen state. Thermal conductivity was measured using the experimental setup presented in section 3.1.1. A complete list of the sample characteristics is given in Paper VI.

Figure 20 shows the typical temperature evolution of a test sample using borosilicate glass discs (GD) as heat flux sensors. The sample is first subjected to a temperature above zero, applying approximately 7°C at the top and 3°C at the bottom of the sample. The measurements from the steady state conditions are used to calculate unfrozen thermal conductivity. Subsequently the temperature settings are reduced to below zero. Temperatures

of approximately -3°C and -7°C are applied at the top and the bottom of a sample respectively. The measurements from the steady state conditions are used to calculate thermal conductivity in the frozen state. In samples with higher moisture content a clear phase change period can be observed, as shown in Figure 20.

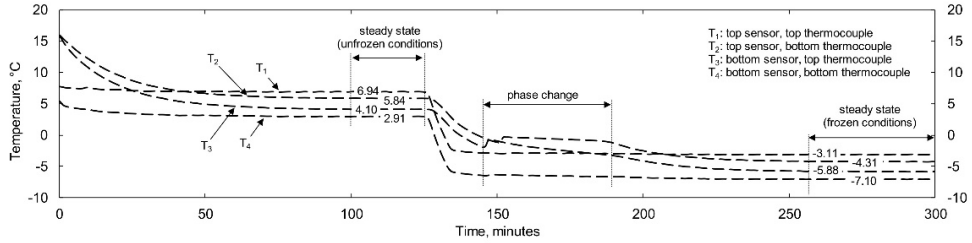

Figure 20. A typical temperature evolution in a sample using borosilicate discs as heat flux sensors

Figure 21 shows the temperature distribution in the three-layer system based on the measurements presented in Figure 20: a) temperature profile and calculated heat flux values under frozen conditions; b) sample layout; c) temperature profile and calculated heat flux values under unfrozen conditions. As shown, the heat flux measurements obtained from both heat flux sensors are very similar, validating the experimental setup and steady state conditions. The average heat flux is subsequently used to calculate the thermal conductivity in the crushed rock sample.

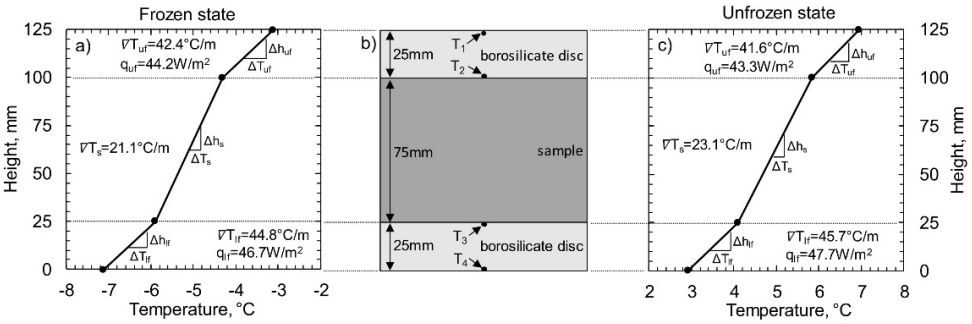

Figure 21. Representation of temperature distribution in the sample based on temperature measurements in Figure 5: a) measured temperature profile and calculated heat flux and temperature gradient under frozen conditions; b) sample layout with a specimen enclosed by borosilicate glass discs at the top and the bottom; c) measured temperature profile and calculated heat flux and temperature distribution for unfrozen conditions. Notation: Δh_{uf}, height of upper heat flux sensor; ΔT_{uf}, temperature difference in upper heat flux sensor; Δh_s, height of sample; ΔT_s, temperature difference in sample; Δh_{lf}, height of lower heat flux sensor; ΔT_{lf}, temperature difference in lower heat flux sensor.

Figure 22 shows a typical temperature and heat flux evolution in a sample tested with heat flux plates (HF) as heat flux sensors. Like the setup with the borosilicate discs, the sample is first subjected to a temperature gradient above zero. Once steady state is reached, subzero temperatures are applied to the sample. Two significant things can be observed in the measurements showed in Figure 22. First, the heat flux measurements are very sensitive to minor temperature fluctuations imposed by the heat exchange plates. However, calculating an average heat flux value for a given period of time (under steady state conditions) gives a good representation of heat flux value. Second, the temperature measurements are not as

stable as in the setup with borosilicate discs. However, the temperature difference between the upper and lower sensor stays fairly stable throughout the experiment and hence the temperature variation is due to the reference temperature in the data logger. As a result, the temperature fluctuations have no influence on the calculated temperature gradient.

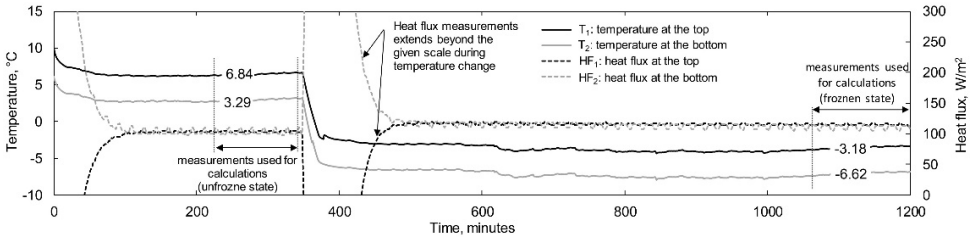

Figure 22. A typical evolution of temperature and heat flux in a sample measured using heat flux plates as measurement sensors

Figure 23 shows the temperature distribution in the sample based on the measurements shown in Figure 22: a) measured heat flux values and calculated temperature gradient under frozen conditions; b) sample layout; c) measured heat flux values and calculated temperature gradient under unfrozen conditions. As shown, the heat flux measurements provide very similar results validating the experimental setup.

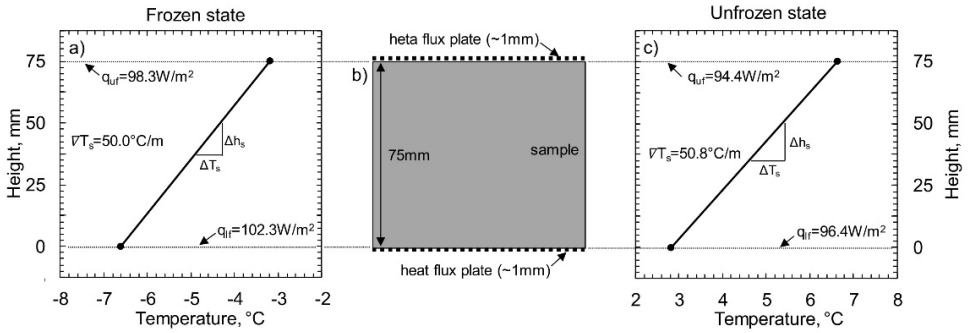

Figure 23. Representation of temperature profile in sample based on temperature measurements showed in Figure 22: a) measured temperature profile and heat flux and calculated temperature gradient in sample in frozen conditions; b) sample layout with specimen enclosed by heat flux plates at top and bottom; c) measured temperature profile and heat flux and calculated temperature gradient in sample in unfrozen conditions. Notation: Δh_s, height of sample, ΔT_s, temperature difference in sample.

The original thermal conductivity model proposed by Côté and Konrad (2005b) uses Eq.5 to estimate dry thermal conductivity values. However, it was observed that due to this equation the calculated thermal conductivity values in a low range of saturation are lower than those measured in the experiments. A comparison between the experimental results and the predicted values using the original model is given in Paper VI.

Eq.5 could be applicable to materials with relatively large porosity where the particle thermal conductivity can be negligible. However, given that the experimental samples had a low range of porosity varying between 0.14 and 0.21, Eq.6 is more appropriate for the calculation of dry thermal conductivity, given that the equation takes into account not only the porosity and particle shape factors but also particle thermal conductivity. Figure 24a and 24b compare the experimental measurements and the model predictions for the unfrozen and

frozen states respectively, showing that the model predictions agree fairly well with the experimental results. However, some adjustments could be made to the model.

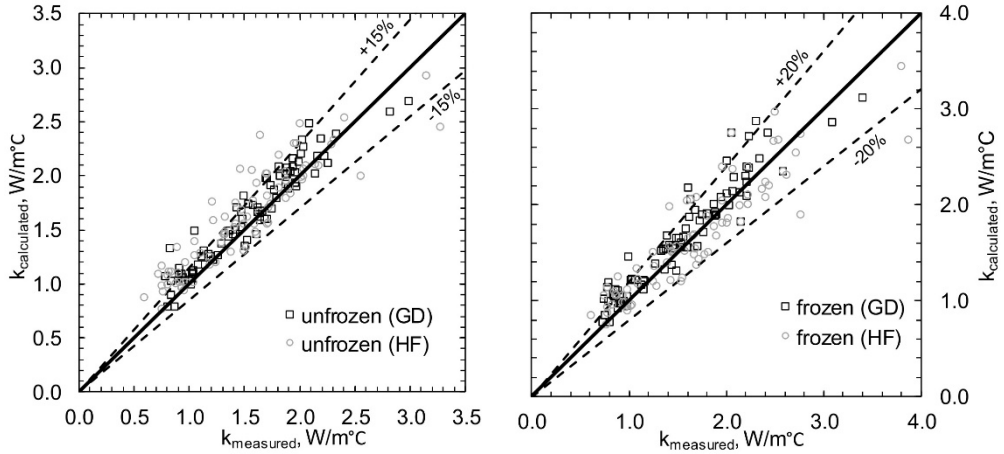

Figure 24. Comparison between experimental measurements and model predictions: a) unfrozen conditions; b) frozen conditions; Notation: GD – meausrements with glass discs, HF – measuremnets with heat flux plates

Figure 24 shows that the model predictions give slightly higher thermal conductivity values than those of the experimental results, especially in the low range of moisture content. This most likely originates from overestimated values using Eq. 6 to estimate of k_{dry}. Eq.6 through Eq.7 incorporate a structure parameter β accounting for soil type. Côté and Konrad (2009) establish a best fit β value of 0.54 for the crushed rock materials tested in their study. Given that β was established for a particular set of data, the value could change slightly depending on particle angularity.

Furthermore, the model prediction incorporates another parameter κ in Eq.4 accounting for the structure. The κ values for unfrozen and frozen conditions were established for a particular dataset. The κ parameter could be slightly adjusted given that the material used in this study is different from that used by Côté and Konrad (2005b) in the original model development. Substituting $k_{sat(u)}$, k_{dry} and k_{nu} in Eq.11 with the corresponding Eq.8, 6 and 4 yield:

$$[35] \quad k_u = \underbrace{\left(k_s^{1-n} k_w^{n} - \frac{\left(0.29\left(15\frac{k_f}{k_s}\right)^{\beta} k_s - k_f\right)(1-n) + k_f}{1+\left(0.29\left(15\frac{k_f}{k_s}\right)^{\beta} - 1\right)(1-n)} \right)}_{k_{sat}} \underbrace{\frac{\kappa S_r}{1+(\kappa-1)S_r}}_{k_r} + \underbrace{\frac{\left(0.29\left(15\frac{k_f}{k_s}\right)^{\beta} k_s - k_f\right)(1-n) + k_f}{1+\left(0.29\left(15\frac{k_f}{k_s}\right)^{\beta} - 1\right)(1-n)}}_{k_{dry}}$$

Eq.35 is the full model equation for unfrozen conditions incorporating the two structure parameters β and κ. A similar equation can be made for frozen conditions by substituting the k_{sat} part in Eq.35 with that of Eq.9 and using the corresponding κ value. Eq.35 can be used to best fit the β and κ parameters. However, the two parameters could be adjusted in several ways: separately from each other, or simultaneously on a single dataset (one sample), on a frozen or an unfrozen dataset, or on the whole dataset together. Paper VI presents more details and results regarding the different ways of adjusting the β and κ parameters. The most

reasonable way to adjust the two parameters was found to be fitting them simultaneously based on the whole dataset. This can be done using β and κ as fitting parameters in Eq.35 and finding the least square difference between the model predictions and the experimental measurements. However, the β value has to be fitted based on the whole dataset, whereas two individual κ have to be fitted for the unfrozen and frozen datasets accordingly. Figure 25 shows the final results of the comparison between the model predictions and the experimental results with fitted structure parameters. The best fit of β value is 0.58. This is slightly higher than that in the original model, 0.54. This probably means that the crushed material tested in this study is less angular than that used in the study by Côté and Konrad (2005b). The best fit of κ resulted in values of 3.9 and 1.8 for unfrozen and frozen conditions respectively. The κ value for the frozen state is the same as in the original model, while that for the unfrozen state is lower than the original value of 4.7. However, the change in κ only has a minor effect on the model prediction, and can probably be attributed to the different material tested in this study.

Figure 25 shows that although the β and κ parameters are adjusted, the model predictions give higher values in the low range of water saturation than in the experimental results. This inaccuracy could be associated with problems measuring nearly dry samples. The same sample was tested and gradually dried multiple times. Although the samples were densely compacted, some particles from the bottom of the sample fell off while moving it from the testing to the drying facilities. This certainly affected the measurement of thermal conductivity for the low range of moisture content.

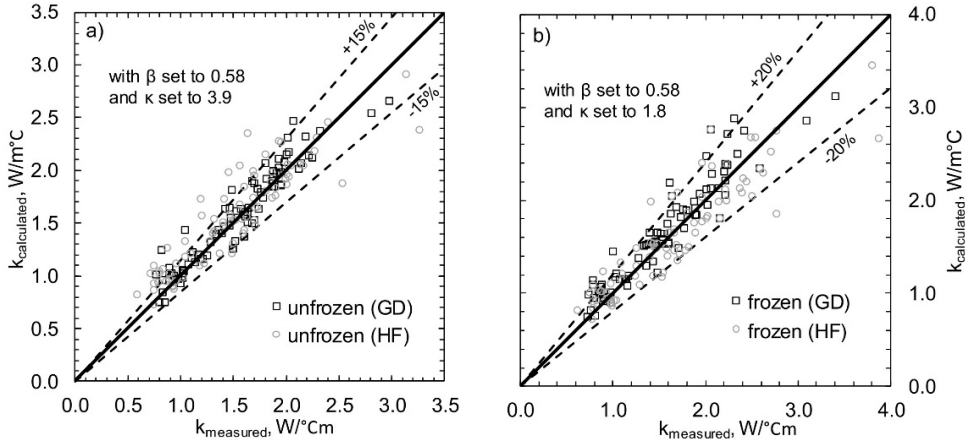

Figure 25. Comparison between experimental measurements and model predictions: a) unfrozen conditions with φ and κ parameters fitted to 0.63 and 4.3 respectively; b) frozen conditions with φ and κ parameters fitted to 0.56 and 1.7 respectively

To sum up, the thermal conductivity model proposed by Côté and Konrad (2005b) agreed relatively well with the experimental measurements in this study. However, it was observed that the model predictions tend to give slightly higher values, especially in the low range of moisture content. This is probably because the materials tested here are different to those in the model. The model incorporates two structure parameters (β and κ) which were configured based on the experimental dataset from this study. The validated and adapted

model is used further in the analysis of the field test site to calculate thermal conductivity in crushed rock materials (Paper VII).

4.2 Large-scale experiments

This section first briefly reviews the preceding large-scale experimental studies of natural air convection, which are reviewed more thoroughly in Paper I. It then presents the experiments performed using the large-scale heat transfer cell. In total eight tests were performed using the experimental test setup. The tests were performed in three stages. The first stage was dedicated to the validation of heat conduction conditions. The second stage was conducted to validate the test setup for convective heat transfer. The third stage involved the actual measurement of convective heat transfer in six different road construction materials, including three crushed rock materials with particle sizes of 20/120, 40/120 and 20/250 mm, and three lightweight aggregates typically used for insulation purposes: two samples of expanded clay with particle sizes of 0/32 and 10/20 mm, and one of foam glass material with a particle size of 10/60 mm. The results of the first two stages are reported in Paper II and the results of the third stage are presented in Paper III. The final part of section 4.2 is dedicated to a numerical model of the large-scale experimental test setup. The model made it possible to derive a test-setup-specific Nu-Ra relationship and to re-establish intrinsic permeability.

4.2.1 Review of preceding studies

The four studies, including the ongoing study, reviewed here and in more detail in Paper I, were selected on the basis that they all rely on the preceding work to some extent.

Johansen (1975) doctoral thesis focuses mostly on aspects of the thermal conductivity of soils. However, a minor part of his study is dedicated to natural air convection in coarse open graded materials. His test sample had a cross-section of 2.2x1.8 m and a thickness of 0.48 m. The experimental setup is shown in Figure 26a. Only one crushed rock sample with a particle size distribution of 20 to 80 mm was tested.

The tests on air convection were performed under different conditions. Johansen (1975) tested heat transfer characteristics for both natural and forced convection. The tests on natural air convection were conducted with permeable (open-system) and impermeable (closed-system) top surfaces. The upper boundary conditions were set by the room temperature, while the lower boundary was a temperature controlled by a heat exchange plate. The temperature was measured in seven horizontal cuts spaced 8 cm apart. The heat flux was measured using nine heat flow gauges. Johansen (1975) was, however, limited to the calculation of Ra and Nu values, as at that time the analytical solution by Schubert and Straus (1979) was not available. Unfortunately, this study provides no information on the number or size of air convection cells. Given that the sample's horizontal dimensions were much larger than the thickness, multiple air convection cells probably formed. Nevertheless, Côté et al. (2011) later successfully reanalyzed the experimental data to establish the intrinsic permeability. The results are presented later in section 4.2.2.

The experiments conducted by the NGI (1999) used a sample size with a horizontal cross-section of 1x1 m and a height of 0.75 m. The heat transfer cell is shown in Figure 26b. The temperature profile was measured only in the center section of the sample, using sensors

spaced 25 cm apart vertically. The cold boundary was temperature controlled using a fluid circulation heat exchange plate. The warm boundary was controlled with electrical heating. The electrical input was accurately monitored, allowing calculation of the heat flux. In this NGI study three different crushed rock materials with particle sizes of 0/250, 25/63 and 20/120 mm were tested. However, only the last two materials were open graded and showed air convection under relatively small temperature gradients. The NGI (1999) did not report any information on the formation of air convection cells. However, Goering et al. (2000) later developed a numerical model and compared it to the laboratory experiments, finding that in the numerical model the air convection formed as four individual air convection cells with an upward air flow in the center of the sample and a downward air flow at each of the four corners. The results of the numerical model agreed relatively well with the experimental results from NGI (1999). The latter are reanalyzed in Paper I to establish intrinsic permeability; the results are given in section 4.2.2.

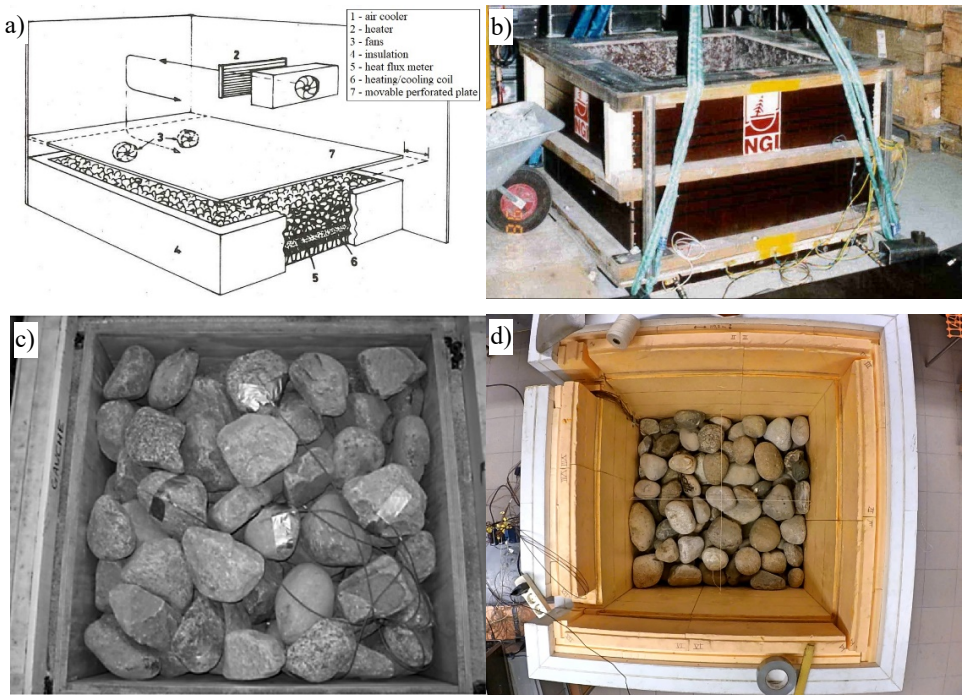

Figure 26. Experimental test setups from different studies: a) Johansen (1975); b) NGI (1999); c) Côté et al. (2011) (figure from Fillion et al. (2011)); d) Rieksts et al. (2017)

The experimental work by Côté et al. (2011) was mostly based on the earlier studies by Johansen (1975) and the NGI (1999). However, they made several improvements to their experimental setups that allowed them to use the analytical Nu-Ra relationship to establish intrinsic permeability. First, the sample size was made very close to cubical. The horizontal cross-section was 1x1m while the sample height was 0.94 m. Second, air convection was initiated with a line heat source at one of the bottom edges. This allowed the imposition of unicellular air convection in a two-dimensional pattern. Third, to be able to better characterize the air flow, four heat flux plates (0.4x0.4 m) were installed at the top of the

sample. Finally, the temperature profile was controlled in five vertical cut lines. With the improved experimental test setup, Côté et al. (2011) were easily able to characterize air convection and to use the experimental results to establish intrinsic permeability. The test material for their experiments was natural cobbles. In total four different particle gradations were tested with a range of 75 to 205 mm. An example of the test material is given in Figure 26c. The established intrinsic permeability values are given in section 4.2.2.

The final test setup, shown in Figure 26d, is the one used for this doctoral study and presented in section 3.1.2. The test setup was built based mostly on Côté et al. (2011) experience, with several improvements. First, the sample height was increased to produce a more cubical sample shape. Second, the setup was equipped with nine heat flux plates instead of four, to cover a larger top sample area and provide a more detailed characterization of the convective air flow.

Table 2 summarizes the main characteristics of the four experimental test setups. More details on the experimental conditions are given in Paper I. The established intrinsic permeability and a short discussion are given in section 4.2.2.

Table 2. Characteristics of experimental setups testing for natural air convection

	Johansen (1975)	NGI (1999)	Côté et al. (2011)	Rieksts et al. (2017)
Sample width	1.8 m	1 m	1 m	1 m
Sample depth	2.2 m	1 m	1 m	1 m
Sample height	0.48 m	0.75 m	0.94 m	0.98 m
Boundary conditions	Temperature controlled on both sides	Heat flux controlled on warm side/ temperature controlled on cold side	Temperature controlled on both sides	Temperature controlled on both sides
Heat flux measurements	Nine heat-flux gauges (size not specified)	Measurement of electrical current converted to heat flux	Four heat flux plates (each 0.4x0.4 m) covering 65% of sample surface	Nine heat flux plates (each 0.3x0.3 m) covering 90% of sample surface
Temperature measurements	Temperature sensors in layers with 22 sensors in each layer	Thermistors only in the centerline	Thermistors placed in layers with five sensors in each layer	Thermocouples placed in layers with five sensors in each layer

4.2.2 Validation of experimental test setup

The large-scale experimental program was initiated with two validation phases. The experimental results are presented in this section, and a more thorough discussion can be found in Paper II.

The first validation phase included a test with dry sand material to eliminate any other heat transfer mechanism apart from conduction. The sand was tested under a temperature gradient of 6.3 and 10.0°C/m and gave an average thermal conductivity of 0.46 W/m°C. This value was in agreement with values found in the literature, validating the experimental equipment for heat conduction conditions.

The second phase was the validation of convective heat transfer. The test material was natural cobbles and the primary objective was to establish intrinsic permeability and compare it with the results using similar materials reported by Côté et al. (2011). The test was first run under downward heat flow conditions. Figure 27 shows typical temperature and heat flux measurements when no air convection in present. As shown, the five thermocouples at each level show the same temperature measurements. Similarly, the heat flux measurements from all nine sensors provide very similar results, confirming that heat is transferred only by conduction (including radiant conductivity). Figure 28a shows the temperature profile under temperature gradients of 7.8, 14.5, and 19.9°C/m. Each line is the average of five temperature profiles measured in the sample. As shown, a linear temperature gradient is achieved, confirming conduction conditions. However, a distinct difference can be seen between the temperature gradients of the sample and of the upper sand layer in Figure 28a. The temperature gradient in the sand layer is roughly twice as high as that in the cobbles, indicating that heat transfer in cobbles is much higher. In fact the two materials have very similar pure thermal conductivity (k_c). However, the heat transfer in the cobbles is greater due to the equivalent radiant conductivity (k_r). Using Eq.14 to calculate k_r yields a value of 0.54 W/m°C. The sand, on the other hand, makes a negligible k_r contribution given that the d_{10} is very low. These observations shows the potential increase in heat transfer by radiation in coarse materials.

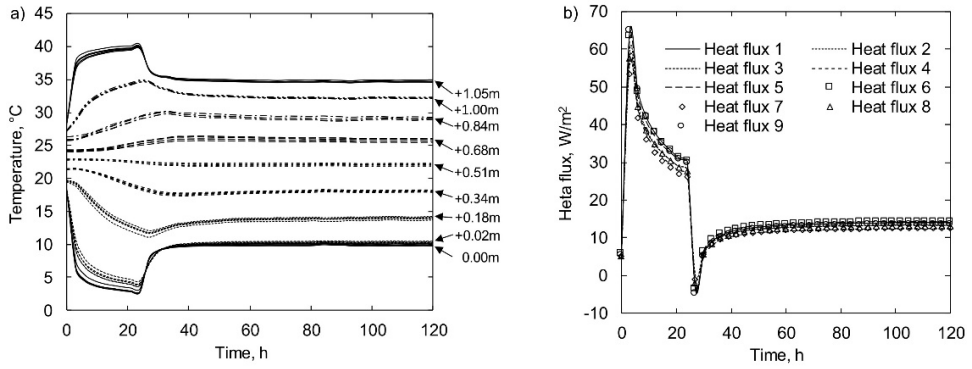

Figure 27. Typical experimental measurements under downward heat flow conditions (conduction and radiation): a) temperature measurements at different levels in the test sample; b) measurements of nine heat flux sensors at the top of the sample

After the cobbles were tested under downward heat flow conditions, the temperature gradient was reversed to allow for air convection. In addition, the line heat source was turned on to impose air convection in a two-dimensional pattern in direction from face to face. However, the line heat source turned out to be too weak to impose air convection in the desired direction in this validation experiment. As a result the air convection was initiated freely. The material was tested under three temperature gradients, 7.0, 14.1 and 17.0°C/m. Figure 28b shows typical temperature profiles in different locations in the sample under steady upward heat flow conditions (∇T=17.0 W/m°C). Figure 28b shows the measured heat flux values in units of W/m^2. The figure shows that the temperature profiles differ based on the location of the measurement. This indicates air convection in the sample. Based on the measured temperature profile and heat flux values it was concluded that air convection was

initiated in a diagonal direction. The upward air flow corresponds to the corner with the highest heat flux value, while the descending air flow is located in the corner with the lowest heat flux value. Figure 28b shows that the temperature at a given level in the sample is higher on the side with the upward air flow.

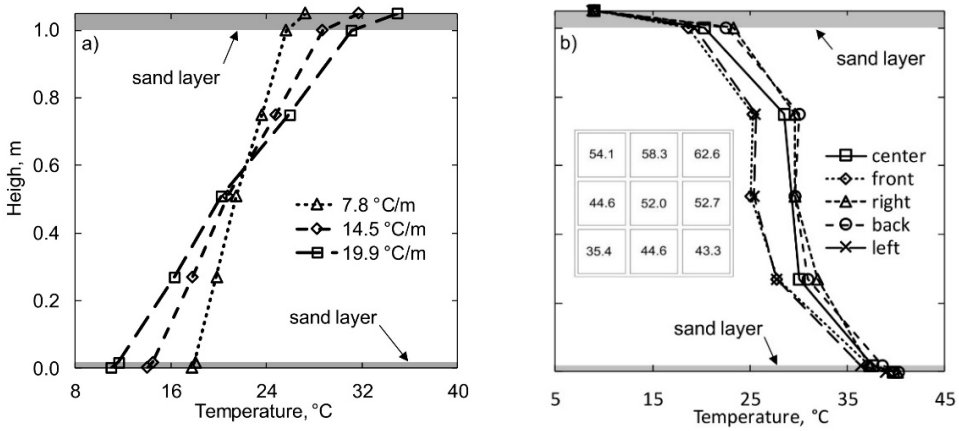

Figure 28. Experimental results for natural cobbles: a) average temperature profile under three different temperature gradients for downward heat flow conditions; b) temperature profile in different locations under upward heat flow conditions (∇T=17.0°C/m)

Figure 29 shows the experimental results for heat flux values under downward and upward conditions as a function of temperature gradient. These results make it possible to establish effective thermal conductivity from the downward heat flow results and intrinsic permeability from the upward heat flow results. First, Eq. is employed to construct a regression line using k_e as the best fit parameter (dotted line). Second, the regression line for upward heat flow conditions can be constructed with Eq.21, using K as the best fit parameter. The best fit of k_e and K for cobbles corresponds to 0.91 W/m°C and 3.38×10^{-6} m^2 respectively. Figure 29 clearly shows natural air convection increasing the overall heat transfer rate. However, the air convection is initiated only when the critical temperature gradient (∇T_c) is exceeded. For the cobbles the ∇T_c corresponds to approximately 4 °C/m.

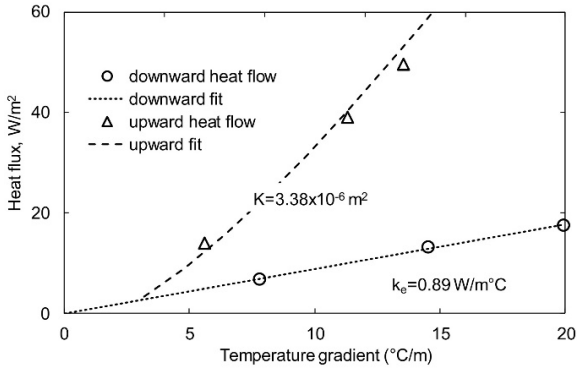

Figure 29. Comparison between experimental results under downward and upward heat flow conditions

Finally, the established K value of the validation phase with natural cobbles was compared to Côté et al. (2011) results using very similar materials. Figure 30 shows the comparison of K between theoretical models and experimentally based values as a function of α ($d_{10}^2 \cdot n^3/(1-n)^2$). It also shows the two commonly used models for the estimation of K: those of Kozeny-Carman (Eq.22) and Chapius (Eq.23). For comparison, the figure shows some experimental results with fine materials, with α in the range of $1x10^{-8}$ to $1x10^{-6}$ m^2. The figure also shows the established K value based on experimental results of Johansen (1975) (reanalyzed by Côté et al. (2011)) and those based on results from the NGI (1999) (reanalyzed by Rieksts et al. (2018)). Several points can be discussed regarding the results shown in Figure 30.

First, the validation results in terms of K values agree very well with those of Côté et al. (2011). It should once more be noted here that air convection was not initiated from face to face in a two-dimensional pattern. Instead the convection in this experiment was freely initiated in a diagonal direction. However, establishing a K value based on Eq.21 still provides a reasonable estimate.

Second, the K values established based on Johansen (1975) and the NGI (1999) experimental results agree reasonably well with the results of the Kozeny-Carman model. While in these two experiments the air convection was not restrained in a cubical enclosure, it seems that applying Schubert and Straus (1979) analytical Nu-Ra relationship still gives reasonable K values.

Third, Kozeny-Carman and Chapius's models were developed based on fine soils such as those shown in Figure 30. In the low range the two models give very similar estimates. However, when the models are extended to the range of coarse materials with α between $1x10^{-4}$ and $1x10^{-2}$ m^2, the difference is very significant. Particularly for very coarse materials, such as cobbles, the two models yield a difference of one degree of magnitude. This means that if thermal design with regard to air convection is based on one or the other model, the final result can vary significantly. Hence if possible, measurement of the intrinsic permeability of coarse materials should be conducted. A more detailed discussion comparing the experimental and the model results is given in section 4.2.3.

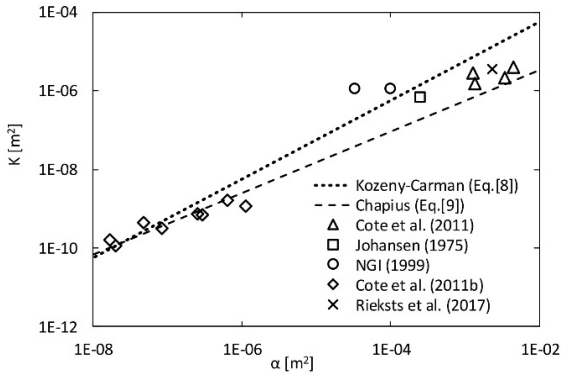

Figure 30. Measured and predicted K-α relationships

4.2.3 Experimental results on road and railway construction materials

This section presents the experimental program carried out on road and railway construction materials. The primary objective of these experiments was to establish the intrinsic permeability of coarse materials in order to be able to further analyze possible air convection under field conditions. Six different materials were tested for their air convection characteristics: crushed rock with three different gradations (20/120, 40/120 and 20/250 mm), two expanded clay materials (10/20 and 0/32 mm), and foam glass material (10/60 mm). This section presents a short discussion on the main experimental results; a longer discussion is presented in Paper III. The experiments on expanded clay material with particle size of 10/20 mm were done later, and the results are only presented here.

Downward heat flow conditions

All the materials were first tested under downward heat flow conditions. Figure 31 shows some typical temperature profiles from the experimental results. Each line represents the average temperature profile measured in the sample. As shown in Figure 31b, some deviations from the linear temperature gradient are observed. However, these can be attributed to small inaccuracies in the placement of the thermocouples.

Table 3 presents a summary of all the experimental heat flux and temperature gradient measurements for downward heat flow conditions. Two measurements are provided for expanded clay material in upward heat flow conditions below the ∇T_c. Each material was tested under two to four different temperature gradients. Most of the materials were tested for ∇T up to 30°C/m. However, the expanded clay 10/20 mm material was subjected to extremely high ∇T up to 73°C/m. The primary aim with such unrealistic ∇T was to see whether any major heat loss could be observed. It was observed that the heat flux sensors located in the corners yielded the highest measurements, while those located in the center gave the smallest values. The temperature did not show any noticeable deviation from a linear temperature profile, even at very high ∇T. However, the experiments with lightweight aggregates raised questions regarding the limiting conditions of heat transfer experiments for materials with very low thermal conductivity. This is discussed further in the next paragraph.

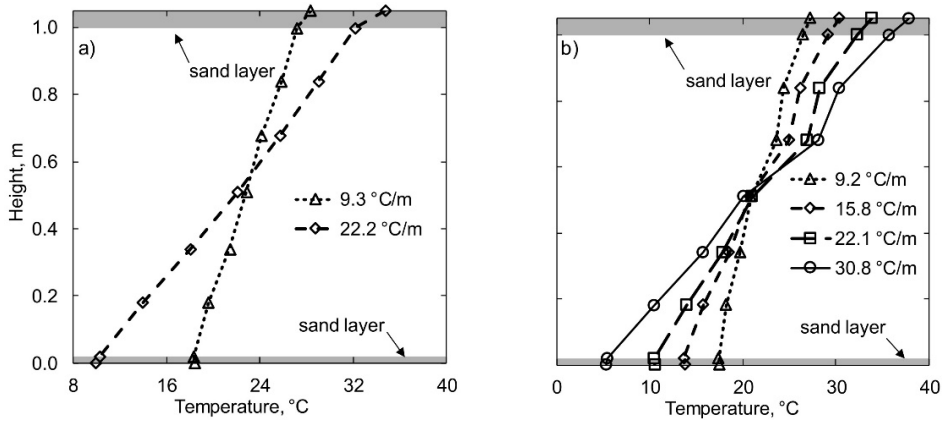

Figure 31. Typical experimental results for temperature profile under downward heat flow conditions: a) crushed rock material 40/120 mm; b) foam glass material

Table 3. Summary of experimental measurements for downward heat flow conditions

Material	Heat flux, W/m2	Temperature gradient,°C/m	Effective thermal conductivity, W/m°C
Crushed rock 20/120 mm	5.9	11.0	0.54
	9.1	17.3	
	13.5	25.1	
Crushed rock 40/120 mm	5.3	19.3	0.59
	13.4	22.2	
Crushed rock 20/250 mm	4.6	6.1	0.72
	15.4	22.3	
Expanded clay 0/32 mm	3.4	10.1	0.30
	5.7	17.6	
	9.7	32.3	
	3.0*	12.3*	
Expanded clay 10/20 mm	2.9	11.6	0.24
	5.0	21.3	
	12.4	51.6	
	18.3	73.0	
	2.4*	8.4*	
Foam glass	3.6	9.2	0.34
	5.2	15.8	
	7.2	22.1	
	9.5	30.8	

*Results of upward heat flow conditions below the critical ∇T

Figure 32 shows a compiled plot with experimentally-measured heat flux value as a function of ∇T. The final effective thermal conductivity value was derived by establishing a regression line using k_e as the best-fit parameter in Eq.. As expected, the crushed rock materials have much higher k_e values than the insulation materials, ranging between 0.54 and 0.72 W/m°C. The lightweight materials, however, showed much higher k_e than that stated by the producer of the material. For instance, dry expanded clay and foam glass materials should have a thermal conductivity value of approximately 0.10 W/m°C. The values measured in these tests were more than twice this. It was speculated that the primary reasons for this could be the limiting conditions of heat transfer experiments in tests with insulation material. When lightweight materials are tested, the thermal resistance between the upper and lower boundaries is very close to the thermal resistance through the side walls. Hence the sample could potentially have significant heat loss or heat input, resulting in overestimated values.

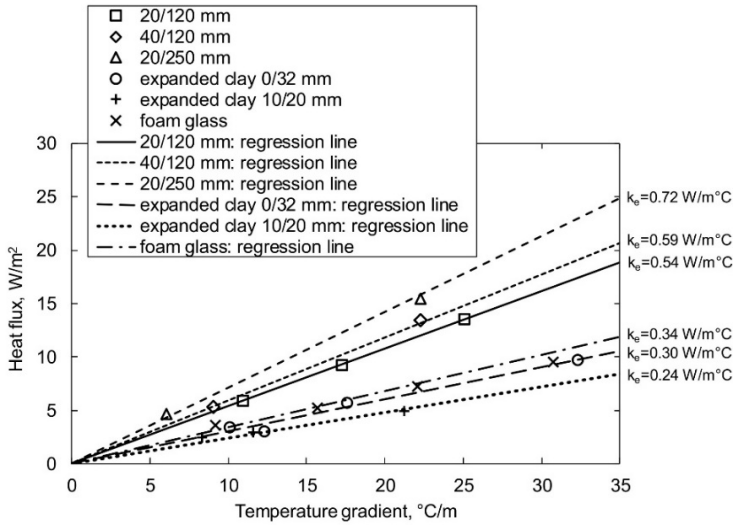

Figure 32. Experimental q-∇T relationships for downward heat flow conditions together with regression lines based on Eq.. The slope of the line indicates the effective thermal conductivity given on the right side of the figure

Upward heat flow conditions

After the materials were tested for k_e, the ∇T was reversed to impose convective heat transfer. Figure 33a shows a typical experimental result for 40/120 mm crushed rock material. For tests with construction materials a more powerful line heat source was used to initiate air convection in a direction from face to face. The method worked successfully for crushed rock materials. As shown in Figure 33a, based on the temperature profiles and heat flux measurements, air convection has a two-dimensional pattern. The highest heat flux measurements and highest temperature for a given level is on the right-hand side of the sample. This corresponds to the side of the convection cell with an upward air flow. The lowest heat flux values and lowest temperatures can be observed on the left-hand side of the box, where colder air is descending.

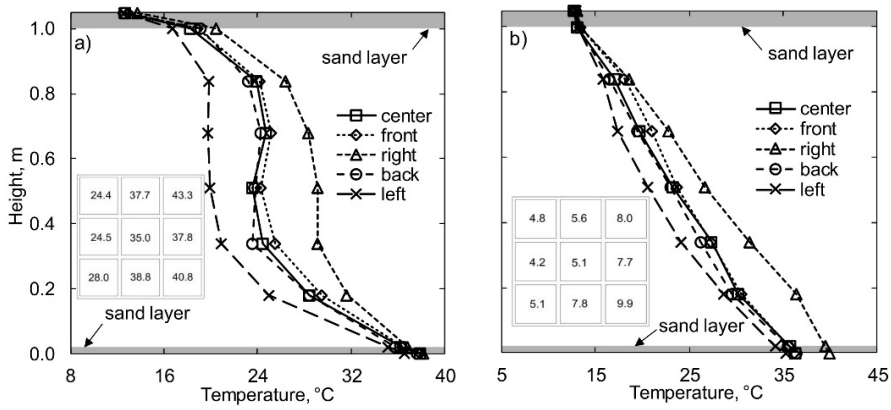

Figure 33. Some experimnetal results from upward heat flow conditions: a) 40/120 crushed rock material under ∇T of 10.9°C/m; b) 0/32 mm expanded clay material under a temperature gradient of 23.4°C/m

The experiments with 10/20 mm expanded clay and foam glass material showed some instability in the shape and number of convection cells. Although the air convection in these materials was initiated in a two-dimensional pattern, the air convection cell had a tendency to change the direction. In addition, for some tests the air convection cell reshaped into two or even four cells. However, it was observed that the average heat flux value used for the subsequent calculations is independent of the air convection instability and hence could be still used for the establishment of intrinsic permeability.

The experiments with 0/32 mm expanded clay material did not show air convection under the standard test procedure. After the line heat source was turned off, the temperature profile returned to linear. Subsequently it was decided to use the line heat source throughout the whole experiment. A typical temperature distribution is shown in Figure 33b. Although the line heat source induced different temperature profiles in the sample, these remained rather linear, confirming conduction-only conditions. Hence the value of intrinsic permeability could not be calculated for the 0/32 mm expanded clay material.

Table 4 summarizes the experimental measurements for all construction materials under upward heat flow conditions and the established values of intrinsic permeability based on the experimental results.

Table 4. Summary of experimental measurements for upward heat flow conditions

Material	∇T,°C/m	$\uparrow q$, W/m^2	T_{top},°C	T_{bottom},°C	T_{avg},°C	K (x10^{-6}), m^2
Crushed rock 20/120 mm	10.88	13.46	18.83	29.49	24.16	1.47
	16.44	20.07	17.15	33.26	25.21	
	21.29	36.44	16.06	36.92	26.49	
Crushed rock 40/120 mm	9.00	14.01	20.47	29.29	24.88	2.22
	17.75	34.48	18.71	36.10	27.41	
Crushed rock 20/250 mm	9.40	5.73	19.62	28.83	24.23	1.09
	15.21	16.91	17.77	32.67	25.22	
	19.94	29.75	17.44	36.98	27.21	
Foam glass 10/60 mm	9.4	3.57	19.48	28.69	24.09	0.86
	10.71	5.19	18.5	29	23.75	
	14.81	7.16	14.01	28.53	21.27	
	20.64	21.83	7.96	28.18	18.07	
Expanded clay 10/20 mm	19.04	5.06	12.38	31.04	21.71	0.17
	28.16	9.71	8.15	35.75	21.95	
	33.91	12.60	5.74	38.97	22.36	
Expanded clay 0/32 mm	15.68	4.62	17	32.37	24.69	-
	23.36	6.47	13.18	36.07	24.63	
	31.04	8.49	9.57	39.99	24.78	

Figure 34 compares the experimental results of upward and downward heat flow conditions as follows: a) 20/120 mm crushed rock; b) 40/120 mm crushed rock; c) 20/250 mm crushed rock; d) foam glass; e) 10/20 mm expanded clay material. The intrinsic permeability of each material was established by regression, using K as the fitting parameter in Eq.21. As expected, the crushed rock material was more permeable than the two insulation materials. The K values for the 20/120, 40/120 and 20/250 mm materials are 1.47, 2.22 and 1.09x10^{-6} m^2 respectively. For the 10/20 mm expanded clay and the foam glass material, the established K values are 0.86 and 0.17x10^{-6} m^2 respectively.

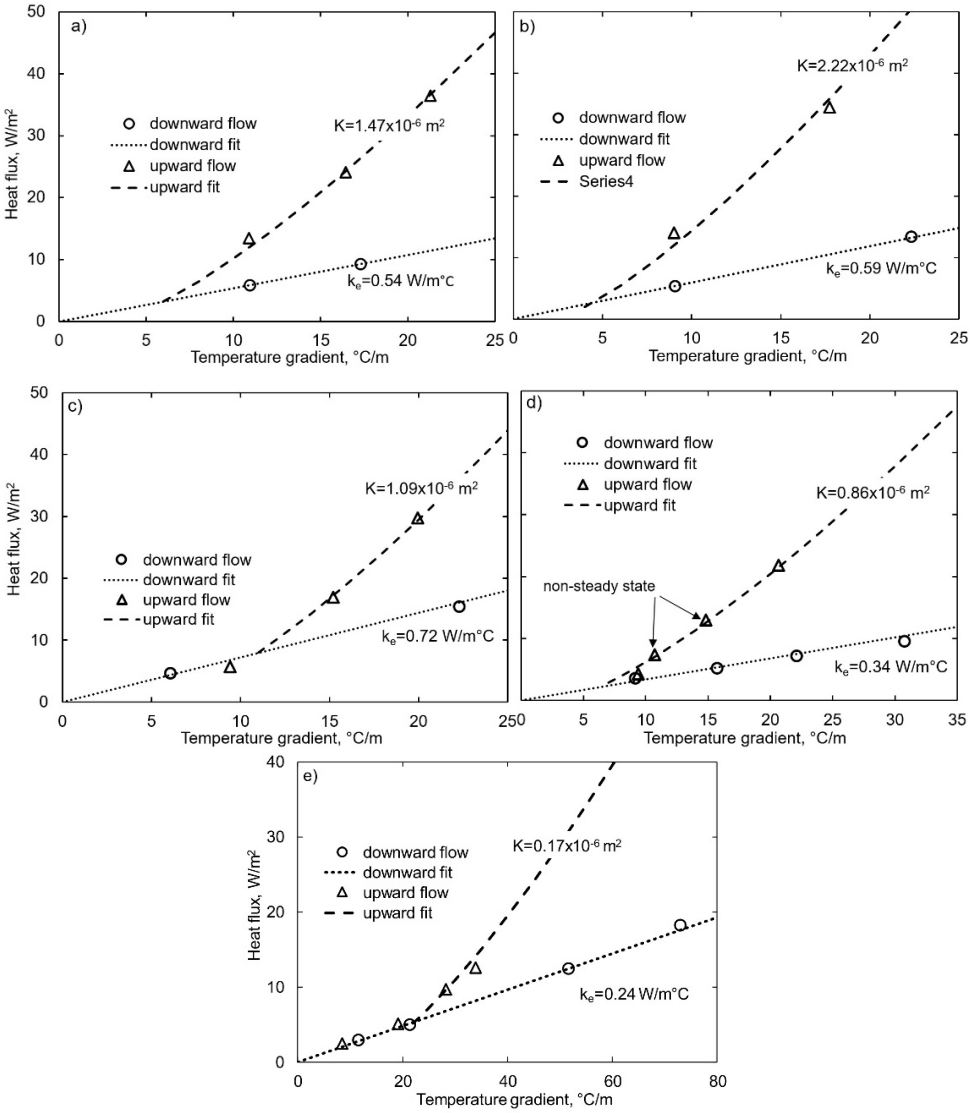

Figure 34. Comparison of experimental results under downward and upward heat flow conditions: a) 20/120 mm crushed rock material; b) 40/120 mm crushed rock material; c) 20/250 mm crushed rock material; d) 10/60 mm foam glass material; e) 10/20 mm expanded clay material.

Figure 35 plots the experimental results under downward and upward heat flow conditions. The k_e and K values and ∇T_c are specified for each of the materials. In all three crushed rock materials air convection can be initiated at relatively small ∇T in the range between 4.5 and 6.5°C/m. The ∇T_c for the foam glass material is about 11°C/m while that for 10/20 mm expanded clay is approximately 22.5°C/m. However, it must be noted here that the ∇T_c also depends on the thickness of the layer. For instance, the layer of foam glass material under field conditions (discussed in Paper VII) is only 0.6 m, and hence a larger ∇T should be required to induce convection under field conditions.

A special remark has to be made regarding the insulation materials. Given that the k_e values for all insulation materials were higher than those specified by the producers of the material, it was assumed that the experimental setup might have limitations in terms of the precise measurement of these materials. However, the initiation of air convection could clearly be seen when the temperature profile became non-linear. The Rayleigh number is directly proportional to the ∇T and intrinsic permeability, and inversely proportional to the k_e (see Eq.18). Moreover the ∇T_c refers to the critical Ra of 39.48. Given that Ra and ∇T are constants, k_e and K could be variables. In other words, decreasing k_e should require increased K to arrive at the same critical Ra and ∇T_c. Assuming that the real k_e could be two times lower, the real K value should be correspondingly twice as high. Hence if k_e is overestimated, the established K values might be significantly underestimated.

Nevertheless, the establishment of intrinsic permeability was a crucial constituent of the analysis of the field test site, as described in Paper VII.

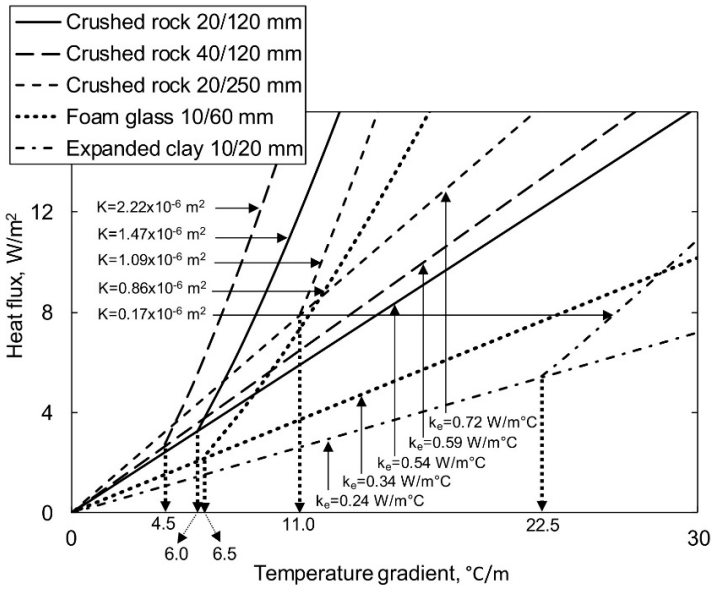

Figure 35. A compiled plot of relationship between downward and upward heat flow conditions

Intrinsic permeability is mostly governed by effective particle diameter and porosity. However, d_{10} has a much larger impact on the resulting K value. This can also be seen in the theoretical equations 22 and 23, where d_{10} is raised to a higher power compared to porosity. In addition, the variation of the porosity in the materials tested in the experimental program was minimal compared to the variation of d_{10}. The porosity varied only from 0.41 for foam glass material to 0.45 for the 20/120 and 40/120 mm crushed rock material, whereas the d_{10} varied from 0.007 m for the 10/20 mm expanded clay material to 0.038 m for the 40/120 crushed rock material. Hence the impact of different d_{10} on the resulting K is much larger than that of porosity. Figure 36 shows intrinsic permeability as a function of d_{10}^2. The figure is presented as given in Paper III, with additional results from 10/20 mm expanded clay material. It can clearly be seen that the K value increases significantly with increasing d_{10}. The last experimental results with 10/20 mm expanded clay material do not follow the trend.

It is assumed that even though air convection could be initiated in this material, the limitations of the permeant test setup do not allow the establishment of precise measurements of K in materials with low k_e.

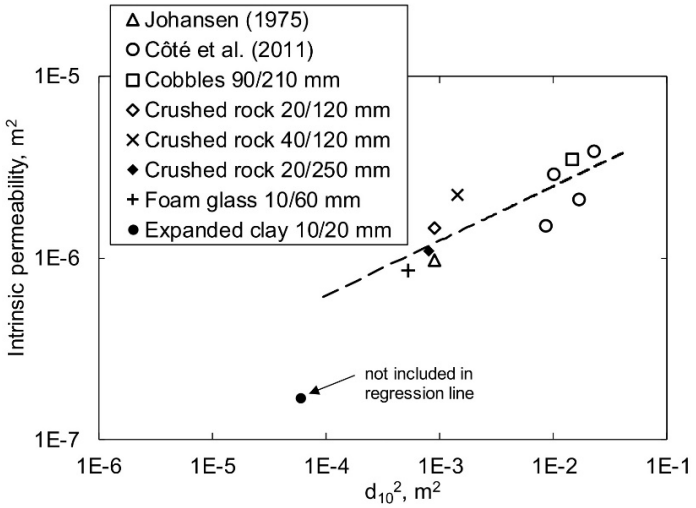

Figure 36. Influence of effective particle diameter (d10) on intrinsic permeability (K)

Although the initiation of air convection in terms of ∇T_c is largely related to the K value, other parameters can also have a significant influence. In the laboratory experiments, the other variable with a large impact is k_e. Disregarding the possible overestimation of k_e values in insulation materials, the crushed rock materials have much higher k_e than the insulation materials. Hence crushed rock materials would require much higher intrinsic permeability to have the same ∇T_c. To put the two variables into perspective, Figure 37 shows the ∇T_c as a function of K/k_e. It also shows the experimental results from the Côté et al. (2011) study. It has to be noted here that the results from these two experimental studies are compatible, given that the height of the test samples were very similar. As Figure 37 shows, the results clearly follow a trend, of ∇T_c increasing with decreasing K/k_e ratios.

Figure 37 also displays the experimental results from the 10/20 mm expanded clay material. As shown, these do not follow the overall trend. The reasons for this may be twofold. First, the K and k_e measurements might not be precise due to the physical limitations of the experimental setup. Second, the critical temperature gradients were derived from the regression line based on Eq.21. However, it was observed that, for instance, experimental measurements at a temperature gradient of 19.0°C/m showed air convection (based on temperature profile), but the value falls below the ∇T_c. Hence the real ∇T_c is probably lower than that based on the regression line of Eq.21.

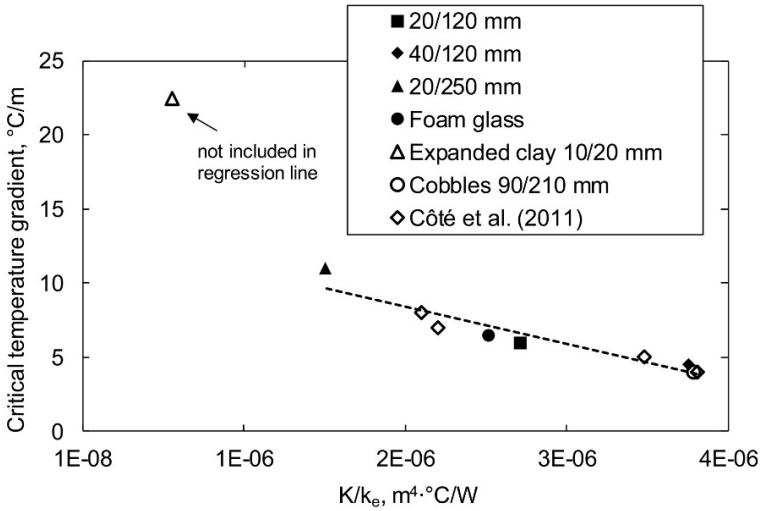

Figure 37. Critical temperature gradient as a function of K/ke

Finally, the established K values are compared to the theoretical models by Kozeny-Carman and Chapius, as displayed in Figure 38, which also shows the K values based on the experiments by Johansen (1975) and Côté et al. (2011). We must remember that the theoretical models were developed from experiments on much finer soils and hence extending them to coarse materials gives a difference of one degree of magnitude.

Figure 38 shows that the experimental results generally agree well with the theoretical values. However, the angular materials (crushed rock and foam glass) agree better with Kozeny-Carman's theoretical model, while rounded materials (except expanded clay) are closer to Chapius's model. Generally, the shape of coarse materials should have a negligible effect on intrinsic permeability. However, the results show that angular materials yield higher K values with the same α. Côté and Konrad (2009) demonstrate that the shape of the particles has a significant effect only at low α values. Hence this experimental observation highlights the need for more thorough investigation of the intrinsic permeability of coarse materials, and the most appropriate model.

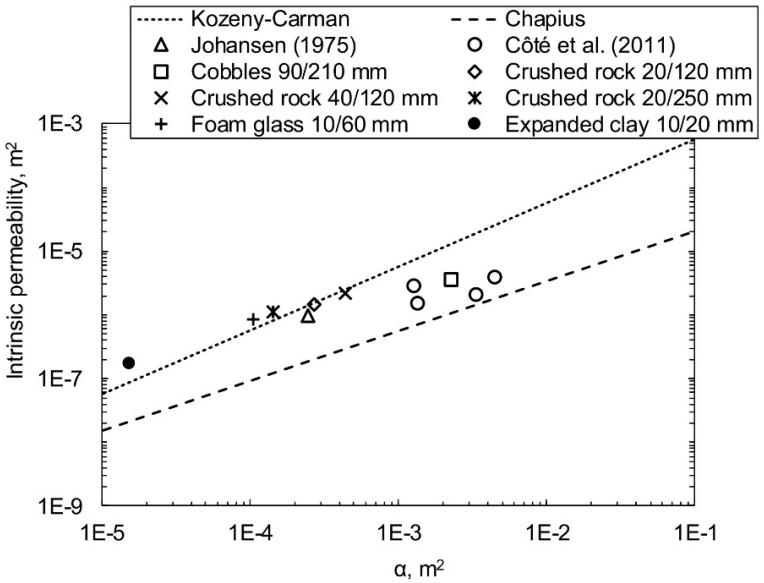

Figure 38. Measured (dots) and predicted (lines) K-α relationships

To sum up, the large-scale experiments on natural air convection together with the method proposed by Côté et al. (2011) make it possible to establish the intrinsic permeability of very coarse materials. Air convection in coarse crushed materials can be initiated at ∇T of 4.5 to 6.5°C/m with a sample thickness of 1.0 m. The results also show that air convection can be initiated in foam glass material and 10/20 mm expanded clay material at ∇T of 11.0 and 22.5°C/m respectively. However, the k_e values derived from the experimental results for insulation materials are higher than the theoretical values. The primary reason for this could be the physical limitations to testing insulation materials in an insulated box. Nevertheless, this part of the research, presented in more detail in Paper II, was a crucial step in gaining knowledge about the K values of coarse materials. The experimental results are re-analyzed, as described in the next section, using an adjusted Nu-Ra number from the numerical model (Paper IV), and then used for the analysis of field observations on possible air convection (Paper VII).

4.2.4 Numerical model

This section presents the numerical model of the large-scale experimental setup, which is presented and discussed in more detail in Paper IV. Given that the analytical Nu-Ra relationship provided by Schubert and Straus (1979) is for an idealized case (Eq.[20]), the numerical model was primarily developed to derive a test-setup-specific Nu-Ra relationship. The main differences between an idealized case and laboratory conditions are as follows: (i) the addition of sand layers at the top and the bottom of the sample; (ii) imperfect side insulation resulting in heat loss or heat input; (iii) heat flux measurements covering only 81% of the samples' top surface area.

The air convective model was first validated under adiabatic conditions, comparing the resulting Nu-Ra relationship with Schubert and Straus (1979) analytical solution. The

adiabatic air convection model was tested under two-dimensional (2D) and three-dimensional (3D) conditions. Figure 39 compares the 2D and 3D models with the analytical solution. For this model intrinsic permeability and effective conductivity were set to $1.5x10^{-6}$ m^2 and 0.6 W/m°C respectively. As Figure 39 shows, a very good agreement was obtained between the numerical and the analytical solution, validating the convective heat transfer model.

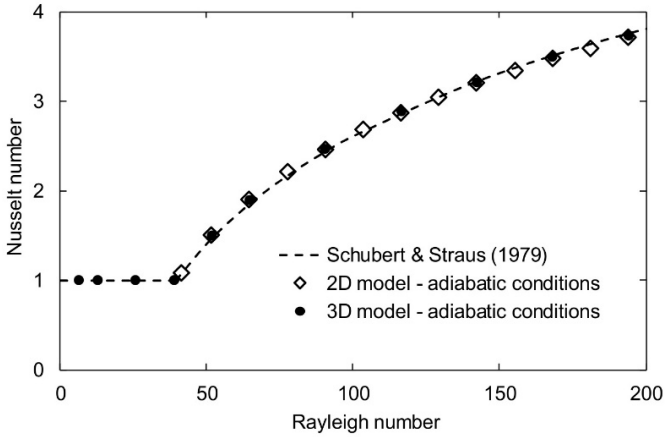

Figure 39. Comparison between analytical result by Schubert and Straus (1979) and 2D and 3D results for adiabatic conditions

After the model was validation against analytical solution, a full model replicating the laboratory experimental test setup was run. The K and k_e for the sample domain were set to $1.5x10^{-6}$ m^2 and 0.6 W/m°C. Figure 40 shows typical results of temperature distribution and air velocity pattern with an increasing temperature gradient: at a low temperature gradient the effect of air convection is minimal and the temperature isotherms are almost evenly distributed. However, when the temperature gradient is increased the effect of air convection is more pronounced, resulting in very non-uniform distribution of temperature isotherms. The Ra in the full model is considered an effective Rayleigh number (Ra_{eff}) and is calculated as in the laboratory experiments using Eq.18, using the average temperatures at the top and the bottom of the sample domain.

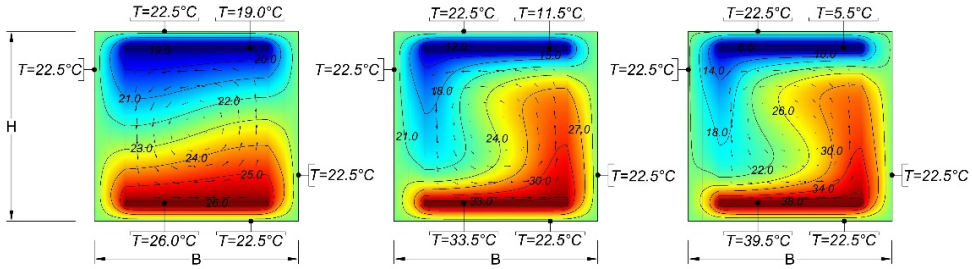

Figure 40. Convective heat transfer for different effective Rayleigh number for full model: a) Raeff=51.5; b) Raeff =99.4; c) Raeff =144.1

Figure 41 shows the final Nu-Ra relationship for the full model. The results of the 2D model are shown as a line, while the empty squares represent the solution from the 3D

model. First, the 2D and 3D model show very good agreement, indicating that the corner and side effects are minimal. Second, the resulting Nu-Ra relationship is shifted upwards compared to Schubert and Straus (1979) analytical Nu-Ra relationship. The resulting Nu-Ra relationship is mostly affected by the addition of the sand layers at the top and the bottom, creating non-uniform temperature distribution on the sample interface. Figure 41 also separately shows the effect of the side insulation and sand layers on the resulting Nu-Ra relationship. When the model was tested for the effect of the sand layers, the side boundaries were kept adiabatic. For the model result representing the effect of side insulation, the upper and lower temperature boundary was applied directly to the sample domain. The figure shows that the addition of the sand layers shifts the Nu-Ra relationship upwards, while the addition of side insulation moves the relationship downwards. Figure 41 also shows that the final Nu-Ra relationship for a full model is the result of the combined effects off the sand layers and side insulation.

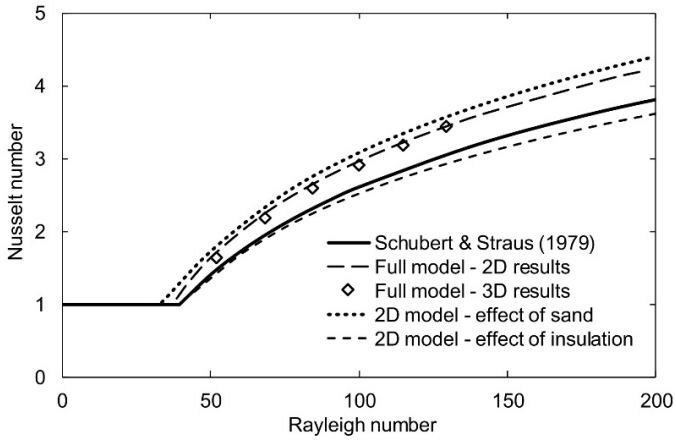

Figure 41. Nu-Ra relationship for the complete model in comparison with the effect of sand layers and insulation

Given that the addition of sand layers had the most effect on the resulting Nu-Ra relationship, the temperature distribution on the sand-sample interface was analyzed in more detail. Figure 42 shows the actual temperature distribution as well as the mean temperature on each interface. The temperature is above the mean temperature on the side of the upward air flow, while it drops on the side of the downward air flow. It is assumed that the altered temperature distribution is the primary reason for the shift in the Nu-Ra relationship. The addition of sand layers increases the effectiveness of air convection in the sample domain compared to adiabatic conditions (analytical solution). This means that for a given Ra value, the heat flux ratio ($q\uparrow/q\downarrow$) is higher when sand layers are present. However, it was also found that the Nu-Ra relationship in a full model also depends on the effective thermal conductivity of the sample domain, as explained in the next paragraph.

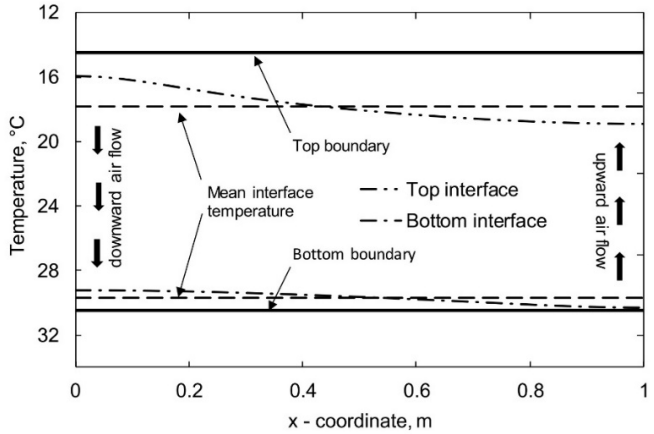

Figure 42. Temperature distribution on the top and bottom interfaces between sample and sand layers

The final Nu-Ra relationship in the full numerical model so far was established using an effective thermal conductivity of 0.6 W/m°C. Figure 43 shows the Nu-Ra relationship for a k_e range of 0.1 to 1.0 W/m°C. This range corresponds to the k_e values for unbound materials, as observed in the experimental studies presented in Papers II and III.

Heat transfer through the three-layer system (sand-sample-sand) is governed by the reciprocal effect of the thermal resistance of the sample and sand layers. This means that any change in the thermal resistance of the sand layers will also lead to changes in the resulting Nu-Ra relationship. However, given that the sand layers' thickness and thermal conductivity are fixed, the upper and lower limits of the Nu-Ra relationship can be defined with respect to the k_e of the sample domain. The lower limit of the Nu-Ra relationship corresponds to the line with k_e of 0.1 W/m°C. In this case, heat transfer through the three-layer system is purely governed by the thermal characteristics of the sample. The sand layers affect the heat flow resistance only negligibly. In fact, the Nu-Ra relationship for the lower limit corresponds to the line showing the effect of insulation (see Figure 41). A theoretical upper limit of the Nu-Ra relationship is derived using a k_e value of 5 W/m°C. In this case, thermal resistance is largely governed by the sand layers. Hence the temperature drop through the three-layer system occurs mainly in the sand layers. However, due to the large temperature distribution across the sample domain interface, effectiveness of the air convection increases significantly in the sample domain.

While k_e has a direct influence on the resulting Nu-Ra relationship, permeability has no effect. Hence the corresponding Nu-Ra relationship can be used to establish the K value. The comparison between the original K values obtained with analytical Schubert and Straus (1979) analytical relationship and those obtained with the corrected Nu-Ra relationship is presented below.

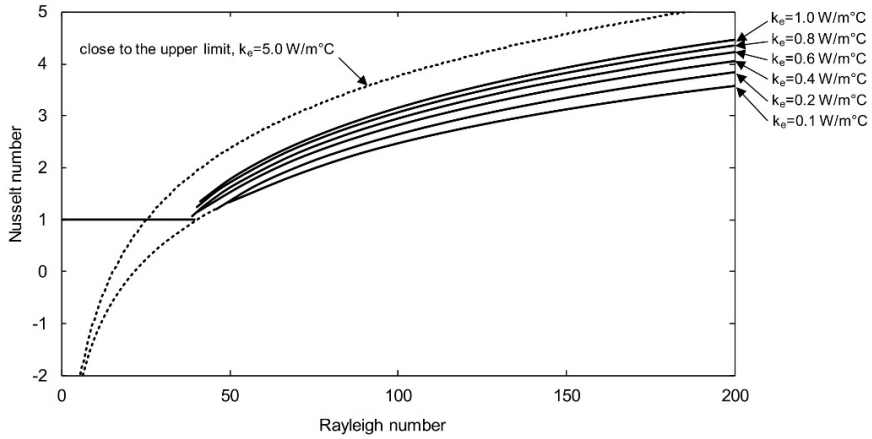

Figure 43. Effect of sample effective thermal conductivity on Nu-Ra number relationship

Since the Nu-Ra relationship is dependent on the value of k_e, it can be expressed in a more general way as follows:

[36] $$\mathrm{Nu} = \mathrm{A} \cdot \ln(\mathrm{Ra}) - \mathrm{B}$$

where coefficients A and B are logarithmic functions of k_e:

[37] $$\mathrm{A} = 0.1488 \ln(\mathrm{k_e}) + 1.9588$$

[38] $$\mathrm{B} = 0.4232 \ln(\mathrm{k_e}) + 5.9267$$

Figure 44 shows the K values originally established (see Papers II and III) and those re-established using Eq.[36]. The figure also shows the results of the study by Côté et al. (2011) and the values re-established by Dhyser (2013). It shows that using Schubert and Straus (1979) analytical Nu-Ra relationship yields higher K. Moreover the difference is higher for materials with higher k_e. Generally the re-established K values are 8% (foam glass) to 26% (cobbles) lower than the original values presented in Paper II and III.

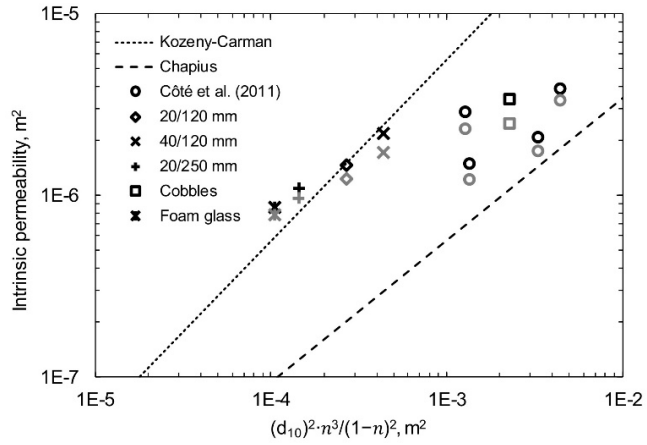

Figure 44. Comparison between experimental and theoretical values of intrinsic permeability

Generally, the method proposed by Côté et al. (2011) to establish the intrinsic permeability of coarse materials gives reasonably good results. However, given that the method is based on an idealized case of a perfectly insulated sample to which uniform temperature is applied, the real K values might be different. The study presented in Paper IV develops a numerical model to account for the effect of any deviations from the idealized case in the resulting Nu-Ra relationship, and shows that using a test-setup-specific Nu-Ra relationship yields lower K values than those established before using Schubert and Straus (1979) Nu-Ra relationship.

4.3 Test site

Although the test site in Røros consisted of ten different sections, only two road sections were analyzed in detail for the possible presence of natural air convection. Paper VII presents an analysis of the field test site and a numerical model to further validate the heat transfer characteristics. The two sections discussed in Paper VII are Ro1 and Ro6 (see Figure 11). These are constructed from open graded materials, each, however, with a significantly different structure. Ro1 incorporates a subbase layer (0.8 m) of 20/120 mm crushed rock material and an underlying frost protection layer (1.0 m) of 40/120 mm material. Ro6 incorporates a shallow 0.2 m subbase layer and an underlying insulation layer of foam glass material with particle size of 10/60 mm (see Figure 11 for full structure). The results for these two sections, with particular focus on the layers of open graded materials, are presented in the next two subsections. Field observations and a simple analysis of natural air convection are presented in section 4.3.1, and the results of the numerical modeling are given in section 4.3.2.

4.3.1 Field observations

Temperature measurements

Figure 45 shows the air and road surface temperatures for the period from October 2016 to May 2018. The whole test site was monitored for two consecutive winters. The first winter (2016/2017) resulted in an air freezing index (FI_a) of 25368°C·h (1057°C·days) and a surface freezing index (FI_s) of 23160°C·h (965°C·days). The second winter (2017/2018) was significantly colder and the corresponding FI_a and FI_s were 36864°C·h (1536°C·days) and 36744°C·h (1531°C·days) respectively. Given that the research focused primarily on the ground cooling period, a more thorough investigation was conducted during the second winter, when the period for the analysis and the modeling was October 2, 2017 to April 19, 2018. This was when upward heat flow based on temperature gradient (∇T) was observed in any of the four open graded layers of interest. The ground cooling period generally starts before freezing takes place and finishes before the ground is entirely thawed.

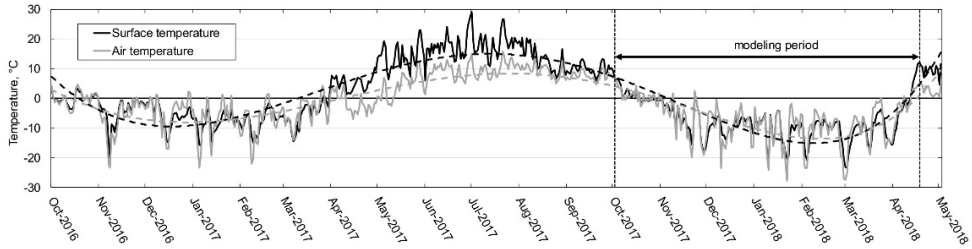

Figure 45. Air and surface temperature from October, 2016 to May, 2018 with modeling and anlaysis period set from October 2, 2017 to April 19, 2018

Figure 46 shows the temperature profiles of Ro1 and Ro6. These were provided on the 2nd of each month throughout the cooling period. Figure 46a shows that for the last three months the frost front penetrated the silt layer in Ro1. However, defining the location of the front precisely was difficult, primarily due to the narrow temperature range in the silt layer and the relatively large error in the temperature sensors. For instance, the temperature difference between the top and the bottom of the silt layer was only approximately 0.4°C. This is well within the relative error of thermocouple sensors. However, moisture sensors, as shown later, also provide useful information about ground freezing.

As expected, the layer of foam glass material in Ro6 provided very good insulation. As a result, based on the temperature observations the frost front penetrated the LFPL only marginally. The silt layer remained unfrozen the entire time. The insulation layer, however, due its very low thermal conductivity, resulted in a very high ∇T which contributed to the initiation of air convection in this layer.

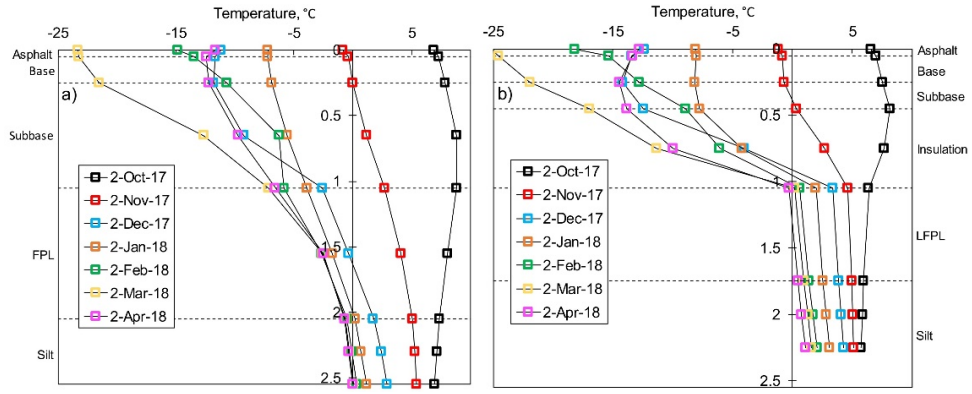

Figure 46. Temperature distribution in road sections on the 2nd of each month thoroughout the cooling period of 2017/2018: a) road section Ro1; b) road section Ro6

Moisture sensor measurements

Figure 47 shows the moisture sensor measurements from field observation from December 2016 to May 2018. The moisture sensors in each road section were installed as follows:

- Ro1-moisture sensor M1 (‘M1’): silt layer
- Ro2-M1: middle of frost protection layer

- Ro2-M2: top of frost protection layer
- Ro3-M1: silt layer
- Ro3-M2: middle of frost protection layer
- Ro3-M3: top of frost protection layer
- Ro3-M4: base layer
- Ro5-M1: silt layer
- Ro5-M2: bottom of lower frost protection layer
- Ro5-M3: middle of insulation layer.

The moisture sensors installed in the silt layer in the different sections gave measurements in the range of 40-50%. Given that the material is saturated, this value also corresponds to its approximate porosity. The measurements from moisture sensor M1 in Ro1 also confirm freezing in the upper part of the silt layer.

Measurement of the moisture content in coarse aggregates is complicated, as the moisture sensors are typically produced for measurements in fine soils. Thus they are incapable of direct measurements in coarse aggregates as the particle size is larger than the measurement range permits. Because of this the moisture sensors in all crushed rock material layers were installed only in the fine fraction of 0/4 mm material, assuming that the fraction of material below 4 mm retains the majority of the water in a certain layer. Therefore the volumetric water content measured by the moisture sensors was related to the fraction of 0/4 mm material in the total mass. For instance, the moisture sensors in the fine graded frost protection layer indicated an average volumetric water content of 22% (Ro2-M2). Based on the particle gradation presented in Figure 47, the fraction of particles finer than 4 mm is equal to about 53%. Hence the measured volumetric water content relates to 11% of the water. This corresponds to the gravimetric water content of approximately 6%.

The final moisture levels assumed for the numerical model are given later in Table 5.

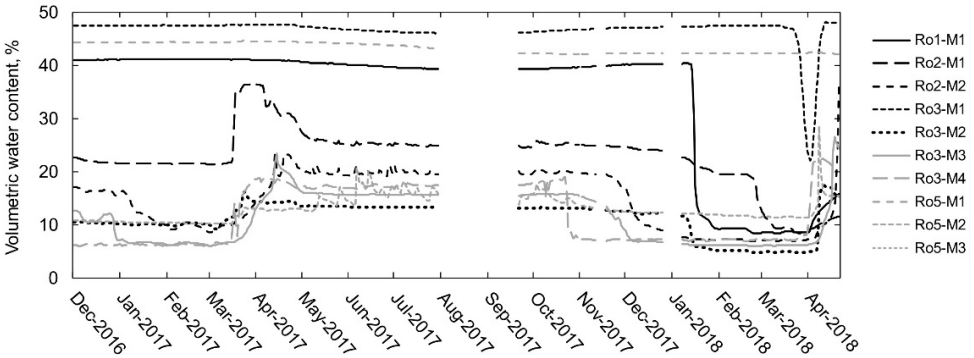

Figure 47. Moisture distribution in road and railway sections, December 2016 to June 2018

Analysis of possible air convection based on field observations

As clearly shown in the results presented in 4.2.3, air convection is initiated only when the ∇T_c is exceeded. Under the laboratory conditions presented in Paper III, the critical ∇T_c is 6°C/m for the subbase material (20/120 mm), 4.5°C/m for the frost protection layer (40/120 mm) and 6.5°C/m for the foam glass material (10/60). For a relative comparison with laboratory conditions, the ∇T in field conditions is needed; this can easily be calculated

based on the temperature measurements. Figure 48 presents the measured temperatures (dashed and dotted lines) at the top and the bottom of the subbase layer and FPL in Ro1. The figure also presents the calculated ∇T (solid lines) for the two layers throughout the cooling period. Figure 48 shows that both layers were subject to relatively high ∇T exceeding the critical values defined under laboratory conditions. More precisely, the subbase layer in Ro1 was subject to a ∇T higher than critical for 35% of the time. The ∇T in FPL exceeded the critical value for 32% of the cooling period. The maximum ∇T observed for subbase and FPL layer was 18 and 9°C/m respectively.

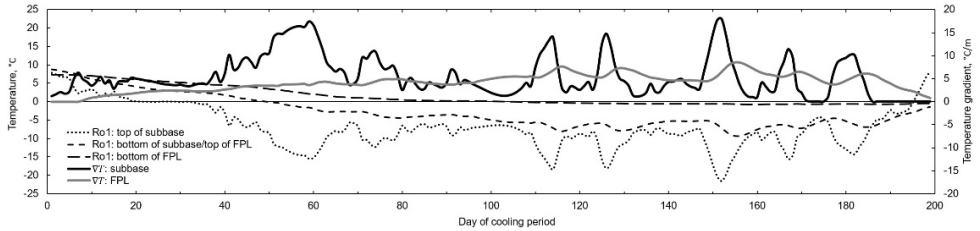

Figure 48. Temperature conditions for open graded material layers in road section Ro1 for cooling period October 2 2017 to April 19 2018 (200 days): dashed and dotted line denote temperature at top and the bottom of subbase and FPL (scale on left axis); solid line –denotes temperature gradient in subbase and FPL (scale on right axis)

Figure 49 shows the measured temperature distribution (dashed and dotted lines) at the top and the bottom of the subbase and in the insulation layer of Ro6. The figure also presents the calculated ∇T (solid lines) in both open graded layers. These two layers were subject to even more extreme ∇T than Ro1. The subbase layer exceeded critical ∇T for 49% of the time and reached a maximum value of 39°C/m. The insulation layer was subject to ∇T exceeding the critical value for 88% of the cooling period and reached a maximum value of 31°C/m.

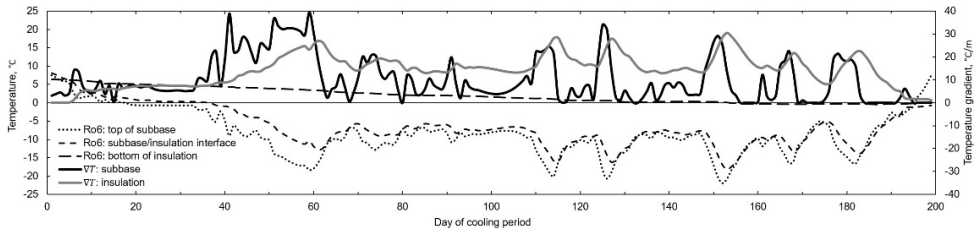

Figure 49. Temperature conditions for open graded material layers in road section Ro6 for cooling period October 2, 2017 to April 19, 2018 (200 days): dashed and dotted line denotes temperature at top and the bottom of subbase and FPL (scale on left axis); solid line denotes temperature gradient in subbase and FPL (scale on right axis)

Figure 48 and 49 clearly show signs of high potential air convection in the open graded material layers for a large proportion of the cooling season. However, the initiation of convection depends on multiple factors. The factors governing it are those that define the Rayleigh number as given in Eq.18. The foremost difference when comparing conditions in the laboratory experiments and the field test site is layer thickness. The FPL is the only layer with the same thickness as that in the laboratory experiments, and hence in terms of critical Ra the height of the FPL has no effect. On the contrary, the subbase layer in Ro1 and Ro6 and the insulation layer in Ro6 are not as thick as those tested under laboratory conditions. For instance the subbase layer in Ro6 is only 80% as thick as that in the laboratory

experiment. For the same critical Ra value, 39.48, and given that Ra is a function of H^2, critical ∇T must increase from 6 to 9.4°C/m. Hence height has a very big impact on critical ∇T.

To account for all the parameters affecting the magnitude of convection, an apparent Rayleigh number (Ra*) could be calculated for each of the layers for each day of the cooling period. However, for simplification, the air properties are considered constant. Hence the variables for the calculation of Ra* are thickness of a layer (H), intrinsic permeability (K), effective thermal conductivity (k_e) and the corresponding ∇T on a given day. Figure 50 presents the calculated Ra* for the four open graded materials throughout the cooling periods, showing that taking into account all the affecting parameters, only the FPL and insulation layer exceed the critical Ra value. None of the subbase layers exceed critical Ra. In the subbase layer in Ro6 this is primarily due to the effect of its reduced thickness of only 0.2 m compared to 1.0 m in the laboratory. In Ro1's subbase layer it is the combined effect of lower permeability, higher effective conductivity and decreased height compared to the laboratory experiments. The subbase material used in the field construction contains a small amount of fine material below 20 mm which accounts for about 5% of the total mass. It was assumed that the fine material fills the pores between the larger particles, thus reducing permeability, and that the subbase material retains a small amount of water, increasing effective thermal conductivity.

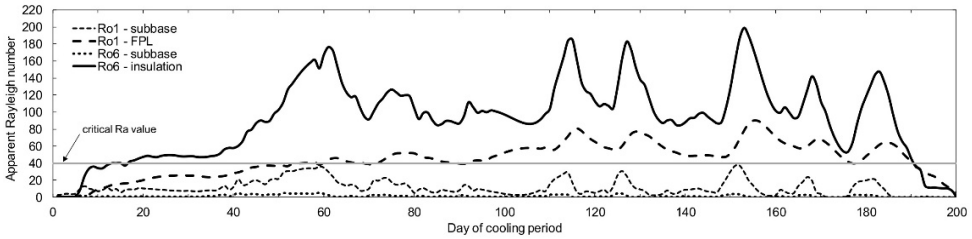

Figure 50. Ra for the open graded materials for cooling period from October 2, 2017 to April 19, 2018*

In summary, although in laboratory conditions convective heat transfer was induced in all of the open graded materials, the same probably does not happen under field conditions. The subbase material in field conditions, with different H, K and k_e to those in the laboratory, showed Ra* below the critical value. In contrast, the FPL and especially the insulation layer, which was only 60% as thick as that in the laboratory experiments, showed Ra* well above the critical value of 39.48. Hence based on the field observations and the material properties of the laboratory experiments, it is probable that air convection occurred in the FPL and insulation layer during the cooling period.

4.3.2 Numerical modeling

To further analyze the presence of air convection in Ro1 and Ro6, a numerical model was developed. Field temperature measurements are used to set the upper boundary and initial temperature conditions. The materials' thermal properties are largely based on the laboratory investigations into thermal conductivity and intrinsic permeability. Thermal conductivity is calculated based on the model described in section 2.2 and validated in Paper VI. The

thermal conductivity model uses input parameters for the thermal conductivity of solid particles discussed in Paper V. The intrinsic permeability of the frost protection layer and insulation layer is based on the laboratory experiments presented in Paper III. The final K used in the model was re-established based on the adjusted Nu-Ra relationship presented in Paper IV. The material gradation for subbase material is not exactly the same as that in laboratory conditions, hence the final K value was calculated using Eq.22. Given that the re-established K values shown in Paper III are higher than the ones based on the original Nu-Ra relationship, the actual K value for the subbase may also be lower.

Table 5. Summary of material properties used for numerical model

Material	ρ_d, kg/m3	ρ_s, kg/m3	n	w%	k_s, W/m°C	k_{uf}, W/m°C	k_f, W/m°C	C_{uf}	C_f	K (x10^{-6}), m^2
Asphalt	-	-		-	-	1.35	1.35	1840	1840	-
Base layer	1979	2788	0.29	4	3.32	1.51	1.57	2019	1834	-
Subbase layer	1623	2788	0.42	1.5	3.32	0.77	0.73	1484	1427	0.86
FPL	1536	2788	0.45	1	3.32	0.67	0.63	1373	1336	2.41
LFPL – typical grading	1784	2788	0.36	5.6	3.32	1.32	1.46	1937	1706	-
Foam glass	223	380	0.41	1	-	0.2	0.2			0.86
Silt	1608	2680	0.40	24.9	3.79	1.81	3.04	3047	2123	-
Clay	1460	2660	0.45	30.8	3.29	1.53	2.75	1334	2094	-

Figure 51 shows a typical temperature distribution and air velocity pattern for road section Ro1 on April 2, 2018. As expected, with the given material parameters convection was initiated only in the frost protection layer. In this numerical simulation 8 air convection cells formed with alternating directions. Figure 51 shows that the frost front has penetrated the underlying silt layer. This is in agreement with the field observations shown in Figure 46a. However, it can be also seen that due to the effect of air convection the frost front is uneven. Generally the frost front is minimal in a location where two convection cells form a downward air flow, and maximal where two air convection cells form an upward air flow.

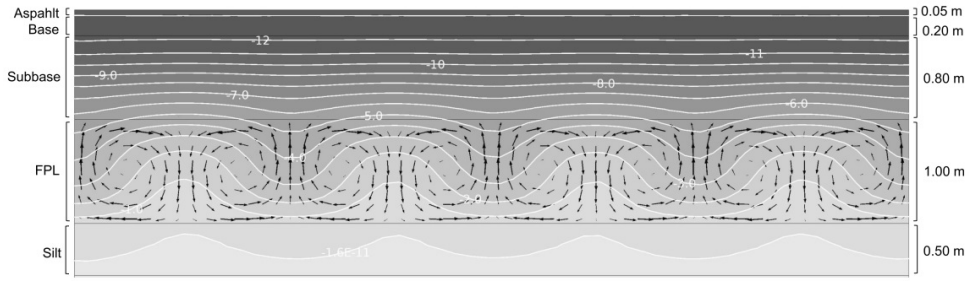

Figure 51. A typical temperature distribution and air velocity pattern in road section Ro1 (April 2, 2018)

Figure 52 shows a typical temperature distribution and air velocity field for Ro6 on April 2, 2018. As expected, the high temperature gradient imposed on the insulation layer together with its relatively high permeability initiate air convection in this layer. In this numerical

simulation, 13 air convection cells formed. Figure 52 shows that on the given date the frost front was in the bottom part of the lower frost protection layer. This is considerably deeper than in the field observations (see Figure 46). This might mean that the effect of convective heat transfer in the insulation layer has been overestimated, resulting in deeper frost penetration as discussed more thoroughly in the next paragraphs.

In the results shown in Figure 51 and 52 two important aspects have to be noted. The air convection significantly alters the temperature distribution and creates uneven frost penetration. First, uneven frost front penetration could result in differential heaving. This is probably the case, as shown in Figure 51, when the frost front penetrates the frost-susceptible layer at different rates and depths. Second, the altered temperature distribution results in different temperature profiles depending on the location, making it difficult to compare the numerical results with those from the field observations.

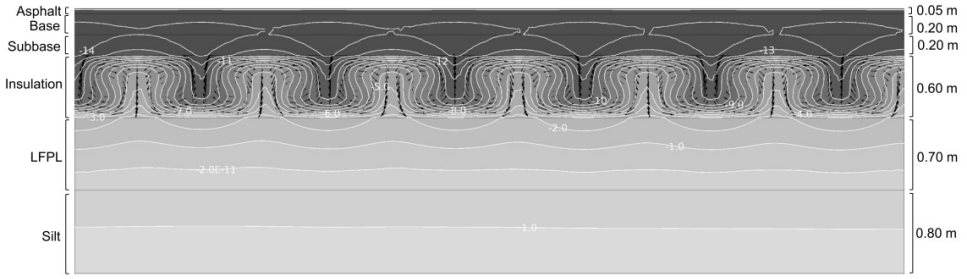

Figure 52. A typical temperature distribution and air velocity pattern in road section Ro6 (April 2, 2018).

Given that the temperature in the field was measured only on one vertical cutline in the middle of each section, different temperature profiles from numerical model should be derived for comparison. Figure 53 compares temperature profiles from model and field measurements for Ro1 and Ro6. Three distinct temperature profiles were selected from the numerical model: (i) at the location where two convection cells create an upward air flow (solid line), (ii) at the center of an air convection cell (dashed black line) and (iii) at the location where two convection cells create a downward air flow (dotted line). The figure also provides the conduction-only solution (gray dashed line). As Figure 53 shows, the model's predictions in general are relatively well in agreement with the temperature measurements from the field test site. However, none of the temperature profiles derived from the numerical model are in very good agreement with the field measurements. In fact the field measurements are very limited and do not provide a sufficient amount of information to reveal a temperature profile that would resemble an air convection pattern. To be able to clearly verify the presence of air convection in the field, the distance between the temperature sensors should be much smaller. Moreover, in an ideal case the temperature sensors should create a grid. For instance, in Goering (1998) study of air convection a grid of thermocouples at vertical and horizontal spacings of 0.6 m was installed in an open graded embankment. However, for the test site studied here the cross-section in the transverse and longitudinal directions is rectangular, and hence predicting the direction of the air convection cells is nearly impossible.

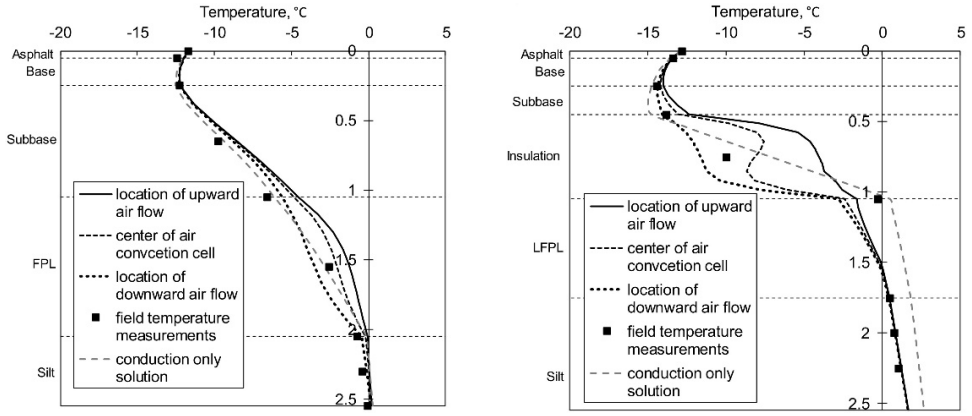

Figure 53. Comparison between field temperature measurements with temperature profile from numerical model at different location on April 2, 2018: a) Ro1; b) Ro6. The solid line represents a cut line in the location of downward air flow (in model); the dashed black line represents temperature profile in the center of an air convection cell (in model); the dotted line represents temperature profile in the location of upward air flow (in model); the dashed gray line represents conduction-only solution; the filled dots are temperature measurements from the field

For comparison over a longer period of time an average temperature profile can be calculated from numerical model. Given that the location of field sensors with respect to convection cells is unknown, this still gives a reasonable comparison. Figure 54a and 54b shows the numerical model and field temperature measurements for Ro1 and Ro6 respectively. The temperatures displayed were noted on the 2nd of each month. The dashed lines represent the average temperature profile derived from the numerical model, while the squares show the field temperature measurements. The average temperature profile shown in Figure 54a agrees well with the temperature measurements from the field. However, it should be emphasized here that the magnitude of possible convective heat transfer in Ro1 is smaller than that in Ro6. Hence a temperature profile derived from a numerical model with no convection would be fairly similar to the average temperature profile from a numerical solution with convection. In Figure 54b the field measurements and the numerical solution agree reasonably well. However, a noticeable difference can be observed on the insulation and LFPL interface. The field temperature measurements show higher temperatures than those of the numerical solution most of the time. In fact the temperature measurement from the test site does not fall within the range set by the distinct temperature profiles in the numerical model (see Figure 53b). Two possible reasons are discussed here. First, the heat capacity of the LFPL is higher than assumed. Although the real heat capacity could be higher, it is highly unlikely that the water content is underestimated by such an extent. The second reason for the lower temperature in the numerical model is overestimation of heat extraction through the insulation layer. This could originate from overestimated permeability, resulting in more intense air convection. The permeability of the foam glass material was established based on laboratory measurements of the uncompacted sample presented in section 4.2.3. Although the coarse material would not have a high compaction rate, the foam glass particles are rather fragile and during its compaction its particles are not only rearranged but also broken, with angular edges becoming more rounded. Hence it is

quite likely that permeability under field conditions could be lower than expected, resulting in an overestimated heat extraction rate in numerical model.

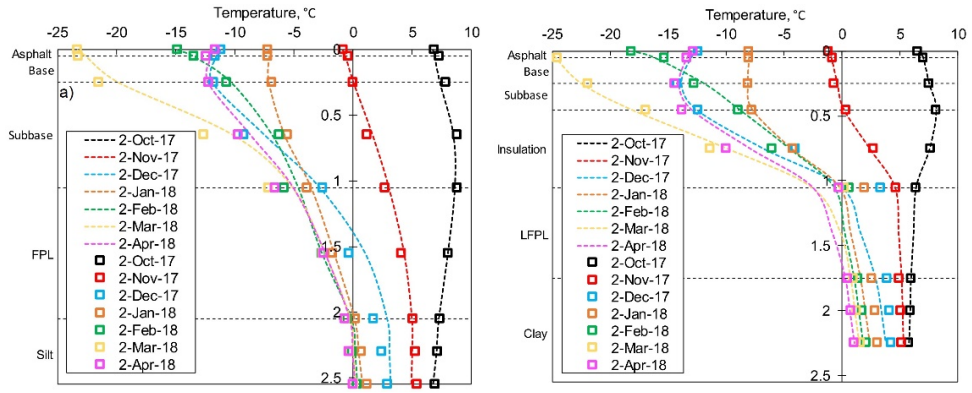

Figure 54. Comparison of temperature profiles on the 2nd of each month: field observations and numerical model from a) road section Ro1 and b) road section Ro6. Squares show temperature measurements from the field and dashed lines show the model results.

To further compare the field observations with the results from the numerical model, the magnitude of convection can be compared. The temperature measurements from the field test site were used to calculate Ra*. Ra* could also be calculated from the numerical model based on the temperature distribution. However, the numerical model makes it possible to derive the convective heat flux (q_c), which directly shows the magnitude of convection in units of W/m^2. The average heat flux over a certain layer must be calculated, given that heat flux changes depending on location. Figure 55 shows Ra* and q_c in Ro1. While the measures do not have common units, they clearly show a similar trend with convective heat flux increasing with increasing Ra*. Convective heat flux shows values above zero when Ra* reaches the critical value of approximately 40 on about day 60, corresponding to the beginning of December.

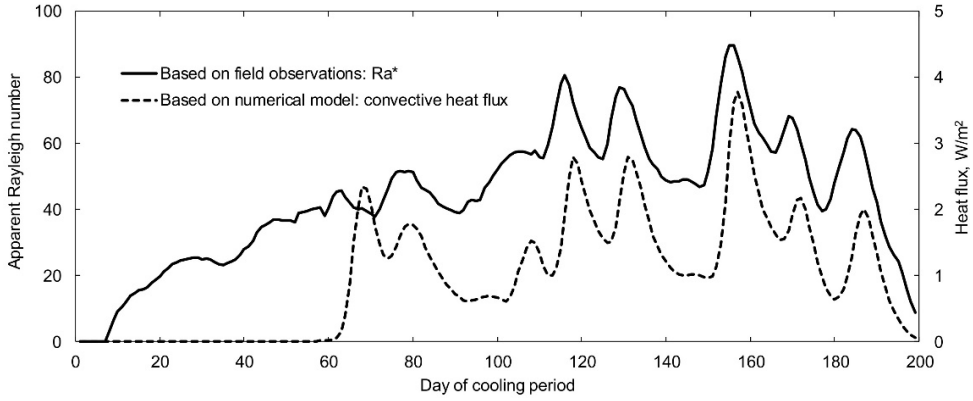

Figure 55. Comparison between Ra from field observations and convective heat flux value from numerical model for frost protection layer in road section Ro1*

Figure 56 compares Ra* and q_c in Ro6 throughout the cooling period. Both measures closely follow the same trend. The convective flux is initiated on approximately day 20, when the Ra* reaches the critical value.

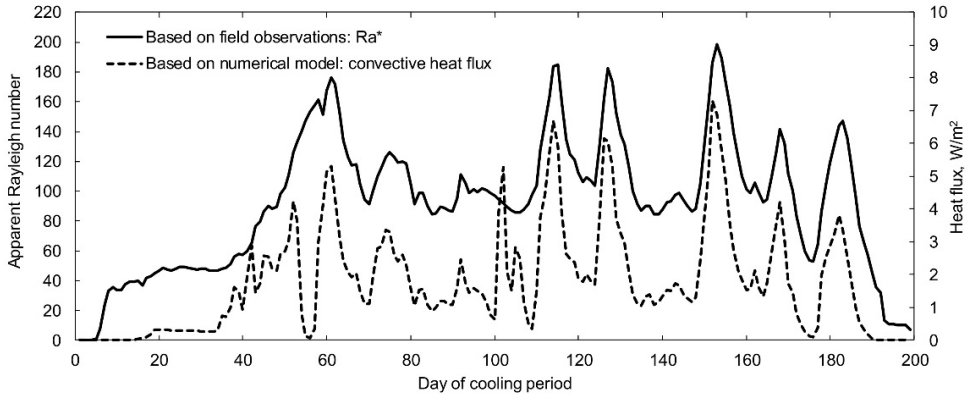

Figure 56. Comparison between Ra from field observations and convective heat flux value from numerical model for frost protection layer in road section Ro6*

To sum up, Figure 55 and 56 clearly show the possible presence of air convection under field conditions in the two open graded material layers. Calculating Ra* based on field measurements is an easy way of estimating the magnitude of convection. The numerical model can give direct measurements of air convection in units of W/m^2. However, both Ra* and q_c rely heavily on established intrinsic permeability based on the laboratory experiments, where testing conditions can be well controlled compared to in the field. The main factors influencing the analysis of the field and numerical results should be noted: the field temperature analysis is influenced by the actual layer thickness (compared to the design), the assumed location and the accuracy of the temperature sensors. However, with a relatively wide temperature range the temperature sensor error will have a negligible effect. The accuracy of the numerical model mainly depends on estimated material properties such as intrinsic permeability and thermal conductivity.

Nevertheless, the laboratory study presented in Paper III clearly shows that air convection can be initiated in road construction materials at fairly low temperatures. Extending the scale to a full road structure, as presented in Paper VII, finds that the temperature gradient imposed on the open graded layers can be much higher than those under laboratory conditions. Hence even though the material properties in the field can differ from those in the laboratory, the open graded material has a high risk of natural air convection. The main consequences of this in a seasonally freezing environment are increased frost penetration depth, and differential heaving if frost-susceptible soils freeze.

5 Conclusion and future work

This section summarizes the main conclusions drawn in the research papers included in this study, and from the results and discussion above. Final remarks are made about future work and recommendations for frost protection on roads and railways, and about extending knowledge of the thermal properties of granular materials.

5.1.1 Conclusions

In northern countries thermal design is a crucial part of overall road and railway design. Given that such structures are often constructed on frost susceptible soils, frost penetration depth should be limited or minimized to avoid frost related problems such as frost heave and loss of bearing capacity in the spring thaw. The common method is the construction of a frost protection layer of crushed materials or insulation materials such as expanded clay or foam glass. The thermal design of transport structure requires good knowledge of the thermal properties of these materials. Thermal conductivity is the governing heat transfer mechanism in the majority of construction materials. The current regulations in Norway allow the use of coarse open graded materials in which heat transfer can be significantly higher due to interparticle radiation and natural air convection. Relying on the conventional approach of thermal design based on thermal conductivity might lead to the underestimation of frost penetration depth and unexpected frost heave problems.

The following paragraphs present the main conclusions and research findings from the associated papers:

- For an accurate estimate of the thermal conductivity of crushed rock materials, the thermal conductivity of solid particle (k_s) should be well defined. This study has investigated several methods of directly and indirectly measuring or estimating the k_s values of nine different materials and finds that each has challenges to overcome. Measuring rock core samples is the only way to directly measure k_s. However, the results showed lower values than any other method. It was speculated that surface contact resistance between the sample and the heat flux sensors could be the main reason for this effect. A geometric mean method based on the proportion and thermal conductivity of each of the minerals produced reasonable estimates of k_s. However this method relies on the precise measurement of mineralogical composition. It is assumed that the geometric mean method could be used if no k_s measurements are available. This study found that the most promising estimate was produced from saturated samples and back-calculating k_s values. These estimates were used as an input parameter for the subsequent thermal conductivity model validation.
- In total 328 measurements of 42 unfrozen and frozen crushed rock samples with varying moisture content were performed to create a dataset for the validation of the thermal conductivity model. In this study a generalized thermal conductivity model proposed by Côté and Konrad (2005b) was validated and adapted. The study finds that the original model predictions are in relatively good agreement with the experimental measurements. However, the model yielded slightly higher values, especially for low range of moisture contents. Given that the original model was calibrated on a specific experimental dataset, adapting the model for another set of materials required some minor adjustments. The model incorporates

two structure parameters: β, accounting for dry thermal conductivity, and κ, accounting for structure effects in the k_r-S_r relationship. This study finds that slight adjustment to the β and κ parameters increased the model's accuracy. The validated and calibrated thermal conductivity model was also used to estimate the thermal conductivity of crushed rock materials under field conditions.

- The large-scale experimental test setup was inspired by and based on some of the preceding studies in the field on natural air convection in coarse materials. This study reviewed some of the experimental setups and the main differences and improvements over time. It also reviewed Côté et al. (2011) proposed method for the establishment of intrinsic permeability (K) based on experimental results. The method is based on Schubert and Straus (1979) analytical Nusselt (Nu) and Rayleigh (Ra) number relationship. This study reviewed some of the preceding experimental studies and re-analyzed some of the experimental results to derive a value for K. It found that comparing the results from different experimental setups can be difficult due to different sample geometry and boundary conditions, and lack of information about the formation of air convection cells. However, it is still possible to establish K values with a certain degree of confidence. This method was further used to validate the experimental test setup used in this doctoral study, and to estimate the K values of different construction materials.
- The experimental program on the measurement of air convection was initiated with two phases of test setup validation. The first included a test with a sand sample to validate the experimental test setup for heat-conduction-only conditions. The measured thermal conductivity agreed well with the values found in the literature. The second phase included a test using natural cobbles, with the objective of comparing the established value of intrinsic permeability (K) with that from a study using very similar materials. Although the air convection was not initiated in a two-dimensional pattern, the established K values were in good agreement with those of the similar materials, validating the experimental setup for air convection flow.
- After the validation phases in the large-scale test setup, the experimental program continued, measuring air convection in six different materials. These included three crushed rock materials (20/120, 40/120 and 20/250 mm), two expanded clay materials (0/32 and 10/20 mm) and foam glass material (10/60 mm). The experimental results show that natural air convection can be initiated in all three crushed rock materials at a relatively low temperature gradient ranging between 4.5 and 6.5°C/m. The established permeability values for the 20/120, 40/120 and 20/250 mm materials correspond to 1.47×10^{-6}, 2.22×10^{-6} and 1.09×10^{-6} m^2 respectively. It was also found that natural air convection could be initiated in 10/20 mm expanded clay and foam glass material at temperature gradients of 11 and 22.5°C/m respectively. The K values established based on the experimental measurements were 0.17×10^{-6} m^2 for 10/20 mm expanded clay material and 0.86×10^{-6} m^2 for foam glass material. No air convection was initiated in the 0/32 mm expanded clay material. The experiments on insulation materials found that the effective thermal conductivity of all three materials was much higher than the theoretical values. It is possible that the experimental setup included some limiting conditions with regard to highly insulating materials tested in an insulated box. Hence although it was possible to establish K values based on the experimental results, one should be critical when applying them to other analyses.

- The method used to establish the K values relies on an analytical Nu-Ra relationship in a square enclosure heated from below. In this idealized case the side boundary conditions are adiabatic and a uniform temperature is applied at the top and the bottom of the sample. However, in the laboratory the side insulation was imperfect and interface sand layers were added to increase the transfer of heat from the heat exchange plates to the sample. These deviations from the idealized case changed the resulting Nu-Ra relationship. Hence a numerical model representing the large-scale experiment was developed to account for any deviations in the analytical Nu-Ra relationship. It was found that the addition of interface sand layers had the largest effect on the resulting Nu-Ra relationship by altering the temperature conditions applied on the sample's top and bottom surfaces. It was also found that the Nu-Ra relationship is dependent on the effective thermal conductivity of the test sample. Hence the Nu-Ra relationship from the numerical model was expressed as a function of the effective thermal conductivity of the sample. Finally, the K values were re-established using the test-setup-specific Nu-Ra relationship. The results show that the re-established K values were 8-26% lower than those established using the analytical Nu-Ra relationship. The re-established K values were further used to analyze possible air convection in road structural layers under field conditions.
- In order to evaluate the performance of crushed rock and insulation materials in real environmental conditions, a full scale test site was constructed with six road and four railway sections. The current study focused on two road sections constructed with layers of open graded materials. The first section incorporated an open graded subbase and frost protection layer, and the other section was constructed with a shallow open graded subbase layer and an underlying foam glass layer. The field observations showed that the temperature gradients imposed on each layer significantly exceeded the critical gradient necessary to impose air convection under laboratory conditions. However, air convection also depends on layer thickness, which was different from the laboratory experiments in some cases. Hence an apparent Rayleigh number was calculated to account for all parameters defining the initiation of air convection. The results showed that natural air convection could be initiated only in the open graded frost protection layer and the foam glass material layer. To further validate possible air convection, a numerical model was developed. The model clearly showed the presence of natural air convection. However, it was observed that the model probably overestimated the magnitude of the air convection in the foam glass layer. The model relies on intrinsic permeability measured under laboratory conditions. Given that material is compacted under field conditions, the extent of air convection is probably less than expected. Nevertheless, the numerical model showed the potential risk of increased frost penetration depth and possible differential heaving.

To sum up, knowledge of the thermal properties of construction materials is crucial for thermal design of road and railway structures. This study has shown that a fairly simple thermal conductivity model can be adopted for the estimation of thermal conductivity in crushed rock materials. This could greatly improve the general estimation of frost penetration depth. The coarse open graded materials, although good for their mechanical properties, pose the risk of increased heat transfer due to convection. The field observations show that temperature gradients imposed on open grade layers may far exceed the critical temperature gradients observed in laboratory conditions with a 1.0 m thick layer. Hence the use of very

coarse materials should be limited to a certain thickness to limit possible air convection and thereby avoid frost-related problems.

5.1.2 Recommendations and future work

This study shows the importance of knowledge of the thermal properties of unbound materials and the potential risk of increased heat extraction due to natural convection. It has shown that a simple thermal conductivity model can be adjusted to the use of local materials. However, the model requires knowledge of three main parameters – the thermal conductivity of rock material, porosity and moisture level. First, the thermal conductivity of rock materials can easily be estimated since most producers of such materials can provide their mineralogical composition. Second, better knowledge should be developed about the compaction rate of different material gradings. Third, while the moisture level is probably the most challenging aspect of extending the existing model, other models accounting for water retention in different types of materials could be utilised.

The use of very coarse and open graded materials should be more restricted. Currently a typical subbase layer is constructed of open graded 20/120 mm crushed rock material. If the layer thickness is sufficient, natural air convection may be initiated. A small reduction in the minimum size could reduce permeability to a level at which natural air convection does not pose a significant risk and mechanical properties are not compromised. The current regulations also allow the use of open graded frost protection layers with a particle size of up to 500 mm. The requirements for material particle size distribution should be more limited to have dense graded materials. This would not only eliminate the possibility of air convection but also improve frost protection properties, with higher water retention and latent heat of fusion.

The investigation of the intrinsic permeability of coarse materials could be extended. Current knowledge shows that existing theoretical models give estimations differing by up to one degree of magnitude for very coarse materials. More experiments could be conducted with different sizes and shapes of coarse materials to derive a more appropriate model for the estimation of intrinsic permeability.

6 References

Argo, W., & Smith, J. (1953). Heat transfer in packed beds-prediction of radial rates in gas-solid beds. *Chemical Engineering Progress, 49*(8), 443-451.

Balland, V., & Arp, P. A. (2005). Modeling soil thermal conductivities over a wide range of conditions. *Journal of Environmental Engineering and Science, 4*(6), 549-558. doi:10.1139/s05-007

Birch, A. F., & Clark, H. (1940). The thermal conductivity of rocks and its dependence upon temperature and composition. *American Journal of Science, 238*(8), 529-558.

Chapuis, R. P. (2004). Predicting the saturated hydraulic conductivity of sand and gravel using effective diameter and void ratio. *Canadian Geotechnical Journal, 41*(5), 787-795. doi:10.1139/t04-022

Côté, J., Fillion, M.-H., & Konrad, J.-M. (2011). Intrinsic permeability of materials ranging from sand to rock-fill using natural air convection tests. In *Canadian Geotechnical Journal* (Vol. 48, pp. 679-690).

Côté, J., & Konrad, J.-M. (2005a). Thermal conductivity of base-course materials. *Canadian Geotechnical Journal, 42*(1), 61-78.

Côté, J., & Konrad, J.-M. (2005b). A generalized thermal conductivity model for soils and construction materials. *Canadian Geotechnical Journal, 42*(2), 443-458.

Côté, J., & Konrad, J.-M. (2009). Assessment of structure effects on the thermal conductivity of two-phase porous geomaterials. *International Journal of Heat and Mass Transfer, 52*(3-4), 796-804. doi:10.1016/j.ijheatmasstransfer.2008.07.037

De Vries, D. A. (1963). Thermal properties of soils. *Physics of plant environment*.

Dhyser, Y. (2013). Analyse numérique de résultats expérimentaux dans le but d'établir la perméabilité intrinsèque de matériaux d'enrochement. *Master Thesis. Laval University*.

Dudgeon, C. R. (1966). An experimental study of the flow of water through coarse granular media. *La Houille Blanche*(7), 785-801. doi:10.1051/lhb/1966049

Farouki, O. T. (1981). Thermal properties of soils. *US Army Corps of Engineering, Cold Regions Research and Engineering Laboratory, Hanover, NH, CRREL Monograph 81-1.*

Fillion, M. H., Côté, J., & Konrad, J. M. (2011). Thermal radiation and conduction properties of materials ranging from sand to rock-fill. *Canadian Geotechnical Journal, 48*(4), 532-542. doi:10.1139/t10-093

Fladvad, M., Aurstad, J., & Wigum, B. J. (2017). A survay comparing practices for use of aggreates in road construction. *Tenth international conference on the bearng capacity of roads, railways and airfields*.

Goering, D. J. (1998). *Experimental investigation of air convection embankments for permafrost-resistant roadway design.* Paper presented at the Seventh International Conference on Permafrost. Collection Nordicana.

Goering, D. J., Instanes, A., & Knudsen, S. (2000). Convective heat transfer in railway embankment ballast. *Ground freezing*, 31-36.

Goering, D. J., & Kumar, P. (1999). Permeability effects on winter-time natural convection in gravel embankments. *Advances in Cold-Region Thermal Engineering and Sciences. Springer Berlin Heidelberg, 1999*, 455-464.

Handbook N200. (2014). Vegbygging (Road construction). Statens vegvesens håndbokserie. Norway.

Heiersted, R. S. (1976). *Sikring mot teleskader*: Norges teknisk-naturvitenskapelige forskningsråd og Statens vegvesens utvalg for frost i jord.

Horai, K. i. (1971). Thermal conductivity of rock-forming minerals. *Journal of geophysical research, 76*(5), 1278-1308.

Horton, C., & Rogers, F. (1945). Convection currents in a porous medium. *Journal of applied physics, 16*(6), 367-370.

Howell, J. R., Menguc, M. P., & Siegel, R. (2010). *Thermal radiation heat transfer*: CRC press.

Johansen, O. (1975). Thermal conductivity of soils. *Ph.D. Thesis. University of Trondheim, Trondheim, Norway. US Army Corps of Engineering, Cold Regions Research and Engineering Laboratory, Hanover. N.H. CRREL Draft English Translation 637*, 291.

Johansen, O., Frivik, P. E., Pedersen, K. B., & Bjerkan, O. (1976). Varmeteksniske egenskaper av jord og bygningsmaterialer. *Sikring Mot Teleskader, Frost I Jord, 17*, 71-121.

Kaviany, M. (1999). Principles of heat transfer in porous media. 2nd ed. *Springer-Verlag, New York*.

Kersten, M. S. (1949). Laboratory research for the determination of the thermal properties of soils. *Research Laboratory Investigation, Engineering Experiment Station, University of Minnesota, Minneapolis, Minn. Technical report*.

Kozeny, J. (1927). Ueber kapillare Leitung des Wassers im Boden. *Sitzungsberichte Wiener Akademie, 136(2a)*, 271–306.

Lapwood, E. (1948). *Convection of a fluid in a porous medium.* Paper presented at the Mathematical Proceedings of the Cambridge Philosophical Society.

Lu, S., Ren, T., Gong, Y., & Horton, R. (2007). An Improved model for predicting soil thermal conductivity from water content at room temperature. *Soil Science Society of America Journal, 71*(1). doi:10.2136/sssaj2006.0041

Mickley, A. (1951). The thermal conductivity of moist soil. *Transactions of the American Institute of Electrical Engineers, 70*(2), 1789-1797.

NGI. (1996a). Måling av varmeledningsevne i springstein. Ufrosset varmeledningstall for stein i fraksjon 20-250 mm., jordfuktig tilstand. In *Norges Geotekniske Institutt (Norwegian Geotechnical Institute)* (pp. 20).

NGI. (1996b). Måling av varmeledningsevne i springstein. Ufrosset varmeledningstall for stein i fraksjon 20-250 mm. In *Norges Geotekniske Institutt (Norwegian Geotechnical Institute)* (pp. 20).

NGI. (1996c). Måling av varmeledningsevne i springstein. Ufrosset varmeledningstall for stein i fraksjon 0-100 mm og 0-250 mm. In *Norges Geotekniske Institutt (Norwegian Geotechnical Institute)* (pp. 16).

NGI. (1999). Måling av varmetap i ulike steinfyllingsfraksjoner. Måling av varmetap i ballastpukk, maskinkult og sprengstein. *Norges Geotekniske Institutt (Norwegian Geotechnical Institute)*, 35, (In Norwegian).

Nield, D. A., & Bejan, A. (2013). *Convection in porous media*: Springer.

Poiseuille, J. L. (1844). *Recherches expérimentales sur le mouvement des liquides dans les tubes de très-petits diamètres*: Imprimerie Royale.

Rieksts, K., Hoff, I., Kuznetsova, E., & Côté, J. (2017). Laboratory investigations on heat transfer of coarse crushed rock materials. *70th Canadian Geotechnical Conference*.

Rieksts, K., Hoff, I., Scibilia, E., & Côté, J. (2018). Establishment of intrinsic permeability of coarse open graded materials – a review and analysis of existing data from natural air convection tests (to be submitted in 2018).

Rothery, K., & Mellor, S. (2006). Crushing and screening. *The Institute of Quarrying*, 268.

Sass, J., Lachenbruch, A. H., & Munroe, R. J. (1971). Thermal conductivity of rocks from measurements on fragments and its application to heat-flow determinations. *Journal of geophysical research, 76*(14), 3391-3401.

Schubert, G., & Straus, J. M. (1979). Three-dimensional and multicellular steady and unsteady convection in fluid-saturated porous media at high Rayleigh numbers. *Journal of Fluid Mechanics, 94.01*, 25-38.

Seehusen, J. (2011). Flytoget må kjøre i 80. *Available at: https://www.tu.no/artikler/flytoget-ma-kjore-i-80/238210 [Accessed 21.03.2018]*.

Smith, W. O. (1942). The thermal conductivity of dry soil. *Soil Science, 53*(6), 435-460.

Tien, C. L. (1988). Thermal radiation in packed and fluidized beds. *Journal of Heat transfer, 110.4b*, 1230-1242.

Tunmo, T. (2010). Ny motorvei ødelagt for alltid. *Available at: https://www.tu.no/artikler/ny-motorvei-odelagt-for-alltid/238209 [Accessed 21.03.2018]*.

Woodside, W., & Messmer, J. (1961). Thermal conductivity of porous media. I. Unconsolidated sands. *Journal of applied physics, 32*(9), 1688-1699.

Xue, S. C., Poladian, L., Barton, G. W., & Large, M. C. J. (2007). Radiative heat transfer in preforms for microstructured optical fibres. *International Journal of Heat and Mass Transfer, 50*(7-8), 1569-1576. doi:10.1016/j.ijheatmasstransfer.2006.08.027

APPENDIX – THE PAPERS

Appendix A – Paper I

PAPER I

This appendix includes the following paper submitted to the Cold Regions Science and Technology.

Rieksts, K., Hoff, I., Scibilia, E. and Côté, J., 2018. *Establishment of intrinsic permeability of coarse open graded materials – a review and analysis of existing data from natural air convection tests.*

Is not included due to copyright

Appendix B – Paper II

This appendix includes the following paper submitted and presented at the 70th Canadian Geotechnical Conference and the 12th Joint CGS/IAH-CNC Groundwater Conference.

PAPER II

Rieksts, K., Hoff, I., Kuznetsova, E. and Côté, J., 2017. *Laboratory investigations on heat transfer of coarse crushed rock materials.* GeoOttawa 2017, the 70th Canadian Geotechnical Conference and the 12th Joint CGS/IAH-CNC Groundwater Conference.

Laboratory investigations on heat transfer of coarse crushed rock materials

K. Rieksts, I. Hoff, E. Kuznetsova
Norwegian University of Science and Technology, Trondheim, Norway
J. Côté
Laval University, Quebec city, Canada

ABSTRACT

Design requirements for roads and railways in Norway allow the use of coarse open graded materials. For such materials, apart from the thermal conduction, natural air convection can yield a significant contribution to the overall heat transfer. This paper presents a laboratory study dealing with air convection tests for coarse materials. In addition, the tests serve as a good basis for defining the intrinsic permeability of these materials within a heat transfer cell with an inner volume of $1m^3$. One sample was prepared of natural cobbles with particle size ranging from 0.09 to 0.21 m and the corresponding d_{10} value of 0.12 m. The sample was tested under three temperature gradients for upward and downward heat flow. As expected, the experimental results show that for a given thermal gradient, the heat flux is larger for upward heat flux compared to downward heat flow. The analysis results yielded an average value of intrinsic permeability of 3.5×10^{-6} m^2. This value is within the limits of intrinsic permeability of similar study performed with materials with similar particle size distribution. In addition, the results have a reasonably good agreement with values calculated by Kozeny-Carman and Chapius equations. This study serves as a validation for the test setup and the project will continue with measurements of air convection for crushed rock materials.

Les exigences de conception pour les routes et Chemins de fer en Norvège permettent l'utilisation de matériaux grossiers à porométrie ouverte. Pour de tels matériaux, hormis la conduction thermique, la convection naturelle peut contribuer significativement aux échanges de chaleur. Cet article présente une étude en laboratoire de la convection naturelle pour des matériaux grossiers. De plus, les essais permettent d'établir la perméabilité intrinsèque de ces matériaux à l'intérieur d'une cellule de transfert thermique de 1 m^3. Un échantillon de cailloux naturels a été préparé avec des dimensions de particules variant de 0,09 m à 0,21 m et un diamètre effectif d_{10} de 0,12 m. L'échantillon a été testé selon trois gradients thermiques pour des écoulements de chaleur descendant et ascendant, respectivement. Tel qu'anticipé, les résultats expérimentaux montrent que pour une gradient thermique donné, le flux de chaleur des essais ascendant est supérieur au flux de chaleur des essais descendant. Les résultats d'analyse ont donné une perméabilité intrinsèque de $3,5 \times 10^{-6}$ m^2. Cette valeur est comprise à l'intérieure des limites de perméabilité intrinsèque d'étude antérieures sur des matériaux similaires. De plus, les résultats sont raisonnablement en accord les valeurs calculées avec les modèles de Kozeny-Carman et de Chapuis. Cette étude sert de validation de la cellule expérimentale et le projet se continuera avec des essais sur des matériaux de roc concassé.

1 INTRODUCTION

Road and railway structures build in cold regions typically have thicker unbound material layers (Fladvad et al., 2017). This is a design requirement to minimize frost penetration depth when constructing on top of frost susceptible soils. These thick layers allow the use of coarser materials. This is beneficial in terms of decreased production costs. However, the lack of control over material gradation might have an adverse effect on the material thermal properties and resistance to frost penetration.

Thermal conductivity is the governing heat transfer mechanism (Farouki, 1981; Johansen, 1975) for most of the mineral materials. However, coarse open graded materials can have other heat transfer modes that can significantly contribute to the overall heat transfer rate. These are radiation and natural convection that can be present for coarse open graded materials (Nield & Bejan, 2013) As a result frost penetration levels can be higher than anticipated.

The literature provides very limited amount of laboratory studies that characterize coarse mineral materials with particle size up to 200 mm (Côté et al., 2011; Goering et al., 2000; Johansen, 1975). This paper presents experimental results performed with large scale heat transfer box.

This study is a part of a larger research project on frost protection of roads and railways (Kuznetsova et al., 2017) and has a main goal to investigate thermal properties of crushed rock material. The study includes two parts: small scale (Rieksts et al., 2017) and large scale experiments. Study presented in this paper mostly serves as a validation basis for the test setup used in these experiments. Upon successful validation, the research is expected to move on to the next phase where coarse crushed rock materials will be tested.

2 METHODS

Figure 1 summarizes various heat transfer types for unbound mineral materials as a function of effective particle diameter and degree of saturation (Côté et al., 2011). Conduction (1) is the governing heat transfer mode for most of the domain. For fine grained soils with low degree of saturation, temperature driven (2) and humidity

driven (3) vapor diffusion can yield a significant contribution to heat transfer rate. For coarse open graded materials with high degree of saturation free water convection (4) can become the governing heat transfer mode. Finally, for coarse materials with low degree of saturation, free air convection (5) and radiation (6) can become the predominant heat transfer mechanism. Mode 2, 3 and 4 could be relevant for soils/materials below the pavement structure. For materials used in Norwegian road construction only mode 1, 5 and 6 are relevant and the main scope of this study.

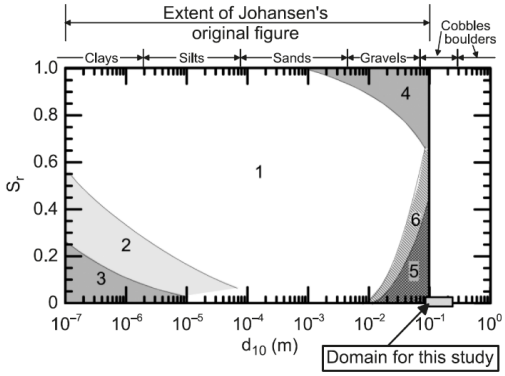

Figure 1. Heat transfer mode in soils (redrawn and adapted from Johansen (1975) (Côté et al., 2011). See text for description of numbers.

2.1 Radiant heat transfer in porous media

Radiant heat transfer in porous media is a very complex heat transfer mechanisms and challenging to solve mathematically. However, in such geometry as porous media, where particles are affected only by their neighboring ones, radiation can be assumed as diffusion process (Xue et al., 2007). Radiation can have a significant contribution to the overall heat transfer rate when material contains large pores. When the distance between two adjacent particles is increased, so is the temperature difference between them. As a result, the interparticle radiation will increase substantially. In addition, radiation flows in the same direction as conduction, hence it can be assessed in the form of Fourier's law of thermal conductivity through diffusion approximation.

Because of this, effective thermal conductivity (k_e) can be defined as a sum of thermal conductivity (k_c) and equivalent radiant conductivity (k_r). This approach greatly simplifies calculations for conditions where radiant heat transfer is involved.

$$k_e = k_c + k_r \quad [1]$$

In diffusion approximation equivalent radiant conductivity can be approximated by Eq. 2 as stated by Tien (1988):

$$k_r = 4Ed_{10}\sigma T^3 \quad [2]$$

where E is an exchange factor, σ is the Stephan-Boltzmann constant and T is the mean temperature.

The contribution of radiant conductivity can be easier observed for downward heat flow conditions (summer conditions). In this case, the heat transfer is limited only to two heat transfer modes, namely thermal conductivity and radiation. To be able to estimate the contribution of each of them, apart from the diffusion approximation also a thermal conductivity model is necessary. The literature provides numerous models for estimation of dry thermal conductivity for mineral materials. For this research a model developed by Côté and Konrad (2009) will be used:

$$k_c = \frac{(\kappa_{2p}k_s - k_f)(1-n) + k_f}{1 + (k_{2p} - 1)(1-n)} \quad [3]$$

where n is porosity and k_s and k_f is the thermal conductivity of solid and fluid (air) phase, respectively and κ_{2p} is a structure parameter and is defined by Eq. [4]:

$$\kappa_{2p} = 0.29\left(15\frac{k_f}{k_s}\right)^{\varphi} \quad [4]$$

where φ is an empirical parameter accounting for structure. For natural unbound mineral materials when ratio of k_f/k_s is lower than 1/15 factor φ is 0.81.

2.2 Convective heat transfer in porous media

Free air convection in porous materials is buoyancy driven, meaning that fluid flow is driven by the changes in density. Convective heat transfer represents the winter conditions for road and railway structures when the ground temperature is still warm while the air temperature is significantly lower. The warmer air in the ground has lower density, hence it moves upwards, while the colder, more dense air, moves downwards.

Free convection in porous media is a complex heat transfer mechanisms depending on numerous factors. The magnitude of convective heat transfer can be expressed by Rayleigh number as stated by Nield and Bejan (2013):

$$Ra = \frac{g\beta CKH^2\nabla T}{\nu k_e} \quad [5]$$

where g is the gravitational acceleration, H is the height of the sample, ∇T is the temperature gradient, K is the intrinsic permeability and β, C and ν is the thermal expansion, heat capacity and kinematic viscosity of the fluid (air), respectively. For laboratory conditions when air convection roll is restricted to square enclosure, the critical Rayleigh number for initiation of convective motion is $4\pi^2$ (~40). Convective heat transfer is initiated only if Ra number exceeds the critical value.

While the calculation of Rayleigh number for field conditions requires numerous input parameters, most of them can be approximated fairly precisely. However, estimation of intrinsic permeability for coarse materials can be complicated and results can experience large deviations. Such methods involving liquids for determination of intrinsic permeability can be applied only for fine materials. For coarse open graded materials turbulent flow forms at small hydraulic gradients. As a

result Darcy's law cannot be applied in such cases. Large scale air-convection tests can serve as an appropriate alternative for determination of this important parameter.

The increase in heat transfer for upward heat flux compared to downward flow can be expressed with the Nusselt (Nu) number. The Nusselt number is the ratio between upward and downward heat flux under the same steady state temperature gradient:

$$Nu = \frac{q\uparrow}{q\downarrow} \quad [6]$$

Schuber and Straus (1979) defined a relationship between Nu and Ra numbers for free air convection in a square enclosure, heated from below. Côté et al. (2011) derived an empirical relationship from their work:

$$Nu = 1.735\ ln(Ra) - 5.38 \quad [7]$$

This relationship is depicted in Figure 2 together with experimental data from three-dimensional heat transfer cells (Combarnous & Bories, 1975; Elder, 1967; Kaneko et al., 1974; Yen, 1974).

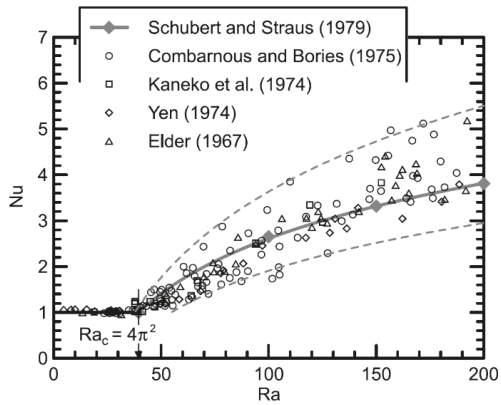

Figure 2. Experimental and analytical Nu-Ra number relationship for porous media in a square enclosure, heated from below (Côté et al., 2011)

As can be seen in Figure 2, relationship experimental data fit reasonably well with experimental data obtained from various laboratory experiments. Empirical Nu-Ra relationship can be used in conjunction with experimental data of natural convection for calculation of intrinsic permeability that is one of the key parameters for approximating convective air flow for road construction materials.

3 MATERIALS

For this phase of the research project natural cobbles were selected as the test material. The cobbles were collected from a natural gravel pit in Sør-Trondelag in Norway. Material was washed clean from the fines and measurements of weights was taken for each of the cobbles prior to placing them in a test setup (see Figure 3). Material was placed dry in the test box. The main purpose of this phase was to validate the equipment against previous tests found in the literature.

Figure 3. Test sample in preparation phase (inner size of the box 1x1m).

Measurements of density was performed according to NS-EN 1097-6 annex B. The average density of the rocks was measured as 2.64 g/cm^3. The weight measurements and rock density was used to establish an equivalent sphere-size gradation as showed in Figure 4. For this test, a total of 433 cobbles were used to fill the test box. Particle size varied from 0.09 to 0.21 m. The total weight of the test sample was 1616.6 kg. The corresponding dry density (ρ_d) and porosity (n) are 1.68 g/cm^3 and 0.36, respectively. The effective particle diameter (d_{10}) is 0.12 m.

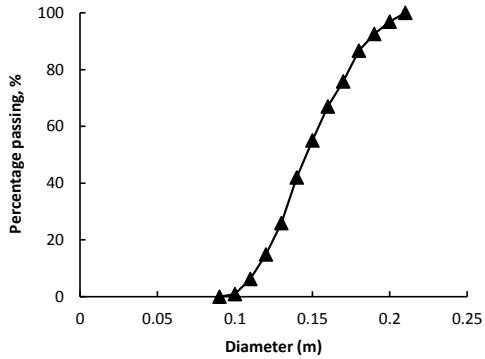

Figure 4. Equivalent sphere-size distribution of test sample.

4 EXPERIMENTAL PROCEDURE

The test setup comprises of a thermally insulated box with the inner volume of 1 m^3 (see Figure 5), as adapted from previous studies of Goering et al. (2000) and from Côté et al. (2011) The walls are made of extruded polystyrene

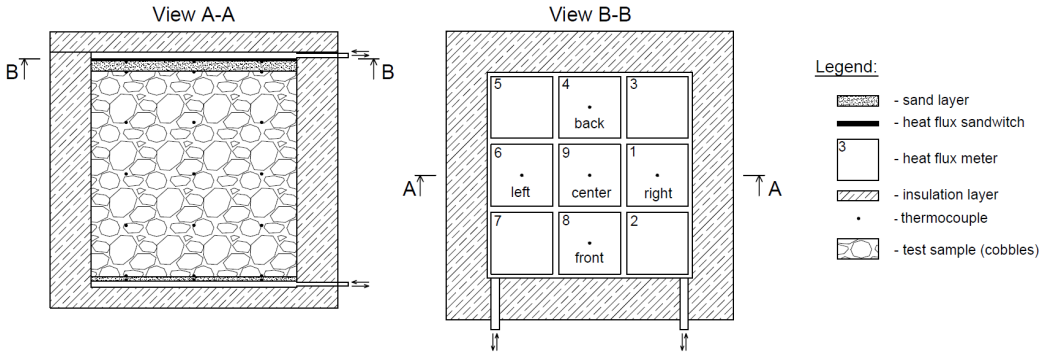

Figure 5. Experimental test setup: A-A vertical cross-sectional view; B-B horizontal cross-sectional view at heat flux sensor level.

boards with the total thickness of 0.3 m (k=0.03 W/mK). The box is equipped with two independent heat exchange plates that are placed below and on top of the sample. The plates consist of a double steel tube circuit placed between two steel sheets. The voids between the tubing are filled with fine sand to ensure sufficient thermal contact. The plates are attached to cryostat units that are able to provide desired temperature gradients between 7 and 20 °C/m.

A sand layer, with a thickness of approximately 2 cm is placed at the bottom of the sample. This minimizes the heat resistance from the heat exchange plate to the cobbles. For the top part, a geotextile is laid over the cobbles and a 5 cm thick sand layer is placed on top of it to ensure good heat transfer to the overlaying heat exchange plate.

To monitor the temperature profiles, altogether 30 thermocouples are positioned within the test sample. They are placed in layers by five. In each layer one thermocouple is positioned in the center while the other four are placed 0.17 m from each of the face. The locations of thermocouples are illustrated in Figure 5 with vertical (A-A) and horizontal (B-B) cross-sectional view.

To observe the upward and downward energy flow, heat flux sensors with dimensions of 0.3x0.3 m are placed in the top part of the sample. A sandwich type plate (see Figure 6) where heat flux sensors are placed between two Plexiglas® sheets is laid between top sand layer and heat exchange plate.

Figure 6. Heat flux sensors placed at the top of the sample.

The test is run in two phases. First, a downward heat flow is imposed. In this case, the heat transfer is restricted only to conduction and radiation (effective thermal conductivity). To minimize the influence from the ambient temperature outside the box, the average temperature of the test sample is kept as close as possible to the room temperature (around 22°C). This means that the temperatures of heat exchange plates are set are equally above and below room temperature. At the same time the temperature in the middle section of the test stays around 22°C. For the downward heat flow phase, three temperature gradients were used.

Secondly, an upward heat flow is imposed for the second phase of the test. In this phase, in addition to conduction and radiation, convective heat transfer may be initiated. In an attempt to impose convective heat transfer in desired direction (from face to face), a heating cable was placed in one of the bottom edges. The line heat source was used prior to switching on the heat exchange elements. It was expected that a line heat source would initiate convection in desired direction and it would maintain the same motion when the heat exchange elements are used. For the upward heat transfer phase three temperature gradients were used gradually increasing the heat flux throughout the sample.

5 RESULTS AND DISCUSSION

Figure 7 shows the temperature gradients for all three downward steady state conditions. For each consequent test step the temperature gradient was gradually increased. Each of the line is an average of five temperature gradients measured in vertical direction. It can be seen that an almost linear temperature gradient is obtained throughout the cobbles. It is in agreement with the theory that for a downward heat flow only conduction and radiation are the active heat transfer modes. This means that the temperature gradient is linear and the heat flux rate constant.

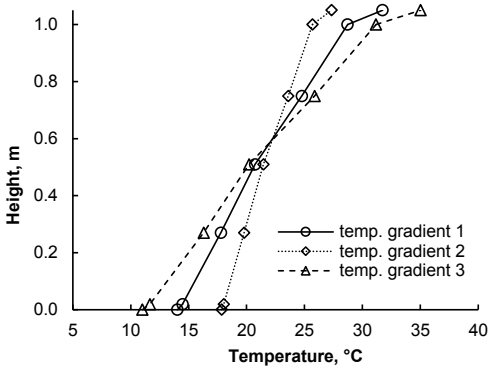

Figure 7. Temperature gradients for downward steady state conditions.

5.1 Radiant heat transfer in porous media.

The contribution of radiation in cobbles can be evaluated using the theory described in section 2. In addition, when comparing the temperature gradient in cobbles with that in upper sand layer, it gives a clear picture of radiant heat transfer as explained below.

Results for downward heat flow are summarized in Table 1. The corresponding temperature gradient (∇T), heat flux (q↓) and effective thermal conductivity is given for the cobbles section. The average measured thermal conductivity for the upper sand layer is 0.22 W/m°C. It has to be mention here that for preliminary validation experiment on pure sand, a thermal conductivity value of 0.46 W/m°C was obtained which was in agreement with values found in the literature for similar materials. It is assumed that the value of 0.46 W/m°C is more realistic than the value of 0.22 W/m°C. The low value of thermal conductivity is most likely caused by the layer of geotextile placed before the sand layer. The layer of geotextile is working as a thermal resistance that is not taken into account here. In addition, although the sand layer was 5 cm it was probably insufficient to provide accurate temperature gradient measurements. The positions of thermocouples could easily vary by ± 5 mm resulting in an error of 10%.

Table 1 give the experimental results of effective thermal conductivity computed from three different imposed thermal gradients within the sample. An average value of 0.91 W/m°C is obtained.

Table 1. Results for downward heat flow.

	∇T (°C/m)	q↓ (W/m^2)	k_e (W/m°C)
1	7.8	6.8	0.89
2	14.5	13.3	0.93
3	19.9	17.7	0.90

Using Eq.(2) to calculate radiant conductivity yields a value of 0.54 W/m°C while Eq.(3) for thermal conductivity component results in 0.44 W/m°C. Both of these components together form the effective thermal conductivity as described before. The sum of these values results in 0.98 W/m°C. This theoretical value has a reasonable agreement with the experimentally measured value of 0.91 W/m°C. Based on these results it is possible to conclude the significant contribution of radiation for downward heat flow. For the studied material, the overall heat transfer increased by a factor of two compared to conduction alone due to the contribution of radiation.

Another validation for radiant conduction is when temperature gradient of cobbles is compared to that of the upper sand layer. Although both materials have similar porosity, thermal gradients are very different. Since the radiant conductivity is giving a significant contribution to heat transfer in cobbles, the temperature gradient in the cobbles in much lower than in sand layer. Another validation for this is when Eq.(2) is applied for the sand material in order to approximate the contribution of radiant conductivity. The resulting value of radiant conductivity is hardly larger than zero W/m°C. The same trend cannot be observed for the bottom sand layer, because of the thin sand layer that introduces substantial inaccuracies. The thermocouples were taped at the bottom of the cobbles. Due to the overlaying pressure it is assumed that the cobbles sank in the sand layer. This resulted in decreased distance between the first two layers of thermocouples. Therefore, the calculated temperature gradient in the bottom sand layer is biased.

5.2 Convective heat transfer in porous media.

A typical result for upward heat motion is depicted in Figure 8. Due to the presence of connective heat transfer each of the temperature gradient has to be showed separately.

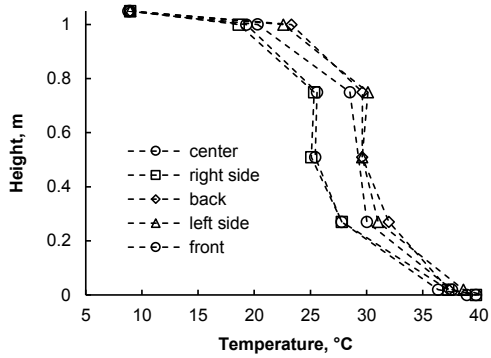

Figure 8. Temperature gradients at steady state for upward heat flow conditions.

Based on the temperature gradients and heat flux readings it could be observed that the air convection instead from face to face was from corner to corner. The upward heat flow was in one corner, while the downward air movement was in the diagonal corner. Thus, the heat

flux sensor no. 2 was yielding the lowest values while no 5. was giving the highest values. All the other values were intermediate with a trend of decreasing values from one corner to the other. A typical experimental result for heat flux meter reading is showed in Figure 9. The numbers of each heat flux meter are in the upper left corner while the corresponding heat flux values in W/m^2 are in the center of each heat flux meter.

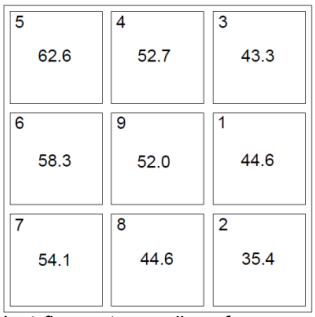

Figure 9. Heat flux meter readings for upward heat flow condition.

As mentioned before, a line heat source was used to impose the convective air motion in desired direction from face to face. Unluckily, the heat source turned out to be too weak for a proper initiation of convective air motion. As a result, air convection was freely initiated and took a non controlled path.

When comparing the temperature gradients for upward heat flow with those from downward, several aspects can be observed that confirm the presence of air convection. Firstly, the temperature gradients are shifted compared to each other. This is due to the motion of warm and cold air. The temperatures on the side of upward air movement are higher than those where the cold air is descending. Secondly, the curved shape of the temperature gradient is another confirmation for convection. Isotherms tends to be pushed closer together in the end parts while being separated in the center section.

A summary of the results for upward heat flow for cobbles is showed in Table 2. Values for temperature gradient and heat flux are the average values at the top and the bottom part of cobbles.

Table 2. Results for upward heat flow.

	∇T (°C/m)	q↑ (W/m^2)
1	7.0	14.0
2	14.1	39.2
3	17.0	49.7

Figure 10 shows a comparison of upward and downward heat transfer extent. The heat flux is showed as a function of temperature gradient. A clear difference can be seen for the contribution of convective heat transfer. The downward heat flow includes only the components of thermal and radiant conductivity. The upward heat flow in addition to those contain also the contribution of air convection. As showed, the free air movement is initiated when the temperature gradient exceeds about 4 °C/m. Up to this value the upward heat flow do not contain a convective heat transfer component. For large temperature gradients, convective air motion can become the dominant heat transfer mode and overrun effective thermal conductivity several-fold.

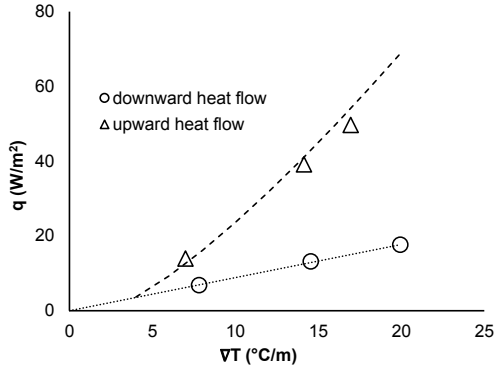

Figure 10. Experimental data points for downward and upward heat flow steady state conditions.

5.3 Intrinsic permeability

Although the convective air motion was not a square enclosure, an attempt was made to apply the existing Nu-Ra number relationship to back-calculate the value for the intrinsic permeability. Figure 11 shows the experimentally defined Nu number values with the corresponding Ra values obtained using the Eq.(7). Obtained Ra values are well within the recommended range below 300 for laminar or Darcian flow conditions (Wang & Bejan, 1987).

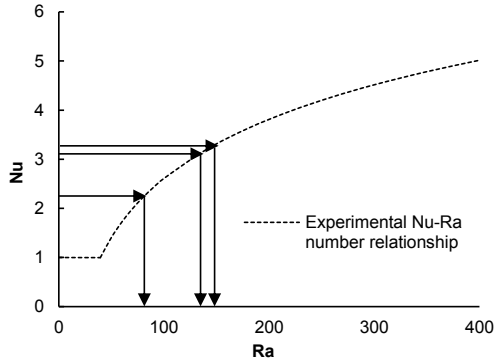

Figure 11. Experimental Nu-Ra number relationship

By having the corresponding Ra number values it is now possible to use Eq.(5) to back-calculated the intrinsic permeability. The values for β, C and ν for laboratory conditions are taken as 0.00343 K^{-1}, 1211 Jm^{-3}K^{-1} and 0.000015 m^2/s, respectively. The height of the experiment is set to 1 m and the gravitational acceleration is 9.81 m/s^2.

The value of effective thermal conductivity is taken as the average value form all three downward heat flow experiments and is calculated as 0.91 W/m°C. The value of temperature gradient is set according to the test conditions.

The summary of calculated values is given in Table 3. Nusselt values are calculated as the ratio of upward and downward heat flow at the same magnitude of temperature gradient. The corresponding values of intrinsic permeability is calculated using the empirical Nu-Ra number relationship. The average K is 3.51×10^{-6} m^2.

Table 3. Calculated values using Nu-Ra number relationship.

	Nu	Ra	∇T (°C/m)	K (10^{-6} m^2)
1	2.25	81	7.0	4.11
2	3.11	133	14.1	3.34
3	3.28	147	17.0	3.08

In order to validate the K values obtained in this paper, it can be useful to compare those to existing data from literature or to predictions from actual permeability models. Many empirical equations exist for estimation of intrinsic permeability. However, most of them have been developed on the basis of fine soils. Therefore, one should be careful when such equations are applied for much coarser materials as the characteristics of coarse materials can be different in many ways.

One of the most common equations used for determination of permeability for sands is Kozeny-Carman (Kozeny, 1927) equation expressed in Eq. 8:

$$K = \frac{C}{f^2} d_{10}^2 \frac{n^3}{(1-n)^2} \quad [8]$$

Here the ratio C/f^2, which accounts for tortuosity as well as pore and particle shape, is set to 0.0056. This is a value for arrangements of uniformly sized spheres.

Kozeny-Carman equation have been later modified by Chapuis (2004). He established his equation on the basis of hydraulic conductivity of sand. Converting his equation to intrinsic permeability gives:

$$K = A\left(d_{10}^2 \frac{n^3}{(1-n)^2}\right)^{\beta} \quad [9]$$

The values of coefficients A and β were estimated as 1.25×10^{-4} and 0.7825, respectively.

The values of intrinsic permeability are compared to the ones obtained from a study by Côté et al. (2011) who tested similar materials. They also analyzed previous tests by Johansen (1975) who performed convection tests but could not back-calculate the K value because no analytical solutions such as that from Shubert and Strauss (1979) existed at the time of his study. The corresponding comparison is showed in Figure 12. It can be observed that the average K value from this study fits well within the range of similar materials tested in other studies.

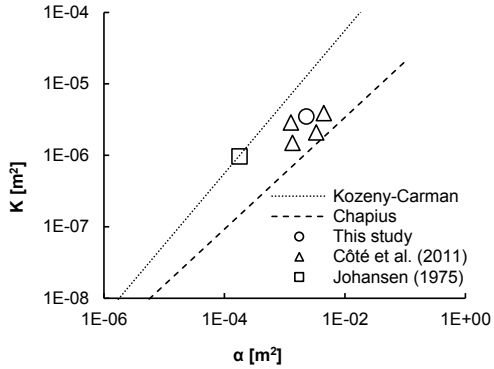

Figure 12. Measured and predicted K-α relationship.

To highlight the importance of effective particle size on intrinsic permeability of unbound materials, K values are plotted versus d_{10}^2 in Figure 13. The data are plotted together with those obtained from preceding studies by Johansen (1975) and Côté et al. (2011). The results show a clear trend that intrinsic permeability increases with increased d_{10}. This confirms the fact that effective particle diameter can serve as a good characterization of material pore space. With increasing d_{10} values the intrinsic permeability increases, which could result in initiation of convective heat transfer.

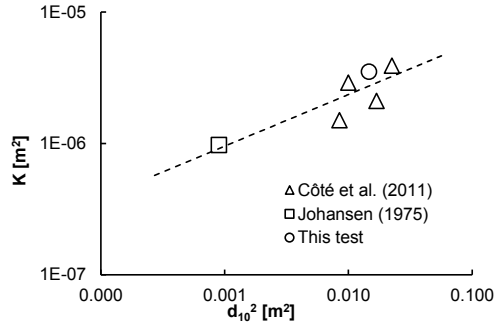

Figure 13. Influence of effective particle size on intrinsic permeability.

6 CONCLUSION

Heat transfer characteristics for a sample of highly porous and coarse material have been established using a 1 m^3 large scale laboratory equipment.

Laboratory experiments show the significant increase in the rate of heat transfer due to contribution of radiant and convective heat transfer. Radiation in the pores of opaque particulate media can be approximated as diffusion process. In that sense, radiant conductivity is added to thermal conductivity together forming effective thermal conductivity. The test results show that the effective thermal conductivity is 0.91 W/m°C. The value for pure conduction only is about half this value. This means that for

this material, radiation only can increase the rate of heat transfer by a factor of two.

Convective heat transfer is representing winter conditions when energy is extracted from the ground. Results for the studied material show that free air motion is initiated when the temperature gradient exceeds 4 °C/m. For higher temperature gradients, convective heat transfer can exceed that of conduction and radiation several-fold. Neglecting the contribution of radiation and convection when frost design is carried out might lead to significantly underestimated frost penetration depths.

While the large scale experiments can give a good characterization for coarse material heat transfer mechanisms it also serves well for the characterization of intrinsic permeability of coarse porous materials. Conventional methods for measuring permeability, such as those involving liquids, cannot be applied to these coarse materials as the turbulent flows would form at small hydraulic gradients invalidating Darcy's law usually used to establish permeability. Large scale air convection tests provide good insight into this crucial parameter. Using the Nu-Ra relationship in a closed square enclosure, it is possible to back-calculate intrinsic permeability from experimental convection heat transfer. The tests results fit well with results from other preceding studies and compare well to predictions of existing permeability models.

The outcome if this phase of the research gives confirmation on the validity of test equipment. The ongoing research will be continued with natural convection tests on crushed rock materials used in road construction and artificial insulation materials.

7 ACKNOWLEDGEMENTS

This research was supported by the Norwegian Research Council (NRC) under grant 246826/O70.

Authors wish to acknowledge the technical assistance of Lisbeth Johansen, Bent Lervik and Jan Erik Molde from Department of Civil and Environmental Engineering, Norwegian University of Science and Technology.

8 REFERENCES

Chapuis, R. P. (2004). Predicting the saturated hydraulic conductivity of sand and gravel using effective diameter and void ratio. *Canadian Geotechnical Journal, 41*(5), 787-795. doi:10.1139/t04-022

Combarnous, M. A., & Bories, S. A. (1975). Hydrothermal convection in saturated porous media. *Advances in hydroscience, 10*, 231-307.

Côté, J., Fillion, M. H., & Konrad, J. M. (2011). Intrinsic permeability of materials ranging from sand to rock-fill using natural air convection tests. *Canadian Geotechnical Journal, 48*(5), 679-690. doi:10.1139/t10-097

Côté, J., & Konrad, J.-M. (2009). Assessment of structure effects on the thermal conductivity of two-phase porous geomaterials. *International Journal of Heat and Mass Transfer, 52*(3-4), 796-804. doi:10.1016/j.ijheatmasstransfer.2008.07.037

Elder, J. W. (1967). Steady free convection in a porous medium heated from below. *Journal of Fluid Mechanics, 27*(01), 29-48.

Farouki, O. T. (1981). Thermal properties of soils. *US Army Corps of Engineering, Cold Regions Research and Engineering Laboratory, Hanover, NH, CRREL Monograph 81-1.*

Fladvad, M., Aurstad, J., & Wigum, B. J. (2017). A survay comparing practices for use of aggreates in road construction. *Tenth international conference on the bearng capacity of roads, railways and airfields*.

Goering, D. J., Instanes, A., & Knudsen, S. (2000). Convective heat transfer in railway embankment ballast. *Ground freezing*, 31-36.

Johansen, O. (1975). Thermal conductivity of soils. *Ph.D. Thesis. University of Trondheim, Trondheim, Norway. US Army Corps of Engineering, Cold Regions Research and Engineering Laboratory, Hanover. N.H. CRREL Draft English Translation 637*, 291.

Kaneko, T., Mohtadi, M., & Aziz, K. (1974). An experimental study of natural convection in inclined porous media. *International Journal of Heat and Mass Transfer, 17*(4), 485-496.

Kozeny, J. (1927). Ueber kapillare Leitung des Wassers im Boden. *Sitzungsberichte Wiener Akademie, 136(2a)*, 271–306.

Kuznetsova, E., Hoff, I., & Danielsen, S. W. (2017). FROST – Frost Protection of Roads and Railways. *Mineralproduksjon, 7*(B1-B8).

Nield, D. A., & Bejan, A. (2013). *Convection in porous media*: Springer.

Rieksts, K., Hoff, I., Kuznetsova, E. & Côté, J. (2017) Laboratory investigations of thermal properties of crushed rock materials. Pp. 143-149. In A. Loizos, I. Al-Qadi, and T. Scarpas, Eds. *Bearing capacity of roads, railways and airfield*,CRC Press 2017

Schuber, G., & Straus, J. M. (1979). Three-dimensional and multicellular steady and unsteady convection in fluid-saturated porous media at high Rayleigh numbers. *Journal of Fluid Mechanics, 94.01*, 25-38.

Tien, C. L. (1988). Thermal radiation in packed and fluidized beds. *Journal of Heat transfer, 110.4b*, 1230-1242.

Wang, M., & Bejan, A. (1987). Heat transfer correlation for Bénard convection in a fluid saturated porous layer

International Communications in Heat and Mass Transfer, 14.6, 617-626.

Xue, S. C., Poladin, L., Barton, G. W., & Large, M. C. J. (2007). Radiative heat transfer in preforms for microstructured optical fibres. *International Journal of Heat and Mass Transfer, 50.7*, 1569-1576.

Yen, Y.-C. (1974). Effects of density inversion on free convective heat transfer in porous layer heated from below. *International Journal of Heat and Mass Transfer, 17*(11), 1349-1356.

Appendix C – Paper III

This appendix includes the following paper submitted to the Canadian Geotechnical Journal.

Rieksts, K., Hoff, I., Scibilia, E. and Côté, J., 2018. *Laboratory investigations on convective heat transfer for road construction materials.*

PAPER III

Is not included due to copyright

Appendix D – Paper IV

This appendix includes the following paper submitted to the Journal name here.

Rieksts, K., Hoff, I., Scibilia, E. and Côté, J., 2018. *Modelling the Nu-Ra relationship to establish the intrinsic permeability of coarse open graded materials from natural air convection tests in 1m^3 cell.*

PAPER IV

Is not included due to copyright

Appendix E – Paper V

This appendix includes the following paper submitted to the International Communications in Heat and Mass Transfer.

Rieksts, K., Hoff, I., Scibilia, E. and Côté, J., 2018. *Comparison of different methods to assess the thermal conductivity of crushed rock solid particles used for road and railway construction.*

PAPER V

Is not included due to copyright

Appendix F – Paper VI

This appendix includes the following paper to be submitted to the Cold Regions Science and Technology.

Rieksts, K., Hoff, I., Scibilia, E. and Côté, J., 2018. *Validation and adaptation of thermal conductivity model for crushed rock materials.*

PAPER VI

Is not included due to copyright

Appendix G – Paper VII

This appendix includes the following paper submitted to the Cold Regions Science and Technology.

Rieksts, K., Hoff, I., Scibilia, E. and Côté, J., 2018. *The presence of natural air convection in road structural layers: comparison between field observations and numerical model.*

PAPER VII

Is not included due to copyright